Nonlinear optical microscopy for the invisible: vibrational imaging of small molecules in live cells and electronic imaging of fluorophores into the ultra deep

Lu Wei

Submitted in partial fulfillment of the requirements for the degree
of Doctor of Philosophy
in the Graduate School of Arts and Sciences

COLUMBIA UNIVERSITY

2015

ABSTRACT

Nonlinear optical microscopy for the invisible: vibrational imaging of small molecules in live cells and electronic imaging of fluorophores into the ultra deep

Lu Wei

Nonlinear optical microscopy (NOM) has become increasingly popular in biomedical research in recent years with the developments of laser sources, contrast mechanisms, novel probes and etc. One of the advantages of NOM over the linear counterpart is the ability to image deep into scattering tissues or even on the whole animals. This is due to the adoption of near-infrared excitation that is of less scattering than visible excitation, and the intrinsic optical sectioning capability minimizing the excitation background beyond focal volume. Such an advantage is particularly prominent in two-photon fluorescence microscopy compared to one-photon fluorescence microscopy. In addition, NOM may provide extra molecular information (e.g. second harmonic generation and third harmonic generation) or stronger signal (e.g. stimulated Raman scattering and coherent anti-Stokes Raman scattering compared to spontaneous Raman scattering), because of the nonlinear interaction between strong optical fields and molecules. However, the merits of NOM are not yet fully exploited to tackle important questions in biomedical research.

This thesis contributes to the developments of NOM in two aspects that correspond to two fundamental problems in biomedical imaging: first, how to noninvasively image small functional biomolecules in live biological systems (Chapters 1-4); second, how to extend the optical imaging depth inside scattering tissues (Chapters 5-6).

The ability to non-perturbatively image vital small biomolecules is crucial for understanding the complex functions of biological systems. However, it has proven to be highly challenging with the prevailing method of fluorescence microscopy. Because it requires the utilization of large-size fluorophore tagging (e.g., the Green Fluorescent Protein tagging) that would severely perturb the natural functions of small bio-molecules. Hence, we devise and construct a nonlinear Raman imaging platform, with the coupling of the emerging stimulated Raman scattering (SRS) microscopy and tiny vibrational tags, which provides superb sensitivity, specificity and biocompatibility for imaging small biomolecules (Chapters 1-4). Chapter 1 outlines the theoretical background for Raman scattering. Chapter 2 describes the instrumentation for SRS microscopy, followed with an overview of recent technical developments. Chapter 3 depicts the coupling of SRS microscopy with small alkyne tags (C≡C) to sensitively and specifically image a broad spectrum of small and functionally vital biomolecules (i.e. nucleic acids, amino acids, choline, fatty acids and small molecule drugs) in live cells, tissues and animals. Chapter 4 reports the combination of SRS microscopy with small carbon-deuterium (C-D) bonds to probe the complex and dynamic protein metabolism, including protein synthesis, degradation and trafficking, with subcellular resolution through metabolic labeling. It is to my belief that the coupling of SRS microscopy with alkyne or C-D tags will be readily applied in answering key biological questions in the near future.

The remaining chapters of this thesis (Chapters 5-6) present the super-nonlinear fluorescence microscopy (SNFM) techniques for extending the optical imaging depth into scattering tissues. Unlike SRS microscopy that is an emerging technique, multiphoton microscopy (mainly referred as two-photon fluorescence microscopy), has matured over 20 years with its setup scheme and biological applications. Although it offers the deepest penetration in the optical microscopy, it still poses a fundamental depth limit set by the signal-to-background ratio when imaging into scattering tissues. Three SNFM techniques are proposed to extend such a depth limit: unlike the conventional multiphoton microscopy whose nonlinearity stems from virtual-states mediated simultaneous interactions between the incident photons and the molecules, the high-order nonlinearity of the SNFM techniques that we have conceived is generated through real-state mediated

population-transfer kinetics. In particular, Chapter 5 demonstrates the multiphoton activation and imaging (MPAI) microscopy, which adopts a new class of fluorophores, the photoactivatable fluorophores, to significantly extend the fundamental imaging depth limit. Chapter 6 theoretically and analytically depicts two additional SNFM techniques of stimulated emission reduced fluorescence (SERF) microscopy and focal saturation microscopy. Both MPAI and focal saturation microscopies exhibit a fourth order power dependence, which is effectively a four-photon process. SERF presents a third order power dependence for a three-photon process.

TABLE OF CONTENTS

LIST OF FIGURES

LIST OF TABLES

ACKNOWLEDGEMENTS

My deepest and heartfelt thanks to my advisor Prof. Wei Min, for his full support, passionate discussion, positive encouragements, and all the long hours he spent to teach me thinking creatively and writing logically. I feel extremely lucky to have him as my mentor and enjoy working with him. Every thesis survives from spending a huge amount of efforts exploring immature ideas and from learning after countless unproductive trial experiments. This one is no exception. I thus feel eternally grateful to Wei for always available to offer his enlightening scientific opinions about the projects and optimistic thoughts to cheer me up whenever I needed them. I also thank him for giving me enough trust and freedom to learn and explore by myself.

I thank all the Min lab members for their contribution to this thesis: Dr. Ya-ting Kao and Dr. Evangelos Gatzogiannis for the initial guide when I first joined the Min lab. Dr. Zhixing Chen for the inspiring discussion and helpful suggestions from a perspective of an organic chemist. Dr. Luyuan Zhang for the helpful discussion. Yihui Shen and Fanghao Hu for sharing the hardship and joyfulness from our projects together. Lixue Shi for the help on my experiments.

This thesis could not have been possible without all the input from my collaborators. I thank Prof. Virginia Cornish for her encouragements and sound suggestions through the years. Prof. Louis Brus and Prof. Ann McDermott for the insightful advice about my projects. Prof. Rafael Yuste for all the discussions and supports on neuroscience related experiments. Prof. Meng Wang for all her kind help, support and the discussion about science and life when I was in her lab performing our very first SRS experiments. Prof. Martie Chalfin and Prof. Elizabeth Hillman for helpful discussion. Prof. Kimara Targoff and Jamie Harrington for all the zebrafish experiments. Christophe Dupre and Dr. Yeonsook Shin for the assistance on mouse related experiments. Dr. Yong Yu for driving me back to hotel for all those late experiment nights in Houston. Andrew Anzalone for patiently explaining organic synthesis routes to me.

I would like to thank the entire faculty at Columbia Chemistry Department, for creating such a scientifically friendly environment. Especially I would like to thank my progress committee members, Prof. Louis Brus, Prof. Ann McDermott and Prof. Ruben Gonzalez, for the helpful advice, encouragements and criticisms that have urged me to work harder and grow into a better researcher. I thank Prof. Louis Brus, Prof. Ann McDermott, Prof. Ronald Breslow and Prof. Peter Sims for serving on my defense committee.

I am grateful to all the people that have helped me. My friends and peers at Columbia University for the companionship. My undergraduate advisor Prof. Zijian Guo at Nanjing University for introducing me into the wonderland of research. My summer research advisor Prof. Yung-ya Lin at UCLA for helping me realize my interest in using physical principles and chemical methods to solve biological problems.

Finally, I would like to give my special thanks to my family: my parents and my grandparents for their unconditional love; my husband Fangzhou for the warmth and tolerance; for all the happy moments together; and for all the hours commuting between New Haven and New York.

Chapter 1

Theory of stimulated Raman scattering microscopy

Abstract

Chapters 1-5 focus on non-invasive imaging of small functional bio-molecules in live cells, tissues and animals by the coupling of the emerging stimulated Raman scattering (SRS) microscopy with small vibrational tags. In order to comprehend the SRS microscopy, including the experimental setup, the data acquisition, the signal estimation and interpretation, the advantages over spontaneous Raman scattering and coherent anti-Stokes Raman scattering (CARS) microscopy, and certain disadvantages, a thorough understanding of the underlying physical principles is essential. Therefore, Chapter 1 focuses on the theory of both the spontaneous and the stimulated Raman scattering. Classical theory of light-molecule interaction is first highlighted as it provides intuitive yet insightful understanding of the physical processes, and suffices as qualitative explanation of many experimental phenomena. A complete and quantitative understanding of these processes requires quantum mechanical theory, which is then discussed briefly.

1.1 Background.

The spontaneous Raman scattering effect, probing the molecular vibrations, was first reported in 1928 in *Nature*[1] and awarded the *Nobel Prize in Physics* in 1930. However, due to the excessively feeble signal, Raman spectroscopy was not popularized until the invention of laser in the 1960s. Despite the rapid developments as a spectroscopy technique, which is capable of acquiring a Raman spectrum revealing molecular information at one data point within seconds, the spontaneous Raman scattering is far from ideal as an imaging technique due to unsatisfying acquisition speed. Therefore, it is not widely applied in biomedical studies, for which fine temporal and spatial resolutions are highly demanded as the samples are usually live and in complex environments. In addition, the parasitic auto-fluorescence from biologic samples that easily overwhelms the weak spontaneous Raman signals also hinders its further developments[2].

Stimulated Raman scattering (SRS), accidentally observed in 1963[3], could however, overcome the aforementioned major disadvantages in spontaneous Raman scattering and be implemented for biomedical imaging. This coherent two-photon Raman process adopts the stimulated emission amplification principle, and thus dramatically increases the efficiency of the weak spontaneous Raman transition. It become increasingly popular with the maturation of ultrafast lasers. Femtosecond stimulated Raman scattering (fSRS) was later developed as an ultra-fast spectroscopic technique that has been widely utilized for probing the vibrational excited-state dynamics of molecules[4]. The use of fSRS as a contrast mechanism for microscopy has also been proposed, however, the scheme was not entirely suitable as a biocompatible imaging technique[5]. In addition, coherent anti-

Stokes Raman scattering (CARS), another coherent Raman scattering process, has been applied as a biomedical imaging technique for almost 20 years[6-8]. Nevertheless, CARS microscopy suffers from severe spectral distortion, unwanted non-resonant background, non-straightforward concentration dependence and coherent image artifacts[2].

The implementation of SRS microscopy for high-speed biomedical imaging with shot-noise limited sensitivity was not demonstrated until 2008. It immediately offered much improved performance, overcoming all the aforementioned shortcomings of CARS[9,10]. In addition, SRS microscopy is immune to auto-fluorescence background in biological samples due to a unique detection scheme that is different from both spontaneous Raman scattering and CARS. Hence, SRS microscopy with fast image acquisition and linear signal dependence would be an ideal imaging modality unveiling the molecular information in biological samples. In fact, SRS microscopy has proven its unique value in biomedical applications including label-free detection of biomolecules[11-13], video-rate SRS imaging on live animals[14], tumor imaging[15] and etc.

Note that, the words “one-photon” and “two-photon” in this thesis indicate the signal-to-light-intensity dependence, but not the light-molecule interaction. “One-photon” designates linear signal-to-intensity relationship and “two-photon” represents nonlinear quadratic dependence. For example, spontaneous Raman scattering is a “one-photon” linear process in terms of the signal-intensity dependence, while it could be described as a two-photon light-molecule interaction process as shown later in quantum mechanics.

1.2 Classical theory of Raman scattering.

1.2.1 Basics of the light-molecule interaction.

In the classical theory, light is treated as an electromagnetic wave and molecules are treated as harmonic oscillators. The interaction of light and molecules could be understood as the interaction between electromagnetic radiation with charged particles, in which the particles are driven by the oscillatory motion of the electric field[2, 16]. In the molecules, nuclei are too heavy to adiabatically follow the driving frequency of up to PHz (10^{15} Hz) from usually adopted visible and near-infrared laser light, while electrons are light enough to follow such a driving frequency[2]. Therefore, when the electric field interacts with a molecule, the electrons outside the nuclei are driven away from equilibrium positions in absence of the electric field and one electron produces one induced dipole moment, characterized as:

$$\mu(t) = -e \cdot r(t) \tag{1.1}$$

with e the charge of the electron and $r(t)$ the displacement from the equilibrium position, indicating how strong the electron is bound to the nuclei. The induced polarization P is a macroscopic quantity that sums up all the induced dipole moments from all the N electrons in the molecule:

$$P = N\mu(t) \tag{1.2}$$

and is related to the material susceptibility χ and the external electric field $E(t)$ through

$$P = \varepsilon_0 \chi E(t) \tag{1.3}$$

with ε_0 the vacuum electric permittivity. Here $E(t)$ is weak compared to the interaction between the electrons and the nuclei. However, when $E(t)$ becomes stronger and the electrons are further driven away from the equilibrium position, the binding potential

between the electrons and the nuclei transits from harmonic to anharmonic. Thus, the dependence of the induced polarization and the electric field is not strictly linear any more as shown in Eq. 1.3 and should be modified with higher order nonlinear terms[17, 18]:

$$P = \varepsilon_0[\chi^{(1)}E(t) + \chi^{(2)}E^2(t) + \chi^{(3)}E^3(t) + ...] \quad (1.4)$$

where $\chi^{(n)}$ is the nth order susceptibility. The higher order χ of the material contributes to the higher order optical processes. For example, the second harmonic generation is a $\chi^{(2)}$-process, and the coherent Raman scattering, including both CARS and SRS, is a $\chi^{(3)}$ process.

Raman scattering probes the vibrational motion between the nuclei of a molecule through driving the oscillation of the electrons by light. Since electrons are bound to nuclei and their motion depends on nuclear coordinates, the driven oscillation of the electrons contains information from nuclear vibration. Because chemical bonds exhibit a specific vibrational frequency for each vibrational mode in different chemically structured molecules, Raman spectra could thus reveal molecular information about materials. For simplicity, the molecule is regarded as a two-atom harmonic system with a single vibrational mode in the following discussion.

1.2.2 Classical description of spontaneous Raman scattering.

Polarizability $\alpha(t)$, describing the ability of a molecule to be polarized, is introduced to connect the nuclear motion and the external electric field with the induced electric dipole moment:

$$\mu(t) = \alpha(t)E(t) \quad (1.5)$$

assuming that the driving frequency is far from electronic resonance. $\alpha(t)$ could be expanded in a Taylor series in terms of the nuclear coordinates $Q(t)$, which directly quantify the nuclear motion for a molecule:

$$\alpha(t) = \alpha_0 + (\frac{\partial \alpha}{\partial Q})_0 Q(t) + ... \tag{1.6}$$

Here α_0 it the rigid molecule polarizability, and $(\partial\alpha/\partial Q)_0$ is interpreted as the coupling between electronic and nuclear motion.

Nuclear motion is treated as a harmonic oscillator, thus yielding:

$$Q(t) = Q_0(e^{i(\omega_v t+\phi)} + e^{-i(\omega_v t+\phi)}) \tag{1.7}$$

where Q_0 is the amplitude of the nuclear vibration; ω_v is the nuclear vibrational frequency; ϕ is the phase for the vibration. On the other hand, the incoming optical field could be expressed as:

$$E(t) = E_0(e^{i\omega_1 t} + c.c.) \tag{1.8}$$

with E_0 and ω_1 being the amplitude and the frequency of the external electric field respectively, and *c.c.* short for complex conjugate. Taking Eqs. 1.6-1.8 into Eq. 1.5, the interaction between light and molecule containing the information of electron-nuclear motion coupling could thus be expressed as:

$$\mu(t) = E_0\alpha_0 e^{-i\omega_1 t} + E_0(\frac{\partial \alpha}{\partial Q})_0[e^{-i(\omega_1-\omega_v)+\phi} + e^{-i(\omega_1+\omega_v)+\phi}] + c.c \tag{1.9}$$

where the induced dipole moments oscillate at three different frequencies ω_1, $\omega_1 - \omega_v$ and $\omega_1 + \omega_v$ (Fig.1.1a). Classically, oscillating dipoles act as antennas and radiate[18]. The radiated light from Eq. 1.9 is that of the scattered light. Thus, the first term with

frequency ω_1 designates the elastic Raleigh scattering, the second term with frequency $\omega_1 - \omega_v$ is the Stokes-shifted inelastic Raman scattering and the third term with frequency $\omega_1 + \omega_v$ is the anti-Stokes-shifted inelastic Raman scattering.

Note that both Raman scattering signals are proportional to the coupling term $(\partial\alpha/\partial Q)_0$, whose value being non-zero forms the selection rule for Raman active vibrational modes. In addition, Eq. 1.9 illustrates that while the photons scattered from Raleigh process are coherent with each other, photons scattered in the Raman process from an ensemble of molecules are incoherent since the phases of the scattered photons stem from the random phases ϕ of the uncorrelated molecules.

The classical model concisely presents the physical picture that enables intuitive understanding of the Raman scattering and offers qualitative interpretation and prediction for various experimental phenomena without complicated calculation. For example, the treatment of molecules as harmonic oscillators nicely predicts the experimentally measured Raman frequency, since the vibrational frequency ω_v scales with the square root of the reduced mass m:

$$\omega_v = \frac{1}{2\pi}\sqrt{\frac{k}{m}} \tag{1.10}$$

Experimentally, the carbon-hydrogen bond (C-H) vibration is measured to be around 2940 cm^{-1}. Since the reduced mass of the carbon-deuterium bond (C-D) is about 2 times of C-H, Eq. 1.10 predicts its vibration frequency to be peaked around 2100 cm^{-1}, $\sqrt{2}$

times of that of the C-H vibration. This is very close to the experimental measurements, which will be shown in Chapter 4.

However, the classical theory does pose a few shortcomings. First, it fails to quantitatively predict the correct intensity ratio. For example, it is indicated in Eq. 1.9 that the Stokes-shifted Raman signal is equally intense as the anti-Stokes shifted signal, which is not consistent with the experimental results. In addition, the classical model cannot predict the results under the electronic resonance condition. Brief discussion of quantum mechanical theory will be provided in section 1.3.

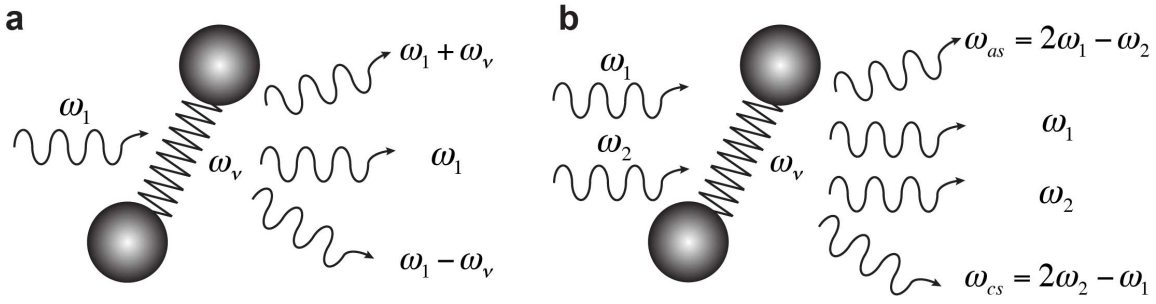

Fig. 1.1 Cartoon demonstration of spontaneous Raman scattering and coherent Raman scattering. (a) The incident light at frequency ω_1 is scattered by a molecule with vibrational frequency at ω_v into Raleigh scattering light at ω_1 and spontaneous Raman scattering light at Stokes frequency of $\omega_1 + \omega_v$ and at anti-Stokes frequency of $\omega_1 - \omega_v$. (b) When two lights at frequency ω_1 and ω_2 (where $\omega_1 - \omega_2 = \omega_v$) are incident on the molecule, the molecular nuclear vibration is efficiently driven by the lights at frequency ω_v. The subsequent incoming light is scattered into components of ω_1 (stimulated Raman loss), ω_2 (stimulated Raman gain), $2\omega_1 - \omega_2$ (coherent anti-Stokes scattering) and $2\omega_2 - \omega_1$ (coherent anti-Stokes scattering) respectively with much higher amplitude comparing to that of the spontaneous Raman scattering. Figure reproduced with modifications from Ref. 2.

1.2.3 Classical model of coherent Raman scattering: CARS and SRS

In contrast to spontaneous Raman scattering whose signal arises when molecules interact with a single-frequency electric field, coherent Raman scattering signal is effectively produced by two electric fields whose frequency difference matches that of the nuclear vibrational frequency. In short, two incoming electric fields induce the oscillation of the electrons outside the nuclei of molecules. This electron oscillation in turn forms an effective force coherently driving the vibration of the nuclei. As such, the intensity of coherent Raman scattering is boosted relative to the spontaneous case.

Specifically, the two incoming fields, with the same propagation direction and polarization, could be written as:

$$E_n(t) = E_{0n}(e^{i\omega_n t} + c.c.), \text{ where } n = 1, 2. \tag{1.11}$$

When these two fields are strong enough, their combination frequencies ($\omega_1 + \omega_2$ and $\omega_1 - \omega_2$) could also drive the oscillation of the electrons. In particular, the difference frequency ($\Omega = \omega_1 - \omega_2$, assuming $\omega_1 > \omega_2$) is small enough to resonate with the vibration of the nuclei. Effectively, a driving force $F(t)$ is exerted on the nuclear vibration through the driven oscillation of surrounding electron clouds, given by[17]:

$$F(t) = (\frac{\partial \alpha}{\partial Q})_0 [E_{0,1} E^*_{0,2} e^{-i\Omega t} + c.c] \tag{1.12}$$

Again, $(\partial\alpha/\partial Q)_0$ is the non-zero coupling term between the electrons and the nuclei. The interaction between light and molecules is now treated as a damped harmonic oscillator model with an external driving force:

$$\frac{d^2Q(t)}{dt^2} + 2\gamma\frac{dQ(t)}{dt} + \omega_v Q(t) = \frac{F(t)}{m} \tag{1.13}$$

where γ is the damping constant, corresponding to the homogeneous linewidth of the vibrational transition; m is the reduced mass of the nuclei. Solving Eq. (1.13) leads to[2]:

$$Q(t) = Q(\Omega)e^{-i\Omega t} + c.c \text{, with amplitude } Q(\Omega) = \frac{1}{m}(\frac{\partial\alpha}{\partial Q})_0 \frac{E_{0,1}E_{0,2}^*}{\omega_v^2 - \Omega^2 - 2i\Omega\gamma} \tag{1.14}$$

Eq. 1.14 designates that chemical bonds with nuclear vibrational frequency close to Ω are coherently driven by the incoming electric fields. Therefore, when the third beam is incident on the sample, it experiences the periodic polarization change from the material that is created by the joint action of the first two beams, and thus being modulated.

From Eqs. 1.2 and 1.5, polarization is written as:

$$P(t) = N[\alpha_0 + (\frac{\partial\alpha}{\partial Q})_0 Q(t)][E_1(t) + E_2(t)] \tag{1.15}$$

In the case of coherent Raman scattering, the third light is from either $E_1(t)$ or $E_2(t)$. Considering only the nonlinear part of the polarization $P_{NL}(t)$ that contains the $(\partial\alpha/\partial Q)_0$ term leads to:

$$P_{NL}(t) = P(\omega_{as})e^{-i\omega_{as}t} + P(\omega_1)e^{-i\omega_1 t} + P(\omega_2)e^{-i\omega_2 t} + P(\omega_{cs})e^{-i\omega_{cs}t} + c.c \tag{1.16}$$

where,

$$P(\omega_{as}) = 6\varepsilon_0\chi_{NL}(\Omega)E_{0,1}^2E_{0,2}^* \tag{1.17}$$

$$P(\omega_1) = 6\varepsilon_0\chi_{NL}(\Omega)\left|E_{0,2}\right|^2 E_{0,1}^* \tag{1.18}$$

$$P(\omega_2) = 6\varepsilon_0\chi_{NL}^*(\Omega)\left|E_{0,1}\right|^2 E_{0,2} \tag{1.19}$$

$$P(\omega_{cs}) = 6\varepsilon_0\chi_{NL}(\Omega)E_{0,2}^2E_{0,1}^* \tag{1.20}$$

and

$$\chi_{NL}(\Omega) = \frac{N}{6m\varepsilon_0}(\frac{\partial\alpha}{\partial Q})_0^2 \frac{1}{\omega_v^2 - \Omega^2 - 2i\Omega\gamma} \tag{1.21}$$

Here $\omega_{as} \equiv 2\omega_1 - \omega_2$ and $\omega_{cs} \equiv 2\omega_2 - \omega_1$ are defined as the CARS frequency and the coherent Stokes Raman scattering (CSRS) frequency respectively.

Eqs 1.16-1.21 present the origin for the coherent Raman scattering, informing us that four parallel $\chi^{(3)}$ processes with similar amplitude are occurring simultaneously (Fig.1.1b). Two of them are at the fundamental frequencies (ω_1 and ω_2) that would interfere with the local electric fields, with $P(\omega_1)$ responsible for stimulated Raman loss (SRL) and $P(\omega_2)$ for the stimulated Raman gain (SRG). The other two are at new frequencies, with $P(\omega_{as})$ and $P(\omega_{cs})$ corresponding to CARS and CSRS, respectively. It is worth pointing out that, in terms of the nonlinear polarizations, these four simultaneous processes exhibit similar amplitudes assuming that the two laser intensities are close to each other. However, in terms of the final experimentally detected signals, their amplitudes vary due to the different signal frequencies and the consequent distinct detection schemes. In addition, these differences could also explain why SRS microscopy is free from the complications (e.g. non-resonant background) in the CARS microscopy. Detailed comparison between SRS and CARS microscopy will be covered in section 1.2.4. Now we discuss the four signals in turn.

Solving Maxwell's wave equations yields the nonlinear field $E_{as}(t)$ at the anti-Stokes frequency that is emitted from the nonlinear polarization $P(\omega_{as})e^{-i\omega_{as}t}$. Hence the intensity of the detected CARS signal is directly proportional to the modulus of $P(\omega_{as})$:

$$I_{CARS} = I(\omega_{as}) = \frac{\varepsilon_0 c}{2}\left|E_{as}^{(3)}\right|^2 \propto \left|\chi_{NL}\right|^2 I_1^2 I_2 \tag{1.22}$$

where $E_{as}^{(3)}$ is the amplitude for the induced nonlinear electric field at anti-Stokes frequency; $I_1 = \frac{\varepsilon_0 c}{2}\left|E_{0,1}\right|^2$ and $I_2 = \frac{\varepsilon_0 c}{2}\left|E_{0,2}\right|^2$ are externally applied laser intensity at ω_1 and ω_2.

Since I_{CARS} is at a new frequency that is different from the laser frequencies and is much smaller than the incident laser intensity, it is experimentally detected by a photo-multiplier tube (PMT) after separating it from laser lights with an optical filter. In addition, since $\chi_{NL}(\Omega) \propto N$, as shown in Eq. 1.21, I_{CARS} is thus to the square of the analyte concentration $c(analyte)$, which usually complicates the experimental signal interpretation. Moreover, this signal-concentration dependence is further complicated by the presence of the non-resonant background in CARS, discussed in the next section.

Similarly to CARS, the CSRS signal could be written as:

$$I(\omega_{cs}) \propto \left|\chi_{NL}\right|^2 I_2^2 I_1 \tag{1.23}$$

However, CSRS is not as popular as CARS, although they have similar intensities. This is because the CSRS signal is at a lower frequency ($\omega_{cs} \equiv 2\omega_2 - \omega_1$) than laser frequencies, thus longer wavelength. Hence CSRS signal is not ideal for experimental

detection due to the low quantum yield from the currently available detectors in the near-infrared region by the near-infrared laser excitation. Even by visible excitation, this signal is still difficult to achieve since it would be easily complicated by samples' auto-fluorescence.

Cases are different for the stimulated Raman scattering (including both SRL and SRG). Since SRS is a coherent process and the signals are at the same frequencies as the incident lasers, the detected SRS signals are results of the interference between induced nonlinear fields $E_1^{(3)}(t)$ and $E_2^{(3)}(t)$ and the local fields $E_1(t)$ and $E_2(t)$ respectively. $E_1^{(3)}(t)$ and $E_2^{(3)}(t)$ are emitted from the nonlinear polarization of $P(\omega_1)e^{-i\omega_1 t}$ and $P(\omega_2)e^{-i\omega_2 t}$. Thus the scattered signals at ω_1 and ω_2 are contained in[2]:

$$I(\omega_1) = \frac{\varepsilon_0 c}{2}\left|E_1^{(3)} + E_{0,1}\right|^2 \propto \left|E_1^{(3)}\right|^2 + \left|E_{0,1}\right|^2 - 2I_1 I_2 \operatorname{Im}\{\chi_{NL}\} \tag{1.24}$$

$$I(\omega_2) = \frac{\varepsilon_0 c}{2}\left|E_2^{(3)} + E_{0,2}\right|^2 \propto \left|E_2^{(3)}\right|^2 + \left|E_{0,2}\right|^2 + 2I_1 I_2 \operatorname{Im}\{\chi_{NL}\} \tag{1.25}$$

It can be seen from Eqs. 1.24 and 1.25 that compared to CARS and CSRS signals, SRS signals are not background-free, but produced on top of the laser intensities. Therefore, unlike CARS and CSRS signals that are directly proportional to the modulus of $P(\omega_{as})$, the SRL signal (I_{SRL}) is $I_1 - I(\omega_1)$ that is proportional to $2I_1 I_2 \operatorname{Im}\{\chi_{NL}\} - \left|E_1^{(3)}\right|^2$ and SRG signal (I_{SRG}) is $I(\omega_2) - I_2$ that is proportional to $2I_1 I_2 \operatorname{Im}\{\chi_{NL}\} + \left|E_2^{(3)}\right|^2$. Because $\left|E_1^{(3)}\right|$ and $\left|E_2^{(3)}\right|$ are much smaller than $\left|E_1\right|$ and $\left|E_2\right|$, the absolute values for both I_{SRL} and I_{SRG} are approximately proportional to $I_1 I_2 \operatorname{Im}\{\chi_{NL}\}$.

Because SRS signals are mixed with high intensity fundamental laser beams, it cannot be directly detected by PMT as in the case of CARS, but instead can be detected by a large-area photodiode that is capable of sustaining high photon intensity. In addition, obtaining pure SRS signal relies on the reference from the corresponding laser intensity. For example, the I_{SRL} is detected as $I_1 - I(\omega_1)$, where $I(\omega_1)$ is the intensity at frequency ω_1 in the presence of $E_2(t)$, and I_1 is detected in the absence of $E_2(t)$. In other words, I_{SRL} is recorded at ω_1 by turning the laser beam at ω_2 on and off. Similarly, I_{SRG} is detected at ω_2 by turning the laser beam at ω_1 on and off. More details on signal detection scheme is provided in Chapter 2. Note that, the difference in signal frequency (and thus the detection scheme) sets the key difference between SRS and CARS.

1.2.4 Signal intensity of CARS and SRS and the non-resonant background.

Signal intensity. It is worth comparing the signal intensities associated with these two popular imaging modalities. The classical model offers a good theoretical prediction for both CARS and SRS signals. From previous analysis, $I_{CARS} \propto \left|\chi_{NL}\right|^2 I_1^2 I_2$ and $I_{SRS} \propto I_1 I_2 \,\mathrm{Im}\{\chi_{NL}\}$. Because $\left|\chi_{NL}\right|$ is the third-order susceptibility and is a very small number, $I_{CARS} << I_{SRS}$ in terms of the absolute value. However, in practice, it is the signal-to-noise ratio (S/N) that determines the detection limit instead of the signal alone.

Because I_{SRS} detection involves laser intensity, its noises include both laser fluctuation noise and the shot noise of laser intensity. With high-frequency modulation scheme adopted (details in chapter 2), the laser fluctuation noise that is mainly at low

frequency could be readily removed. The remaining shot noise arises from the intrinsic Poisson distribution of photon detection. The size of the shot noise is given by the square-root of the detected photon number. Thus $(S/N)_{SRS}$ is given by:

$$(S/N)_{SRL} = \frac{I_{SRL}}{\alpha I_1 + \sqrt{I_1}} \propto \sqrt{I_1} I_2 \,\mathrm{Im}\{\chi_{NL}\} \tag{1.26}$$

$$(S/N)_{SRG} = \frac{I_{SRG}}{\alpha I_2 + \sqrt{I_2}} \propto I_1 \sqrt{I_2} \,\mathrm{Im}\{\chi_{NL}\} \tag{1.27}$$

where αI_1 and αI_2 represent the low-frequency laser fluctuation noise and $\alpha \to 0$ in the high-frequency modulation scheme[10].

On the other hand, the I_{CARS} detection is laser background free. Thus, the overall noise arises from the shot-noise of CARS photons in addition to the CARS signal fluctuation noise transferred from the laser fluctuation noise. With high-frequency modulation, $(S/N)_{CARS}$ is given by:

$$(S/N)_{CARS} \propto \frac{I_{CARS}}{\sqrt{I_{CARS}} + \alpha I_{CARS}} = |\chi_{NL}| I_1 \sqrt{I_2} \tag{1.28}$$

where αI_{CARS} is transferred from the low-frequency laser fluctuation noise and $\alpha \to 0$ in the high-frequency modulation scheme.

Hence, in the shot-noise limited condition, $(S/N)_{CARS} \approx (S/N)_{SRS}$ assuming $I_1 = I_2$. Experimentally, the detection sensitivity of SRS has been proven to approach the shot-noise limit. Nevertheless, the detection of CARS is not, since it usually does not adopt the

high-frequency modulation because αI_{CARS} that is transferred from laser fluctuation noise is much smaller than αI_1 or αI_2 of actual laser fluctuation noise.

Non-resonant background. It is widely known that CARS microscopy severely suffers from spectral distortion from the non-resonant background. On the contrary, SRS microscopy presents identical spectrum as the spontaneous Raman scattering. This section discusses the physical origin. When the frequency difference between the pump and the Stokes beams approaches the vibrational frequency, that is when $\Omega \to \omega_v$ and Ω varies slowly. Eq. 1.21 can be:

$$\chi_{NL}(\Omega) \approx \frac{N}{6m\varepsilon_0}\left(\frac{\partial \alpha}{\partial Q}\right)_0^2 \frac{1}{2\Omega} \frac{1}{\omega_v - \Omega - i\gamma} \tag{1.29}$$

Figure 1.2 plots $\mathrm{Re}\{\chi_{NL}(\Omega)\}$ and $\mathrm{Im}\{\chi_{NL}(\Omega)\}$ as a function of $\Omega - \omega_v$, normalized to the maximum value of $\mathrm{Im}\{\chi_{NL}(\Omega)\}$. When $\Omega = \omega_v$, it is called the Raman on-resonance condition; while when Ω is away from ω_v ($\Omega << \omega_v$ or $\Omega >> \omega_v$), it is called the Raman off-resonance condition.

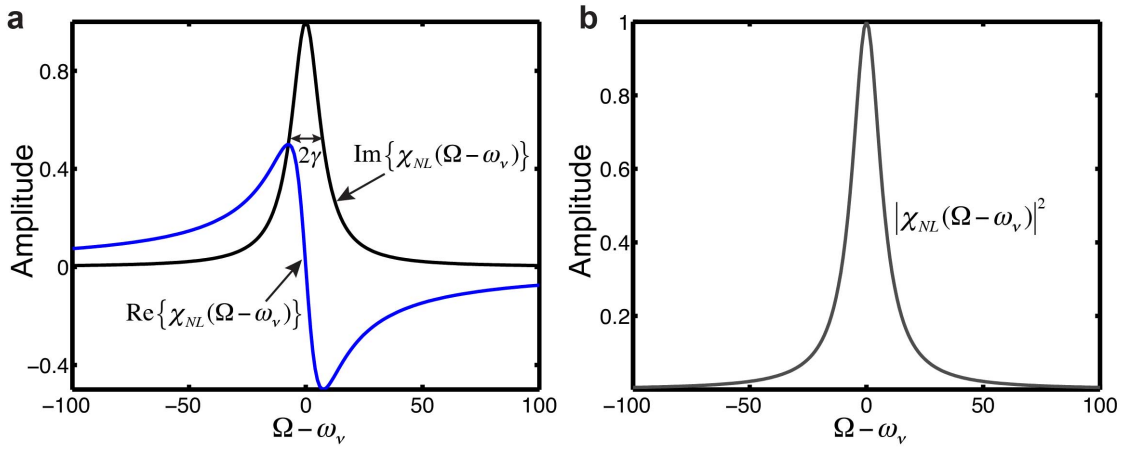

Fig. 1.2 Spectral dependence of nonlinear susceptibility χ_{NL} near vibrational resonance. (a) Simulated spectra of both the imaginary part of χ_{NL} and the real part of χ_{NL} as a dependence on $\Omega-\omega_v$, normalized to the maximum value of $\mathrm{Im}\{\chi_{NL}(\Omega-\omega_v)\}$. The spectrum of $\mathrm{Im}\{\chi_{NL}(\Omega-\omega_v)\}$ corresponds to the SRS spectrum of with a peak width of γ. (b) The simulated plot of $|\chi_{NL}(\Omega-\omega_v)|^2$ corresponding to the CARS spectrum without the interference of non-resonance background. Its peak width is slightly larger than γ.

The non-resonant background originates from the driven oscillation of electrons in solvents by the two external electric fields. Its signal is proportional to the third order susceptibility χ_{NR}, which is a real constant number without dependence on the vibrational frequency of Ω. With the influence of χ_{NR}, Eq. 1.22 representing the CARS signal becomes:

$$I_{CARS} \propto |\chi_{NL}+\chi_{NR}|^2 I_1^2 I_2 = (|\chi_{NL}|^2+|\chi_{NR}|^2+2\,\mathrm{Re}\{\chi_{NL}\}\chi_{NR})I_1^2 I_2 \qquad (1.30)$$

The resulting CARS spectrum with the interference from non-resonant background is thus severely distorted (Fig. 1.3a) compared to both the SRS spectrum and the CARS spectrum free from non-resonant background (Fig. 1.2). This is consistent with experimental observations.

On the contrary, since $I_{SRS} \propto I_1 I_2 \,\mathrm{Im}\{\chi_{NL}\}$ and the non-resonant background only interferes with the $\mathrm{Re}\{\chi_{NL}\}$, the SRS spectrum is thus not influenced. Therefore, the SRS spectrum, possessing the shape of $\mathrm{Im}\{\chi_{NL}\}$ (Fig. 1.2a), is identical to the spontaneous Raman spectrum, which has been confirmed experimentally[9]. To better illustrate the non-resonant background, Fig. 1.3b-c present two sets of images that compares the CARS and SRS results for the same tissue sample. The images at the left panel is for the C-H on-resonance where $\Omega = \omega_v(C-H) = 2845\, cm^{-1}$, and the images at the right panel is at the C-H off-resonance where Ω is away from $\omega_v(C-H)$. The on-resonance images of SRS and CARS exhibit similar intensities (Fig. 1.3b-c, left). However, while the off-resonance SRS image is background-free (Fig. 1.3c, right), the off-resonance CARS image (Fig. 1.3b, right) is not due to the interference of non-resonant background, which prevents the straightforward interpretation for CARS images.

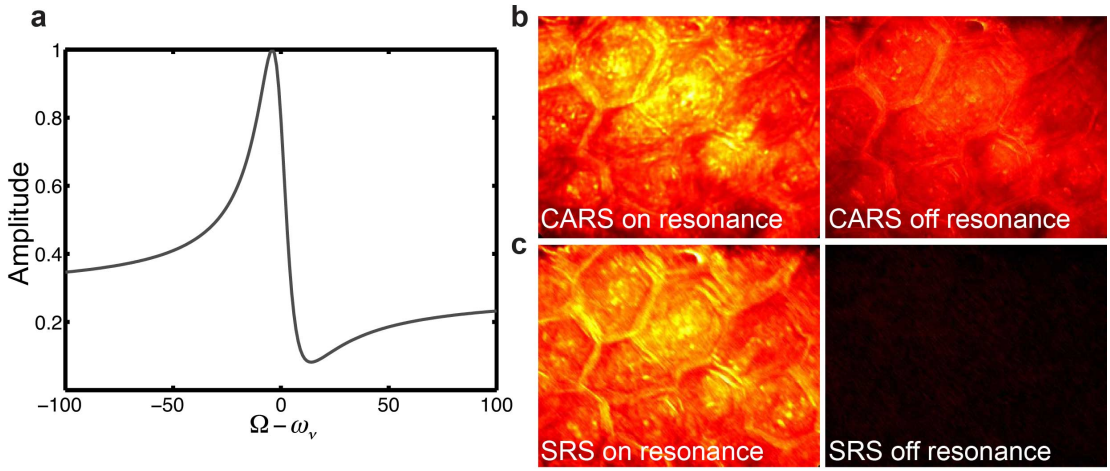

Fig. 1.3 Non-resonant background for CARS microscopy[9, 10]**.** (a) Simulated CARS spectrum with the interference from a constant non-resonant background. (b) On-resonance and off-resonance image comparison of the same tissue sample at similar condition between CARS microscopy and SRS microscopy. The on-resonance images show similar image contrast (left panel, around $\Omega-\omega_v=0$). However, while the off-resonance SRS image is background-clear (lower, right, around $\Omega-\omega_v=-50$), the off-resonance CARS image presents the contribution from the non-resonant background (upper, right, around $\Omega-\omega_v=-50$).

Moreover, as mentioned in the previous section, such a non-resonant background further complicates the relation between I_{CARS} and $c(analyte)$. It has been shown that $I_{CARS}\propto c^2(analyte)$ in the absence of the non-resonant background. Here we discuss two extreme cases in the presence of the non-resonant background[10]. In the limit of concentrated analytes being pure liquid, $|\chi_{NL}|>>|\chi_{NR}|$. Then I_{CARS} is reduced to Eq. 1.22, where $I_{CARS}\propto c^2(analyte)$. In the limit of highly diluted analytes, $|\chi_{NL}|<<|\chi_{NR}|$. Because $|\chi_{NR}|$ is a constant real number, with the constant $|\chi_{NR}|^2$ ignored, I_{CARS} is approximated to $2\,\mathrm{Re}\{\chi_{NL}\}\chi_{NR}I_1^2I_2$, where $I_{CARS}\propto c(analyte)$. This complication is not present in the SRS microscopy, because I_{SRS} is free from the non-resonant background interference and

is proportional to the imaginary part of χ_{NL} that is directly linear proportional to $c(analyte)$.

1.3 Quantum mechanical theory.

Although the classical treatment for the Raman scattering is qualitative and easily understood for various experimentally observed phenomena, it does not recognize the quantized nature of light-matter interactions. Quantum mechanical theory incorporates the quantum mechanical character of the light-matter interaction. However, it is difficult to explain such a quantized interaction without complex analytical approximations and quantum calculations. Brief discussion aiding the quantitative signal interpretation between the stimulated Raman scattering and spontaneous Raman scattering is provided in this section.

In the quantum mechanical treatment, the material states are described as molecular wavefunctions in space and time as a superposition of molecular eigenstates $\psi_n(r,t)$ [16]:

$$\psi(r,t) = \sum_n c_n \psi_n(r,t) \tag{1.31}$$

where the coordinate r includes both the electronic and nuclear coordinates. The evolution of the wavefunction in time is given by the time-dependent Schrodinger equation:

$$i\hbar \frac{\partial \psi(r,t)}{\partial t} = \hat{H}_0 \psi_n(r,t) \tag{1.32}$$

that $\hat{H}_0$ is the Hamiltonian for the system without external fields, and the hat indicates $\hat{H}_0$ as an operator. The eigenstates $\psi_n(r,t)$ of the unperturbed Hamiltonian can be expressed as:

$$\psi_n(r,t) = a_n(r)e^{-i\omega_n' t} \tag{1.33}$$

where $a_n(r)$ designates the spatial part of the wavefunction; and ω_n' is the eigen-frequency associated with ψ_n.

The wavefunction is affected when applied with an external field and the Hamiltonian is revised to:

$$\hat{H} = \hat{H}_0 + \hat{V}(t) \tag{1.34}$$

where the interaction potential operator is

$$\hat{V}(t) = -\hat{\mu}\cdot E(t) \tag{1.35}$$

The hat is dropped for simplicity from now on. In the long-wavelength limit, $E(t)$ is approximated to Eq. 1.8. The interaction potential between two fields $E_1(t)$ and $E_2(t)$ with a molecule is written as:

$$V(t) = -E_2(t)\cdot\alpha\cdot E_1(t) = -\alpha E_{02}E_{01}[e^{i(\omega_1+\omega_2)t} + e^{i(\omega_1-\omega_2)t} + e^{i(\omega_2-\omega_1)t} + e^{-i(\omega_1+\omega_2)t}] \tag{1.36}$$

where $\omega_1 > \omega_2$ and E_{01} and E_{01} are the amplitude for the $E_1(t)$ and $E_2(t)$ respectively.

Eq. 1.36 informs us that four possible transitions are induced by the time-dependent interaction: (1) $e^{-i(\omega_1+\omega_2)t}$ causes the absorption of one photon at frequencies ω_1 and ω_2 respectively (Fig. 1.4a). This process is a coherent process in which the absorption rate is

utterly different from that of the sequential absorption of two photons by a molecule. (2) $e^{i(\omega_1+\omega_2)t}$ causes the emission of two photons from each of the frequency (Fig. 1.4b). (3) $e^{i(\omega_2-\omega_1)t}$ causes the absorption of the ω_1 photon and the emission of the ω_2 photon, corresponding to the Stokes-shifted Raman transition (Fig. 1.4c). (4) $e^{i(\omega_1-\omega_2)t}$ causes the absorption of ω_2 photon and the emission of the ω_1 photon, corresponding to the anti-Stokes-shifted Raman transition (Fig. 1.4d). Note that both orders shown in Fig. 1.4 could happen, but may have distinct probabilities[16].

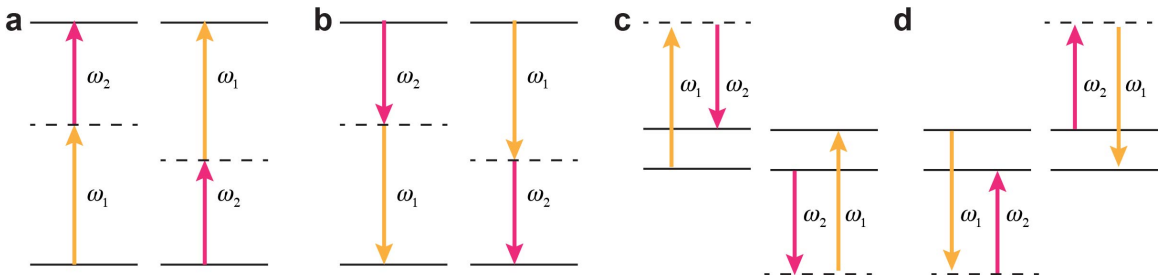

Fig. 1.4 Four possible transitions induced by the time-dependent interaction between two fields and a molecule. (a) Two-photon absorption. (b) Two-photon emission. (c) Stokes-shifted Raman scattering. (d) Anti-Stokes-shifted Raman scattering. Reproduced from Ref. 16.

From Fermi's golden rule, the transition rate could thus be expressed as:

$$w = \frac{2\pi}{\hbar}\frac{1}{16}\rho(\alpha E_{02}E_{01})^2 = \alpha\rho\frac{2\pi}{\hbar}(\frac{2\pi\hbar}{V})^2\omega_1\omega_2 N_1(N_2+1) \tag{1.37}$$

where $E = (\frac{8\pi\hbar\omega N}{V})$ could be shown[16], V is volume, ρ is emitted field density of states, and Eq. 1.37 has been corrected for spontaneous emission by replacing N_2 to N_2+1.

The Raman intensity in the form of differential cross section is defined as:

$$d\sigma = \frac{\text{rate of scattering into solid angle } d\Phi}{N_{\text{incident photon flux in beam absorbed}}} \tag{1.38}$$

where $N_{\text{incident photon flux in beam absorbed}} = \frac{N_1 c}{V}$, and c is the speed of light. Taking Eq. 1.37, where $\rho = \frac{V}{(2\pi c)^3}\frac{\omega^2}{\hbar}d\Phi$ into Eq. 1.38, leads to:

$$d\sigma = \frac{\alpha\omega_1\omega_2^3(N_2+1)}{c^4}d\Phi \tag{1.39}$$

Eq. 1.39 illustrates that the Raman scattering intensity is linearly proportional to ω_1 and is in cubic dependence on ω_2, explaining why the longer the excitation wavelength, the less the scattering there is.

More importantly, Eq. 1.39, where $d\sigma$ is proportional to (N_2+1), is the key for explaining why the SRS signal is much stronger than the spontaneous Raman signal, where the spontaneous emission is created by vacuum fluctuation ($N_2 = 0$). N_2 is the photon number in an optical mode in the Stokes laser.

The ratio between stimulated Raman cross section and spontaneous Raman cross section could then be expressed as:

$$\frac{d\sigma_{SRS}}{d\sigma_{\text{Spontaneous}}} = N_2 + 1 \tag{1.39}$$

meaning that the signal enhancement is proportional to the Stokes laser intensity.

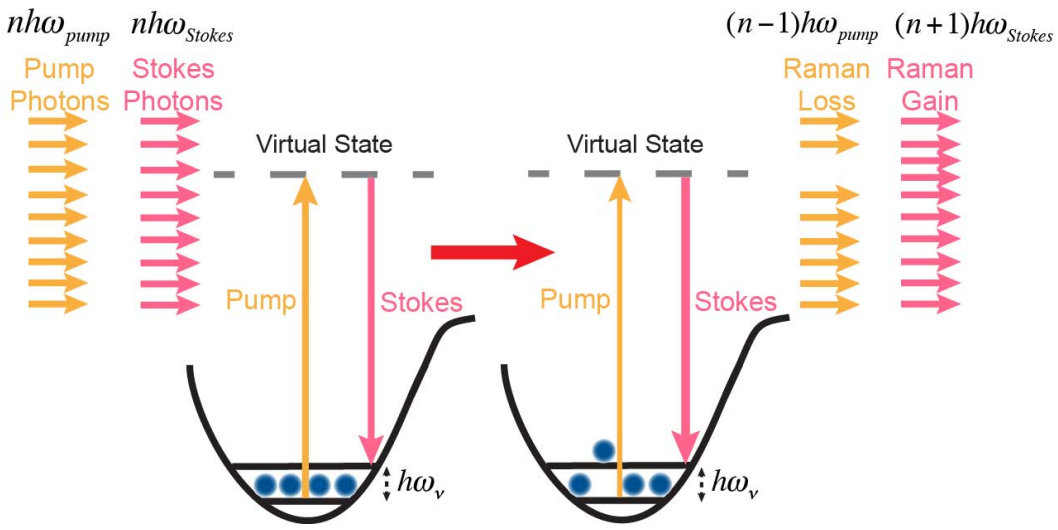

Fig. 1.5 Quantum interaction scheme of stimulated Raman scattering. A quantum of the scatterers being excited is accompanied by the annihilation of one pump photon and the creation of one Stokes photon.

Experimentally, N_2 is estimated to reach ~10^8 using a biocompatible Stokes laser (~ 50 mW average power, 76 MHz pulse train, 6 ps pulse width and a high-NA objective)[9, 10], representing a ~10^8 faster Raman transition rate in SRS compared to spontaneous Raman scattering. Quantum mechanically, SRS is explained as: when both the pump and Stokes laser beams are incident on the sample, the Raman transition is gigantically elevated by the quantum amplification. Each quantum of the vibrational excitation being excited is accompanied by one photon being annihilated in the pump beam and simultaneously one photon being created in the Stokes beam[10] (Fig. 1.5).

1.4 References.

1. Raman, C. V. & Krishnan, K. S. A new type of secondary Radiation. *Nature*, **121**, 501-502 (1928)
2. Cheng, J. -X. & Xie, X. S. *Coherent Raman Scattering Microscopy* (CRC Press, 2012).
3. Woodbury, E.J., Ng, W.K. Ruby laser operation in the near IR, *Proc. IRE* **50**, 2347–2348 (1962).
4. Kukura, P., McCamant, D. W., & Mathies, R. A. Femtosecond Stimulated Raman Spectroscopy. *Annu. Rev. Phys. Chem.* **58**, 461-488 (2007).
5. Ploetz, E., Laimgruber, S., Berner, S., Zinth, W. & P. Gilch, Femtosecond stimulated Raman microscopy, *Appl. Phys. B*, 87, 389-393 (2007)
6. Duncan, M. D., Reintjes, J. & Manuccia, T. J. Scanning coherent anti-Stokes Raman microscope, *Opt. Lett.* **7**, 350-352 (1982).
7. Zumbusch, A., Holtom, G. R., & Xie, X. S. Three-Dimensional Vibrational Imaging by Coherent Anti-Stokes Raman Scattering, *Phys. Rev. Lett.* **82**, 4142-4105 (1999).
8. Volkmer, A., Cheng, J. –X., & Xie, X. S. Vibrational Imaging with High Sensitivity via Epi detected Coherent Anti-Stokes Raman Scattering Microscopy, *Phys. Rev. Lett.* **87**, 023901 (2001).
9. Freudiger, C. W. et al. Label-free biomedical imaging with high sensitivity by stimulated Raman scattering microscopy. *Science* **322**, 1857-1861 (2008).
10. Min, W., Freudiger, C. W., Lu, S. & Xie, X. S. Coherent nonlinear optical imaging: beyond fluorescence microscopy. *Annu. Rev. Phys. Chem.* **62**, 507-530 (2011).
11. Zhang, X. et al. *ChemPhysChem* **13**, 1054-1059 (2012).
12. Freudiger, C. W. et al. Multicolored stain-free histopathology with coherent Raman imaging. *Lab. Invest.* 92, 1492-1502 (2012)
13. Wang, P., Liu, B., Zhang, D., Belew, M. Y., Tissenbaum, H. A., & Cheng, J.-X., Imaging Lipid Metabolism in Live Caenorhabditis elegans Using Fingerprint Vibrations. *Angew. Chem., Int. Ed.* **53**, 11787 –11792 (2014).
14. Saar, B. G. et al. Video-rate molecular imaging in vivo with stimulated Raman scattering. *Science* **330**, 1368-1370 (2010).

15. Ji, M. et al. Rapid, label-free detection of brain tumors with stimulated Raman scattering microscopy. *Sci. Transl. Med.* **5**, 201ra119-201ra119 (2013).
16. Schatz, G. C. & Ratner, M. A. *Quantum Mechanics in Chemistry* (Dover Publications, 2002).
17. Demtröder, W. *Laser Spectroscopy: Basic Concepts and Instrumentation* (Springer, 2nd edition, 1996).
18. Siebert, F. and Hildebrandt, P. *Vibrational Spectroscopy in Life Science.* (WILEY-VCH, 2008).

Chapter 2

Instrumentation of stimulated Raman scattering microscopy

Abstract

A detailed experimental setup and detection scheme for SRS microscopy is presented in this chapter. In addition, the background sources contributing to non-Raman signals in the SRS process are discussed. Moreover, strategies for minimizing those backgrounds are discussed, followed by an overview of advanced acquisition schemes for SRS microscopy.

2.1 Experimental setup for the SRS microscopy.

In theory, detection of either SRL or SRG yields the same results for the SRS signal. For all my experiments[1-3], SRL detection scheme is chosen. There are two reasons for this choice: first, the quantum yield of the currently available detectors favors the choice of SRL detection. In the high modulation scheme for SRL (which is discussed in details in later sections), the Stokes laser is intensity modulated and corresponding intensity change from the pump laser at the same frequency is detected. This scheme is interchanged in SRG. Current detectors are usually Si photodiodes whose maximum quantum yield is around 950 nm and sharply decreases toward higher wavelength. Thus the quantum yield is much higher for the detection at the usually used pump laser wavelength (from 800 – 950 nm) compared to that at the Stokes wavelength of 1064 nm. Second, choosing SRL helps maintain the optimal S/N in the effort of lowering photo-toxicity. It is shown that the Stokes laser wavelength further in the near-infrared region is less phototoxic than the pump laser wavelength region. Therefore, increasing the Stokes laser power while lowering the pump laser power on samples is one strategy to reduce the phototoxicity. However, as shown in Eqs. 1.26-1.27, the enhancement of the Stokes laser intensity elevates the noise level for $(S/N)_{SRG}$. Such a noise level elevation is not present in $(S/N)_{SRL}$, whose noise depends solely on the pump laser intensity. Hence, SRL detection is more beneficial than SRG.

Instrumentation for SRS microscopy of SRL detection is presented in Fig. 2.1 (a). Briefly, a modulated Stokes beam is collinearly combined with a pump beam and then sent into an objective that focuses both beams onto a sample. The output beams

subsequently pass through a filter, which transmits the pump laser but reflects the Stokes laser. The transmitted pump laser is then detected by a photodiode. Only the intensity change of the pump laser at the modulation frequency of the Stokes laser is picked up by a lock-in amplifier, which sends the signal into computer as the SRS intensity at one pixel. The SRS image is subsequently constructed by raster scanning the laser across the sample.

Next, specific components (including the choice of laser source, modulation, signal analysis and etc.) ensuring high sensitivity and fast detection are discussed.

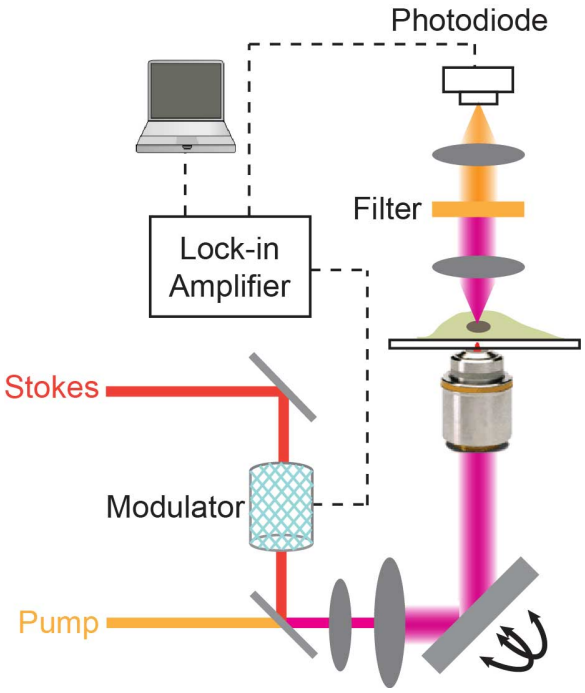

Fig. 2.1 Experimental setup for the stimulated Raman scattering microscopy. A modulated Stokes laser is collinearly combined with the pump laser and both are incident on a sample. The lights passing through the sample are optically filtered to block the Stokes wavelength. Thus only the transmitted pump laser is collected by the photodiode. The signal output from the photodiode is subsequently demodulated by a lock-in amplifier at the modulation frequency of the Stokes laser for the detection of SRS signal.

2.1.1 Laser source.

Because SRS is a nonlinear process, whose signal arises most efficiently with simultaneous excitation of both pump and Stokes photons at the transient time scale of the virtual state (around femto-second (*fs*) ~ pico-second (*ps*)), SRS microscopy requires the utilization of pulsed lasers with high peak-power. Continuous-wave (CW) lasers that are normally used in spontaneous Raman scattering could not ensure an efficient stimulated Raman process.

Both *fs*- and *ps*- lasers have been adopted for SRS microscopy previously, each with certain advantages and disadvantages. *Fs*-laser sources offer stronger signal due to more efficient two-photon excitation by higher peak power. However, they also introduce serious photo-toxicity for biological samples due to both high peak-power induced heat and high-order excitation of intrinsic fluorophores in the samples (e.g. NADPH and flavins). In addition, the large peak-power from *fs*-lasers induce stronger nonlinear non-Raman backgrounds. Moreover, the use of *fs*-lasers sacrifice the Raman spectral resolution (~ 15 cm^{-1}) due to the wide peak width (~100 cm^{-1}) of a transform-limited *fs*-laser (with a peak width of ~100 *fs*) determined by the uncertainty principle.

For all of my experiments, we chose *ps*-laser source, because: first, it is much less photo-toxic than a *fs*-laser; second, it induces much less nonlinear non-Raman background; and third, its laser peak width is similar to that of the regular Raman peak widths of chemical bonds, ensuring detection specificity.

Specifically, an integrated laser (picoEMERALD; Applied Physics & Electronics) was used as the light source for both pump and Stokes beams. PicoEMERALD provides an output pulse train at 1064 nm with a 7-ps pulse width and 80-MHz repetition rate, which serves as the Stokes beam. The frequency-doubled beam at 532 nm is used to synchronously seed a picosecond optical parametric oscillator (OPO) to produce a mode-locked pulse train (the idler beam of the OPO is blocked with an interferometry filter) with 5- to ~6-ps pulse width. The wavelength of the OPO is tunable from 720 to 990 nm, which serves as the pump beam. The intensity of the 1064 nm Stokes beam is modulated by a built-in modulator at high frequency (up to MHz) to achieve shot-noise limited detection sensitivity.

2.1.2 High-frequency modulation transfer scheme.

From Eqs. 1.26-1.27, it is obvious that the laser fluctuation noise would easily bury the SRS signal. Therefore, to ensure the optimum $(S/N)_{SRS}$ with shot-noise limited high detection sensitivity, a high-frequency (up to MHz) modulation transfer scheme is adopted to remove the laser noise that is mainly from the so-called *1/f* noise at low frequency (from DC to kilohertz), where *f* is short for frequency (Fig. 2.2a).

In the high-frequency modulation transfer scheme for SRL, the pulsed Stokes laser is intensity modulated by turning it on and off and the intensity reduction of the pulsed pump laser is detected as I_{SRL} as shown in Fig. 2.2b.

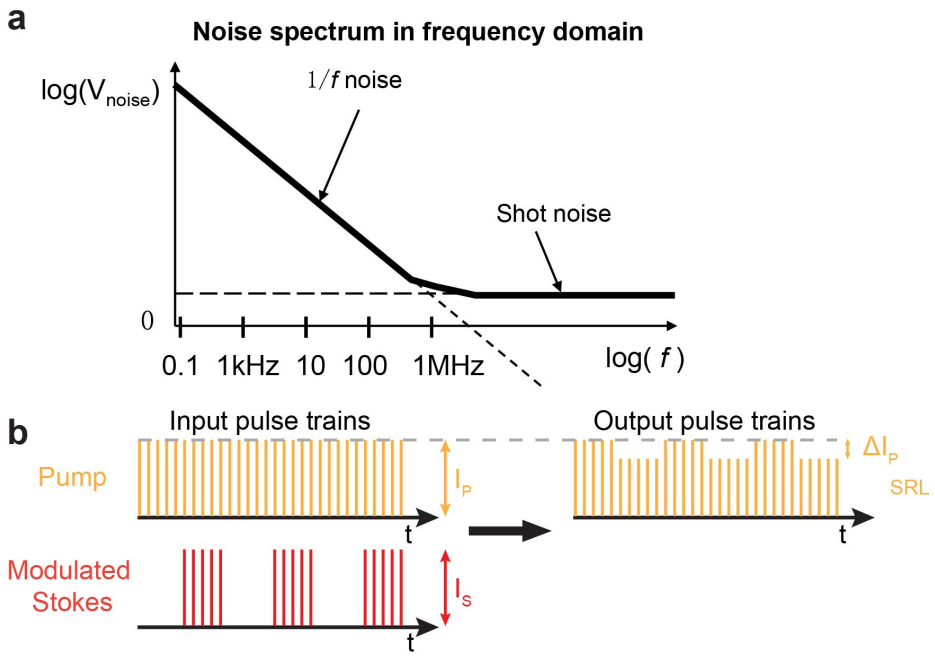

Fig. 2.2 High-frequency modulation transfer scheme enabling shot-noise limited SRS sensitivity[4]**.** (a) Noise spectrum in frequency domain for shot-noise limited signal detection. *f* is short for frequency. (b) SRS signal detection scheme of stimulated Raman loss (SRL) from the pump beam, while the pulsed Stokes beam is intensity modulated at high frequency. In the presence of the Stokes beam and when SRS transition happens, the transmitted pump beam intensity decreases. In the absence of the Stokes beam, the transmitted pump signal remains the same. Therefore, by demodulating the pump beam intensity change at the modulation frequency of the Stokes beam, the detected ΔI_P corresponds to the SRL signal.

For the choice of modulator, the higher modulation depth ensures a stronger detected signal since they are positively correlated. In our setup, we previously used an acousto-optic modulator (AOM) with a modulation frequency at 10 MHz driven by a square-wave function generator, yielding a modulation depth of more than 70%; then the modulator is updated to a built-in electro-optic modulator (EOM) modulated sinusoidally at 8 MHz with a modulation depth of more than 95%.

After passing through the modulator, the Stokes beam is then spatially overlapped with the pump beam with a dichroic mirror inside picoEMERALD. The temporal overlap between pump and Stokes pulse trains is ensured with a built-in delay stage and optimized by the SRS signal of either pure dodecane liquid or 99% heavy water (D_2O).

2.1.3 Microscope and objectives.

Pump and Stokes beams are then coupled into an inverted laser-scanning microscope (FV1000MPE; Olympus) optimized for near-IR throughput. An objective (our choices are 60× water UPlanAPO/IR, 1.2 N.A. or Olympus or XLPlan N, 1.05 N.A., MP, Olympus) with high near-IR transmission is used for biological sample imaging. The pump/Stokes beam sizes are matched to fill the back aperture of the objective. The forward-going pump and Stokes beams are collected in transmission after passing through the sample with a high N.A. condenser lens (oil immersion, 1.4 N.A.; Olympus), minimizing non-Raman artifacts. The condenser is aligned by Kohler illumination.

2.1.4 Signal detection.

There are two prerequisites for choosing a proper detector to assure the optimal signal detection. First, the detector must have fast response to follow the high modulation frequency of ~MHz to efficiently decode the laser intensity change. Second, the detector must be able to sustain high laser power with low electronic dark noise since the entire power of the pump laser is incident on the detector.

The light passing through the high N.A. condenser is then collected through a telescope used to image the scanning mirrors onto a large area (10 × 10 mm) Si photodiode (FDS1010; Thorlabs), which satisfies both aforementioned conditions, to descan beam motion during laser scanning. The current setup adopts transmitted detection on transparent samples such as mammalian cells, because SRS is a coherent process that is strongest in the forward direction.

The photodiode is reversed bias by 64 V from a DC power supply to increase both the saturation threshold and the response bandwidth. A high OD bandpass filter (890/220 CARS; Chroma Technology) is used to block the Stokes beam completely and transmit the pump beam only. The output current of the photodiode is electronically pre-filtered by an 8MHz bandpass filter (KR2724, KR Electronics) to suppress both the 80-MHz laser pulsing and the low-frequency contributions due to laser scanning across the scattering sample. It is then terminated with 50 Ω and fed into a radio frequency lock-in amplifier (SR844, Stanford Research Systems for small signal imaging that requires relative long acquisition time or HF2LI, Zurich instrument for large signals with fast image acquisition speed) to demodulate the SRL signal experienced by the pump beam. The output of the lock-in amplifier is fed back into the analog interface box (FV10-ANALOG) of the microscope converting the analog signal to digital signal. The time constant is determined by two factors. First, the signal size, because the longer the time constant, the smaller the detected noise. Second, the required imaging acquisition speed, since the imaging acquisition speed usually has to be about more than 2 times slower than the time constant for high quality image acquisition. Otherwise, the images would be

seen as retarded. For my experiments[1-3], the time constant is usually set for 20 μs, but could vary (refer to Chapter 4-5 for detailed number).

2.2 Photo-damage and non-Raman background.

Photo-damage. The major source of photo-damage at biological samples comes from the high peak power of the pulsed laser, which induces local heating on the biological samples and the high-order absorption of the intrinsic fluorophores (e.g. NADPH, FAD, etc.) inside the samples, as previously mentioned. This is also one of the major reasons why we prefer *ps*-laser to *fs*-laser. In general, we observed minimum photon damage on live biological samples when using up to 120 mW average power for each laser in our experiments from the *ps*-laser. A cell damage threshold of up to ~ 86 mW at 1100 nm by *fs* laser has been reported before[5]. To minimize such damage, one strategy (also discusses in the previous section) is to bias the use of laser power to the Stokes laser side while lowering the power from the pump laser, since the Stokes laser at 1064 nm is further into the near-infrared region offering much less photo-toxicity compared to the pump laser region from 800-950 nm[5].

Non-Raman background. SRS microscopy is essentially a pump-probe technique. Therefore, there is pump-probe related nonlinear non-Raman background besides the SRS signal with the incident pump and Stokes lasers. This non-Raman background mainly originates from cross-phase modulation, thermal lensing effects and two-photon transient absorption, deteriorating the SRS image quality (Fig. 2.3)[6]. Among the three, cross-phase modulation is a third-order virtual-state mediated nonlinear process, in which

the pump beam propagation is affected by the modulation of the Stokes laser that changes the optical refractive index of the material through the optical Kerr effect. Such an effect thus causes a non-Raman background at both on- and off- resonance Raman frequencies (Fig. 2.3a). On the other hand, thermal lensing and two-photon absorption involve real electronic transitions, which can only occur in the presence of absorbing molecules, such as hemoglobin in the blood vessel. Thermal lensing is caused by heat-induced refractive index changes after absorption of the Stokes photons, thus modulating the pump intensity (Fig. 2.3b). The appearance of two-photon transient absorption is due to the simultaneous absorption of both the pump and the Stokes photons by the absorbing molecules, thus causing an artifact of pump intensity modulation (Fig. 2.3c).

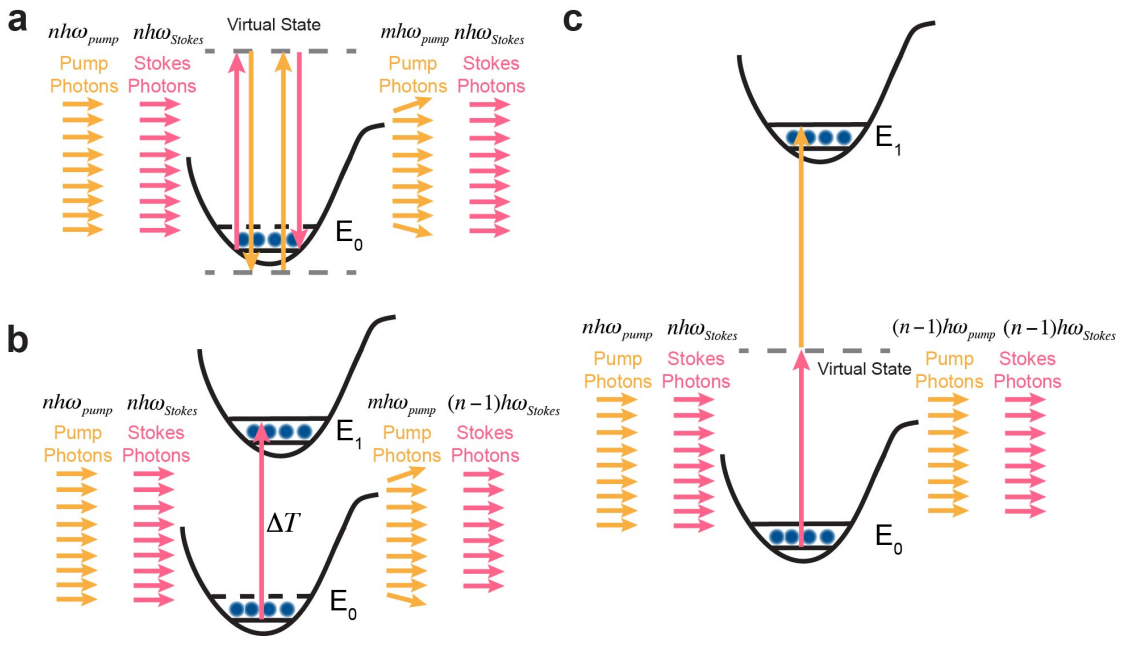

Fig. 2.3 Diagrams for non-Raman backgrounds[6]**.** (a) Cross-phase modulation induced pump photon deflection by the modulation of Stokes photon that changes the refractive index of the materials. $m < n$. (b) Thermal lensing effect caused pump photon deflection by the heating of the materials produced with the absorption of Stokes photon. $m < n$. (c) Two-photon transient absorption is from the materials that absorb each one photon from the pump and the Stokes laser.

None of the three background sources depend on Ω. Thus changing the pump laser wavelength by a few nm from the sharp on-resonance SRS signal and away to the off-resonance signal would rapidly decrease the real Raman signal while the background would remain the same. In this way, the pure SRS signal could be selectively extracted by subtraction and the background would be suppressed. This is called the spectral modulation, which could be used effectively for removing the non-Raman background. Recently, a frequency modulation scheme that switches the excitation wavelengths between modulation frequencies to minimize the background contribution has also been successfully implemented[7].

In addition, the thermal lensing effect could be sufficiently suppressed by increasing the modulation frequency, because the higher-frequency on-off modulation diminishes the effective heat accumulation. Moreover, the two-photon transient absorption background can be readily distinguished from SRG by their phase difference, since, in principle, 180° phase shift should be observed because the Stokes photons are absorbed in the two-photon transient absorption but are created in the SRG[8]. It is worth pointing out that, there may be other processes happening simultaneously along with the SRS process, but only the processes that cause pump photon loss in the presence of the stokes photons would be present as SRS background.

2.3 Advanced acquisition schemes for SRS microscopy.

Video-rate epi-SRS microscopy. Various technical modifications have been developed with the aim of specific applications since the initial report of SRS

microscopy. For example, video-rate *in vivo* imaging by backward epi-SRS detection has been implemented by directly placing the photo-detector around objective lens thus enabling SRS imaging on the non-transparent samples such as in live animals[9].

Hyper-spectral SRS microscopy. In addition, in contrast to spontaneous Raman spectroscopy that produces a Raman spectrum for data acquisition, the initial SRS microscopy focuses the entire power onto a single vibrational frequency peak for maximum signal amplification to acquire a decent image with high speed. The additional ability to swiftly acquire a SRS spectrum would also be appealing. One method of obtaining a SRS spectrum is by sweeping the OPO laser wavelength across the desired range by tuning the crystal temperature while maintaining the Stokes laser wavelength as fixed. Since the spectral acquisition rate is usually limited by how fast the crystal temperature could be adjusted, fast tuning OPO systems have been developed[10]. Besides the optimization of a *ps*-system, developments by *fs*-system have also been explored toward this goal. For example, a spectral focusing system using chirped *fs*-lasers to achieve rapid Raman spectra acquisition within one min while retaining the image quality of narrowband SRS imaging has been presented[11]. In addition, hyperspectra systems with broadband *fs* intrapulse scan have also been implemented for fast SRS spectral acquisition[7, 12].

High-speed multi-channel SRS microscopy. Simultaneous acquisition of multi-channel SRS images is highly appealing because it enables parallel analysis and correlation of different chemical species and possibly their interactions. All the

developments for rapid SRS spectra acquisition systems in the previous section could work for multiplex multi-channel SRS imaging. However, multi-channel analysis usually requires fast acquisition of a stack of imaging frames. Otherwise, the movement of samples or stages would cause spatial distortions. A parallel detection scheme has thus been proposed for multi-channel imaging by fast Fourier transform[13].

All these technical advances have facilitated the development of SRS microscopy for versatile applications. However, since its invention, SRS microscopy has almost always been implemented as a label-free technique, which is powerful, however, lacking sufficient specificity. The next two chapters focus on the specific and noninvasive imaging of small biomolecules by the coupling of SRS microscopy with small vibrational tags.

2.4 References.

1. Wei, L., Yu, Y., Shen, Y., Wang, M. & Min, W. Vibrational imaging of newly synthesized proteins in live cells by stimulated Raman scattering microscopy*, Proc. Natl. Acad. Sci. USA,* **110**, 11226-11231 (2013), *Direct Submission.*
2. Wei, L. et al. Live-cell imaging of alkyne-tagged small biomolecules by stimulated Raman Scattering, *Nat. Methods*, **11**, 410-412 (2014).
3. Wei, L. et al. Imaging complex protein metabolism in live organisms by stimulated Raman scattering microscopy with isotope labeling, *ACS Chem. Bio.* **10**, 901-908 (2015).
4. Min, W., Freudiger, C. W., Lu, S. & Xie, X. S. Coherent nonlinear optical imaging: beyond fluorescence microscopy. *Annu. Rev. Phys. Chem.* **62**, 507-530 (2011).

5. Zhang, D., Slipchenko, M. N. & Cheng, J.-X., Highly sensitive vibrational imaging by femtosecond pulse stimulated Raman loss. *J. Phys. Chem. Lett.*, **2**, 1248-1253 (2011).
6. Zhang, D., Wang, P., Slipchenko, M. N. & Cheng, J.-X., Fast Vibrational Imaging of Single Cells and Tissues by Stimulated Raman Scattering Microscopy. *Acc. Chem. Res.* **47**, 2282-2290 (2014).
7. Zhang, D., Wang, P., Slipchenko, M. N., Ben-Amotz, D., Weiner, A. M. & Cheng, J.-X. Quantitative vibrational imaging by hyperspectral stimulated Raman scattering microscopy and multivariate curve resolution analysis. *Anal. Chem.* **85**, 98−106 (2012).
8. Mansfield, J. C., Littlejohn, G. R., Seymour, M. P., Lind, R. J., Perfect, S., & Moger, J. Label-free Chemically Specific Imaging in Planta with Stimulated Raman Scattering Microscopy. *Anal. Chem.* **85**, 5055−5063 (2013).
9. Saar, B. G. et al. Video-rate molecular imaging in vivo with stimulated Raman scattering. *Science* 330, 1368–1370 (2010).
10. Kong, L., Ji, M., Holtom, G. R., Fu, D., Freudiger, C. W. & Xie, X. S. Multicolor stimulated Raman scattering microscopy with a rapidlytunable optical parametric oscillator. Opt. Lett. 38, 145−147 (2013).
11. Fu, D., Holtom, G., Freudiger, C., Zhang, X. & Xie, X. S., Hyperspectral imaging with stimulated Raman scattering by chirped femtosecond lasers. *J. Phys. Chem. B* 117, 4634-4640 (2012).
12. Ozeki, Y. et al. High-speed molecular spectral imaging of tissue with stimulated Raman scattering. *Nat. Photonics* **6**, 845−851(2012).
13. Fu, D. et al. Quantitative chemical imaging with multiplex stimulated Raman scattering microscopy. *J. Am. Chem. Soc*. **134**, 3623−3626(2012).

Chapter 3

Imaging small biomolecules in live organisms by stimulated Raman scattering microscopy coupled with alkyne tags

The contents of this chapter has been published in:

L. Wei, F. Hu, Y. Shen, Z. Chen, Y. Yu, C. -C. Lin, M. C. Wang and W. Min. "Live-cell imaging of alkyne-tagged small biomolecules by stimulated Raman Scattering", *Nat. Methods*, 11, 410 (2014).

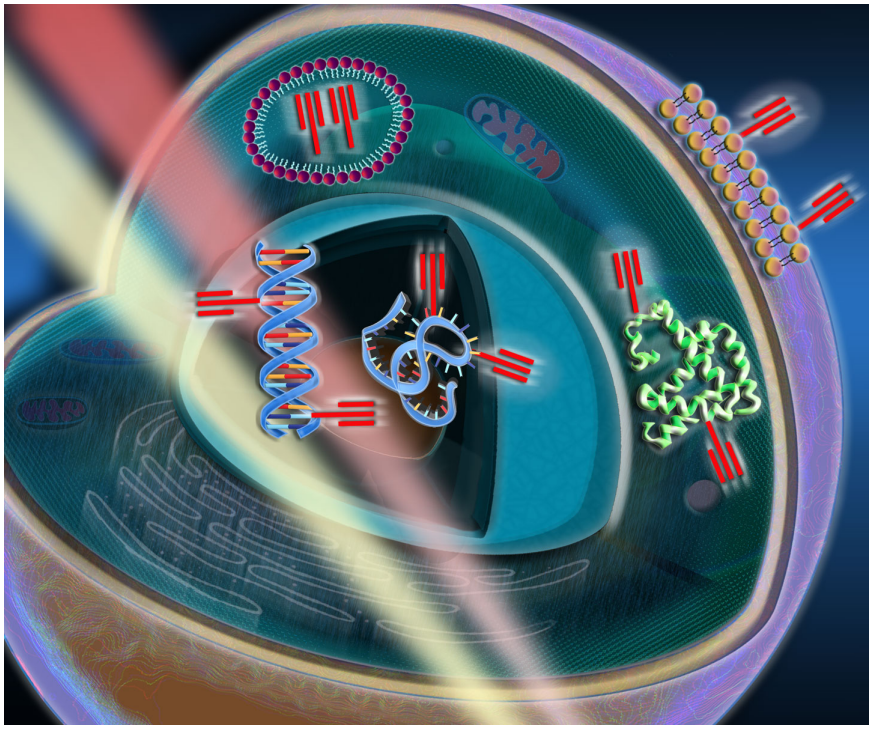

Image credit: Wei, L. /Barolini, N.

Abstract

Small biomolecules such as nucleosides, amino acids, choline, fatty acids and drugs are biologically vital species, playing indispensable roles inside cells. However, sensitive and specific visualization of these small molecules in living systems has proven to be highly challenging, despite the extensive efforts of fluorescence microscopy (hindered by bulky fluorescent tags) and label-free imaging approaches (limited by the poor detection specificity). Herein, we report the coupling of stimulated Raman scattering (SRS), an emerging label-free imaging technique, with alkyne tags (C≡C) as a general strategy for studying a broad spectrum of small biomolecules in live cells and animals. The quantum amplification, bond-selectivity, background-free and biocompatibility of SRS perfectly matches with the high polarizability, sharp Raman transition, spectral bioorthogonality and small size of the C≡C moiety, respectively. We demonstrate our technique by visualizing the metabolic incorporation processes of alkyne-tagged small molecule precursors including deoxyribonucleoside, ribonucleoside, amino acid, choline and fatty acid into newly synthesized DNA, RNA, proteomes, phospholipids and triglycerides, respectively; creating new and orthogonal vibrational colors for simultaneous multi-chemical imaging; and tracking 3D delivery of an alkyne-bearing drug in mouse skin tissues. In all of these applications, the coupling of SRS and alkyne tagging is essential to achieve superb sensitivity, specificity and biocompatibility. Hence, our technique may do for small biomolecules what fluorescence imaging of fluorophores has done for larger species, bringing small biomolecules under the illumination of modern live-cell microscopy.

3.1 Introduction.

Innovations in light microscopy have tremendously expanded our knowledge at the microscopic level. In particular, versatile fluorescence microscopy techniques, accompanied by the advent of fluorescent proteins and quantum dots[1,2], have revolutionized the way modern life science is conducted[3,4]. Common fluorescent tags, however, rely on large conjugation systems for efficient electronic transitions in the visible spectrum, dictated by quantum mechanics (the particle-in-a-box model). Consequently, the relatively bulky fluorescent tags often destroy or significantly alter the biological activities of small biomolecules. A conceptually opposite strategy is label-free imaging by utilizing intrinsic contrast such as vibrational spectroscopy[5-9]. However, label-free approaches are hindered by poor molecular selectivity. Hence, how to specifically and sensitively image small biomolecules remains highly challenging despite their immense importance in biomedicine.

To develop an effective imaging modality for small biomolecules, herein we report a general strategy by harnessing the emerging SRS microscopy coupled to alkynes (i.e., C≡C) as nonlinear vibrational tags (Fig. 3.1a). By harnessing Einstein's stimulated emission process to amplify the otherwise extremely rare spontaneous vibrational transition, SRS sensitivity makes a quantum leap over that of spontaneous Raman microscopy, capable of detecting species of much lower concentrations in three-dimensional (3D) biological samples with much higher speed[10-12]. However, since the invention of SRS microscopy, label-free imaging has been the dominating theme. Indeed, intrinsic chemical bonds such as C-H_2, C-H_3, N-C=O, C=C, O-P-O, O-H and S=O have

been explored by numerous label-free applications to image bio-molecules, including mapping the DNA, protein, lipid and cholesterol distributions[13-16]. In particular, label-free SRS imaging of lipids in combination with RNAi has been applied for screening genes that regulate fat storage in *C. elegans*[17]. In addition, label-free SRS imaging of both protein and lipids has also been applied for delineating tumor margins from normal brain tissue[15]. Despite its popularity in the chemical imaging field, label-free approach is seriously limited in two fundamental aspects[5-6]. First, the detection specificity is usually compromised. It is rather challenging to distinguish a target molecule from the sea of other species inside cells solely based on vibrational peaks from the intrinsic chemical bonds since they are largely overlapping with each other. Second, Raman cross sections of endogenous chemical bonds are usually low. Consequently, the detection sensitivity of label-free SRS is often in the range of millimolar, such as lipid droplet and myelin sheath, which is not sensitive enough for many interesting targets.

3.2 Alkynes as superb nonlinear vibrational tags for small biomolecules.

The introduction of tags thus solves both the poor selectivity and the millimolar sensitivity problems of the otherwise label-free SRS. We chose alkynes because they possess two sets of desirable features. Chemically, alkynes are small – only two atoms, exogenous – nearly non-existing inside cells, and bioorthogonal – inert to reactions with endogenous biomolecules. In fact, these properties render alkynes a key player in bioorthogonal[18] chemistry utilizing alkyne-azide cycloaddition (click-chemistry)[19]. Spectroscopically, alkynes are Raman-active with distinct characteristics – the C≡C stretching motion exhibits a substantial change of polarizability (about 40 times higher

than that of C-D)[20], displaying a sharp Raman peak around 2125 cm^{-1}, which lies desirably in a cell-silent spectral region where no other peaks from endogenous molecules exist (Fig. 3.1b). The combination of SRS with these properties would reciprocally exploit the applications of alkyne tags in bio-imaging.

We thus designed our SRS microscopy to match the alkynes' properties to achieve superb sensitivity, specificity and biocompatibility. First, by employing an additional Stokes laser to execute stimulated emission, we accelerate vibrational excitation by 10^8 times[10], rendering a quantum leap in sensitivity over the spontaneous counterpart[6]. Second, we chose a 6-ps pulse width so that the spectral width of the excitation profile fits well within that of alkyne (Fig. 3.1b). Hence, the pulse width is short enough to assure efficient nonlinear excitation, but also long enough to concentrate all laser energy exclusively on the alkyne (i.e. bond selective). Third, the background-free SRS perfectly matches with the alkynes' spectral bioorthogonality, offering purely chemical contrast[10-12], whereas spontaneous Raman and CARS severely suffer from auto-fluorescence and non-resonant background (and spectral distortion), respectively[6]. Fourth, we employ near-infrared laser wavelengths for enhanced tissue penetration, 3D sectioning and minimal photo-toxicity.

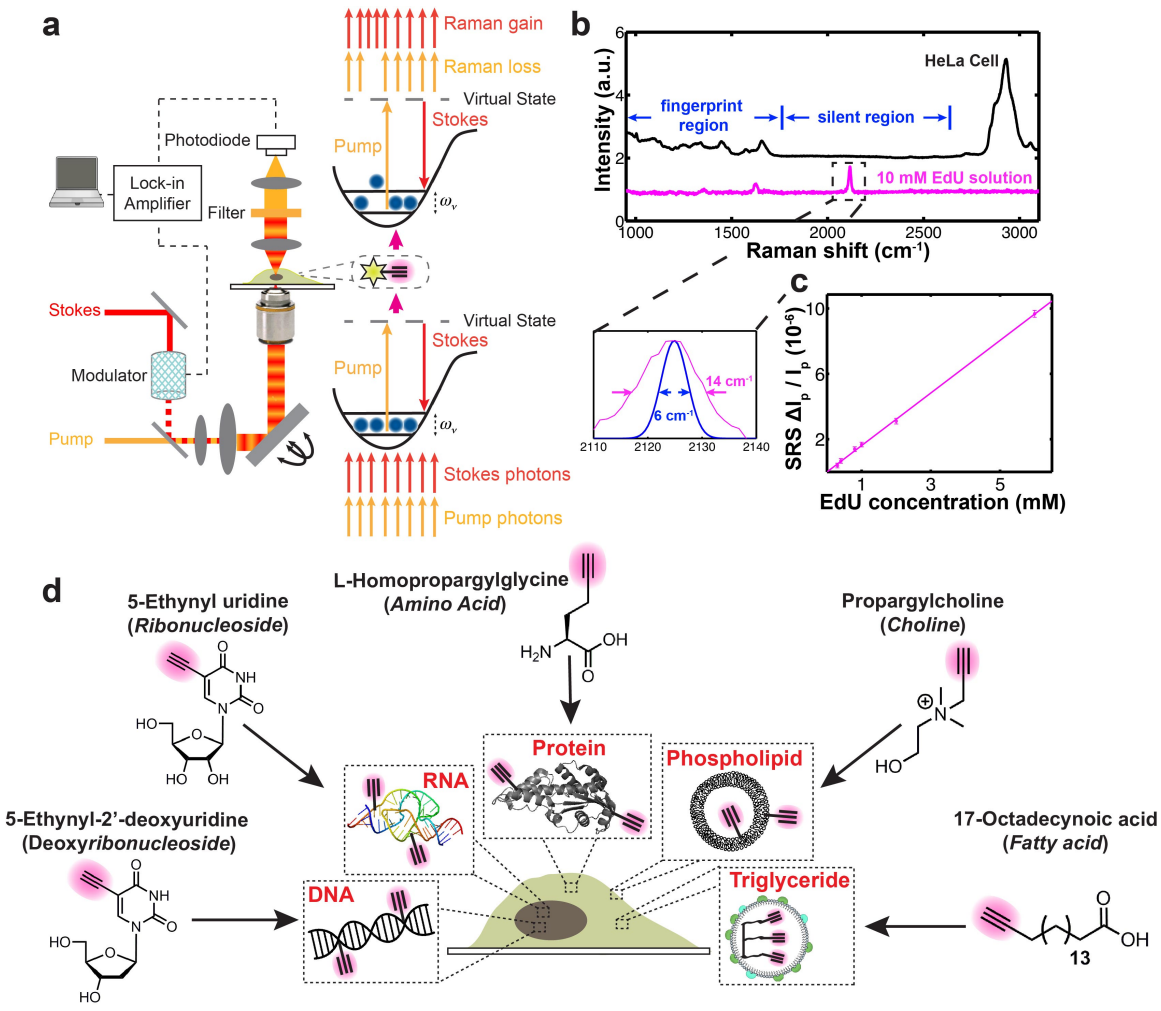

Fig. 3.1 SRS imaging of alkynes as nonlinear vibrational tags. a, Apparatus. In the resonant condition of alkyne vibration, the Pump and Stokes photons, which jointly accelerate the vibrational excitation of alkyne via SRS, experience stimulated Raman loss and Raman gain, respectively. **b,** Spontaneous Raman spectra of HeLa cells and 10 mM EdU solution. Inset: the calculated SRS excitation profile (FWHM 6 cm^{-1}, blue) is well fitted within the 2125 cm^{-1} alkyne peak (FWHM 14 cm^{-1}, magenta). **c,** Linear dependence of stimulated Raman loss signals (2125 cm^{-1}) with EdU concentrations under a 100 μs acquisition time. **d,** The metabolic incorporation scheme for a broad spectrum of alkyne-tagged small precursors.

Figure 3.1c shows the first experimental coupling of SRS with an alkyne. Taken under a fast imaging speed of 100 μs (orders of magnitude shorter than the typical acquisition time of spontaneous Raman), the detection limit is determined to be 200 μM

for 5-ethynyl-2'-deoxyuridine (EdU), an alkyne-tagged thymidine analogue (Fig. 3.1d)[21], corresponding to 12,000 alkynes within the laser focus. This is approaching the shot-noise limit ($\Delta I_p/I_p \sim 2\times10^{-7}$) of the Pump beam, exhibiting about 40 and 400 times higher sensitivity than typical bond of C-D and O-H, respectively.

3.3. The coupling of SRS microscopy with alkyne tags as a general strategy for imaging small bio-molecules.

We then pursued the general imaging applicability to a broad spectrum of small biomolecules of the alkyne-tagged deoxyribonucleoside, ribonucleoside, amino acid, choline and fatty acid (Fig. 3.1d), whose metabolic incorporation has been thoroughly tested in bioorthogonal chemistry studies[21-26]. As shown below, successful visualization of these biologically crucial precursors allows us to sensitively image the fundamental *de novo* synthesis activities of DNA, RNA, proteomes, phospholipids and triglycerides in live cells and organisms for the first time.

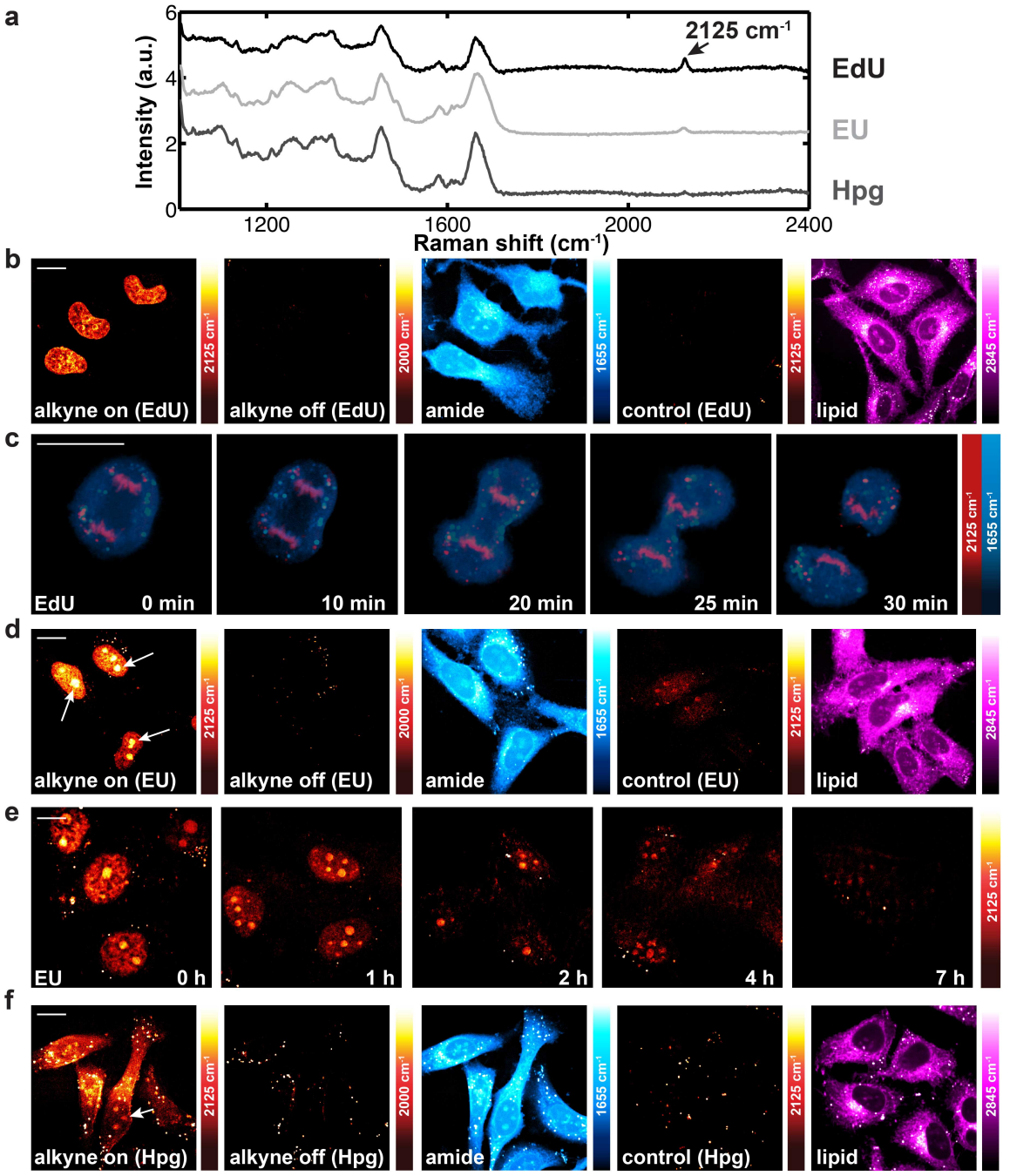

Fig. 3.2 SRS live imaging of *de novo* synthesis of DNA, RNA and proteins by metabolic incorporation of alkyne-tagged deoxyribonucleosides, ribonucleosides and amino acids into HeLa cells. a, Raman spectra of cells incubated with EdU, EU and Hpg. **b,** 2125 cm^{-1} images of live cells incubated with 100 μM EdU (alkyne-on) and with both 100 μM EdU and 10 mM hydroxyurea (Control). **c,** Time-lapse imaging of a dividing cell incubated with EdU (100 μM). **d,** 2125 cm^{-1} images of live cells incubated with 2 mM EU (alkyne-on) and with both 2 mM EU and 200 nM actinomycin D (Control). **e,** Pulse-chase imaging of RNA turnover in cells incubated

with 2 mM EU for 12 h and then changed to regular media. **f,** 2125 cm^{-1} images of live cells incubated with 2 mM Hpg (alkyne-on) and with both 2 mM Hpg and 2 mM methionine (Control). For **b**, **d** and **f**, 2000 cm^{-1} (alkyne-off) images and 1655 cm^{-1} (amide) images display the same set of cells as in the alkyne-on images; the 2845 cm^{-1} (lipid) images capture the same cells as in the control images. All images (512 × 512 pixels) were taken under a 100 μs pixel dwell time. Scale bars, 10 μm.

We first demonstrated imaging metabolic uptaking of EdU for *de novo* DNA synthesis, a signature of proliferating cells. HeLa cells grown in media with EdU show a sharp Raman peak at 2125 cm^{-1} in the cell-silent region (Fig. 3.2a). The live-cell SRS image reveals metabolic incorporation of EdU into the newly synthesized genome during the S phase of cell cycle (Fig. 3.2b, alkyne-on). The off-resonance SRS image at 2000 cm^{-1} (alkyne-off) of the same set of cells is background-free, thanks to the purely chemical contrast of SRS. No EdU signal shows up in control cells incubated with both EdU and hydroxyurea (a DNA synthesis inhibitor), whereas the 2845 cm^{-1} (lipid) image verifies normal cell morphology. Note that cellular EdU is concentrated enough to be detected even by spontaneous Raman microscopy[27,28], but with about 2,000 fold longer pixel dwell time than that of SRS (49-min for 127×127 pixels vs. 26-sec for 512×512 pixels). Hence, only SRS can offer the necessary sensitivity and desired biocompatibility for time-lapse imaging in living systems, as proved by a dividing cell incorporated with EdU being tracked every 5 min during mitosis (Fig. 3.2c) which is nearly impossible by spontaneous Raman. Therefore, our technique is useful for studying cell proliferation during development, cancer and regeneration in living organisms (Fig. 3.3), offering distinct advantages over conventional ^{3}H-dU, BrdU and EdU assays[21]. Furthermore, the fundamentally superior sensitivity of SRS over spontaneous Raman, given by the

quantum amplification of stimulated emission[10], enables us to go beyond EdU to image a broad spectrum of small biomolecules of much lower concentrations (Fig. 3.2a).

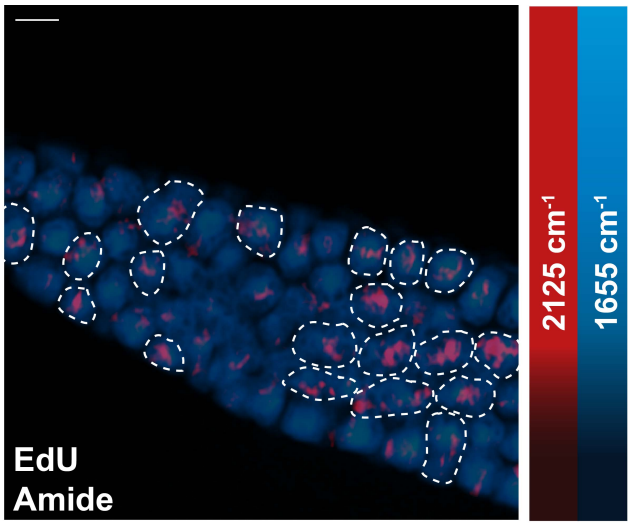

Fig. 3.3 SRS imaging of distal mitotic region of *C. elegans* germline incorporated with EdU. The composite image shows both the protein derived 1655 cm^{-1} (amide) signal from all the germ cells, and the direct visualization of alkynes (2125 cm^{-1} (EdU)) highlighting the proliferating germ cells. White circles show examples of EdU positive germ cells in the mitotic region of *C. elegans* germline. Scale bar, 5 μm.

We next probed biosynthetic labeling of 5-ethynyl uridine (EU), an alkyne-tagged uridine analogue[22], for RNA transcription and turnover (Fig. 3.1d). A 2125 cm^{-1} Raman peak is detected when HeLa cells are incubated with EU (Fig. 3.2a). The alkyne-on image (Fig. 3.2d) reveals a localized EU pattern inside the nucleus with higher abundance in the nucleoli (arrow indicated), which are major compartments of rRNA-rich ribosomal assembly. The signal nearly disappears in control cells with both EU and an RNA synthesis inhibitor, actinomycin D, validating EU incorporation into newly synthesized RNA. The turnover dynamics are further demonstrated by pulse-chase SRS imaging of EU labeled RNA (Fig. 3.2e), indicative of a short nuclear RNA lifetime (~ 3h) in live HeLa cells.

Many intricate biological processes require protein synthesis in a spatiotemporal dependent manner[29]. Here, we imaged L-Homopropargylglycine (Hpg), which is an alkyne-tagged analogue of methionine[23] (an essential amino acid), to visualize the newly synthesized proteome (Fig. 3.1d). HeLa cells growing in the Hpg supplemented methionine-deficient media display a 2125 cm^{-1} alkyne peak (Fig. 3.2a). The corresponding alkyne-on image (Fig. 3.2f) shows the distribution of newly synthesized proteins with spatial enrichment in the nucleoli (arrow indicated), which involve rapid proteomic exchange[30]. The signal is well retained in HeLa cells that were incubated with Hpg and then fixed (Fig. 3.4), indicating that freely diffusive Hpg precursor has little contribution to detected signal. Furthermore, by adding methionine to compete with Hpg, the signal disappears as expected (control, Fig. 3.2f), since methionine is incorporated 500-times faster than Hpg by the aminoacyl tRNA synthetase[23,29]. This is the first time that an unnatural amino acid[29,31] is detected in live cells by vibrational microscopy, going beyond the conventional fluorescence-based protein imaging.

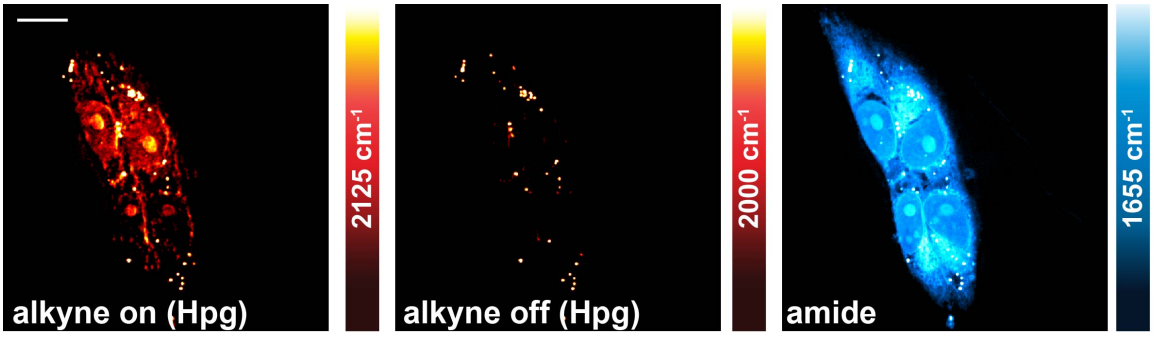

Fig. 3.4 SRS imaging of fixed HeLa cells after incorporating with 2 mM Hpg. The 2125 cm^{-1} (alkyne-on) image displays the Hpg distribution for the newly synthesized proteins. For the same set of cells, the off-resonant (alkyne-off) image shows vanishing signal, and the 1655 cm^{-1} (amide) image shows total protein distribution. This result confirms that the detected signal is not from freely diffusive precursor Hpg itself (which is eliminated during the fixation process). Scale bar, 10 μm.

We then monitored metabolic incorporation of alkyne-tagged choline and fatty acids, respectively (Fig. 3.1d). By incubating hippocampal neurons with propargylcholine, a clear 2142 cm^{-1} Raman peak emerges (Fig. 3.5a). Such a frequency shift from 2125 cm^{-1} is due to the positive charge on the nearby nitrogen (Fig. 3.1d). As revealed by enzymatic assays (Fig. 3.6), the alkyne-on signal (Fig. 3.5b) mainly originates from newly synthesized choline phospholipids, which are major structural components of membranes and critical players in cell signaling[24]. For fatty acids, we incubated 17-octadecynoic acid with THP-1 macrophages, which actively scavenge cholesterol and fatty acids[32]. The alkyne-on image (Fig. 3.5c) depicts intracellular formation of numerous lipid droplets, indicative of transformation into foam cells, a hallmark of early atherosclerosis. To further demonstrate on multi-cellular organisms, *C. elegans* fed with 17-octadecynoic acid displays a distribution of newly up-taken fatty acids which mainly exist in the form of triglycerides inside lipid droplets (alkyne-on, Fig. 3.5d). Such a fat accumulation process could serve as a useful model for studying obesity and diabetes[33].

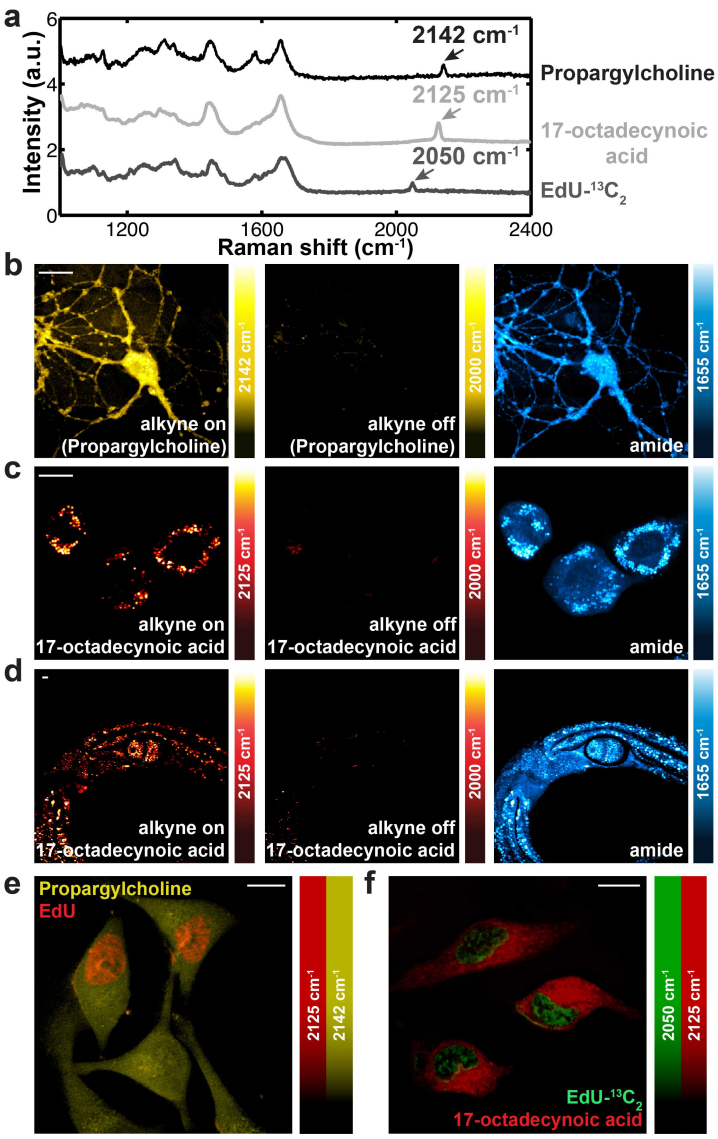

Fig. 3.5 SRS live imaging of metabolic incorporation of alkyne-tagged choline and fatty acid, and multi-color alkyne imaging. a, Raman spectra of hippocampal neurons incubated with propargylcholine, macrophages with 17-octadecynoic acid and HeLa cells with EdU-$^{13}C_2$. **b,** 2142 cm^{-1} image of live neurons incubated with 1 mM propargylcholine (alkyne-on). **c,** 2125 cm^{-1} image of live macrophages incubated with 400 μM 17-octadecynoic acid (alkyne-on). **d,** 2125 cm^{-1} image of *C. elegans* fed with 17-octadecynoic acid (alkyne-on). For **b-d**, 2000 cm^{-1} (alkyne-off) images and 1655 cm^{-1} (amide) images display the same set of cells as in the alkyne-on images. **e-f,** Dual-color SRS images of EdU (2125 cm^{-1}, red) with propargylcholine (2142 cm^{-1}, yellow), and EdU-$^{13}C_2$ (2050 cm^{-1}, green) with 17-octadecynoic acid (2125 cm^{-1}, red) in live HeLa cells. All images (512 × 512 pixels) were taken under a 100 μs pixel dwell time. Scale bars, 10 μm.

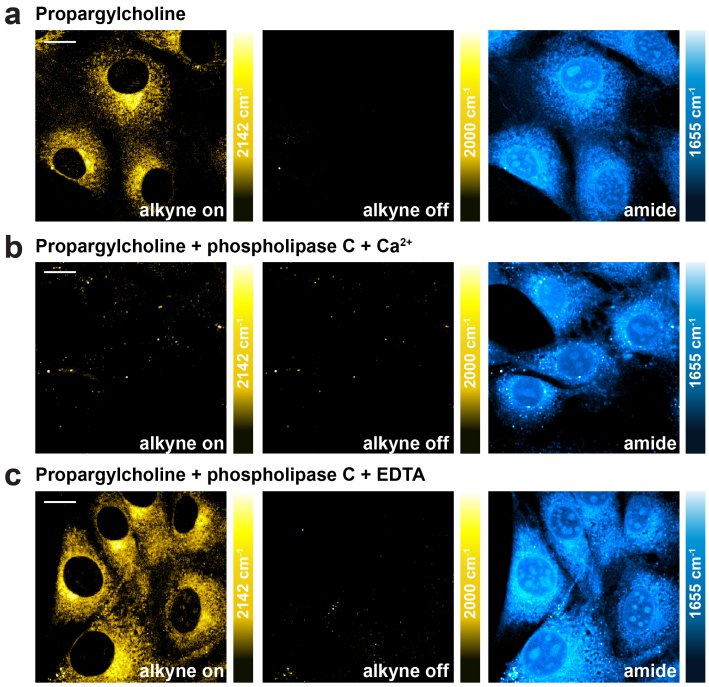

Fig. 3.6 SRS imaging of propargylcholine incorporation in NIH3T3 cells and control experiments. a, Fixed NIH3T3 cells after culturing with 0.5 mM propargylcholine for 48 hours. The 2142 cm^{-1} (alkyne-on) image shows alkyne-tagged choline distribution. **b,** Treatment of fixed NIH3T3 cells with phospholipase C, which removes Choline head groups of phospholipids only in the presence of calcium. The alkyne-on image shows the strong decrease of incorporated propargylcholine signal, supporting its main incorporation into membrane phospholipids. **c,** Treatment of fixed NIH3T3 cells with phospholipase C in the presence of EDTA (chelating calcium). Propargylcholine signal is retained in the alkyne-on image. For **a-c**: in the same set of cells as in alkyne-on images, the 2000 cm^{-1} (alkyne-off) images show a clear background. The 1655 cm^{-1} (amide) images display total protein distribution. Scale bars, 10 μm.

We note that extensive bioorthogonal chemistry studies have used azide-tagged fluorophores to stain the above alkyne-tagged precursors for imaging applications[21-26]. Unfortunately, this click-chemistry based detection usually requires either bulky cyclooctynes (for copper-free) or non-physiological cell fixation (for copper-catalyzed) and subsequent dye staining and washing (Fig. 3.7). Our approach, on the contrary, is

capable of direct visualization of alkyne-tagged small molecules in living systems under physiological conditions.

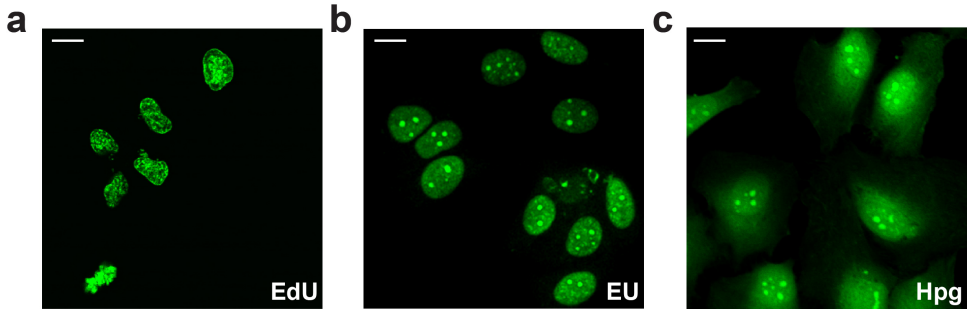

Fig. 3.7 Click chemistry-based fluorescence staining of fixed HeLa cells. Fluorescence images of HeLa cells incorporated with **a,** EdU (for DNA); **b,** EU (for RNA); **c,** Hpg (for protein). Scale bars, 10 μm.

3.4 Multi-color vibrational palettes.

Inspired by the color palettes of fluorescent tags[1,2], we attempted to expand the vibrational "colors" of alkyne tags to enable simultaneous multi-chemical imaging. One immediate approach is to use the local environmental effect to shift the alkyne Raman frequency, as shown in the dual-color image (Fig. 3.5e) of propargylcholine (2142 cm^{-1}) and EdU (2125 cm^{-1}). A more general strategy is to employ isotopes with different masses. Since the vibrational frequency, ω_v, is related to the reduced mass m of the oscillator via $\omega_v \propto \sqrt{1/m}$, a heavier $^{13}C\equiv^{13}C$ should vibrate at a lower frequency of 2042 cm^{-1}. We synthesized EdU-$^{13}C_2$ and measured its Raman frequency to be 2050 cm^{-1} (Fig. 3.5a). Thanks to alkynes' sharp Raman transition, this new peak of $^{13}C\equiv^{13}C$ is clearly resolved from the original one at 2125 cm^{-1}. Hence, comparing to C-D labeling, alkyne tags are not only much stronger (considering there can only be a limited number of C-D on small molecules), but also amenable to multiplexing. Dual-color imaging of 17-

octadecynoic acid (2125 cm^{-1}) in the cytoplasm and EdU-$^{13}C_2$ (2050 cm^{-1}) in the nucleus (Fig. 3.5f) thus paves the way for simultaneous visualization of multiple vibrational "colors". The EdU-$^{13}C{\equiv}^{12}C$ have been synthesized as well, with a vibrational peak at 2077 cm^{-1}, well resolved from peaks as to EdU-$^{13}C{\equiv}^{13}C$ and the original EdU-$^{12}C{\equiv}^{12}C$, enabling 4-color vibrational imaging. The simultaneous imaging of EU-$^{13}C{\equiv}^{13}C$ labeling newly synthesized RNA, EdU-$^{12}C{\equiv}^{12}C$ labeling newly synthesized DNA and 17-octadecynoic acid of newly taken up fatty acids has also been demonstrated[34].

3.5 Imaging the pharmacokinetics of the alkyne-tagged small molecule drugs by SRS microscopy.

Finally, we tracked alkyne-bearing drug delivery in animal tissues by taking advantage of SRS's intrinsic 3D optical sectioning that is unachievable by spontaneous Raman. Comparing to bulky fluorophores which usually perturb pharmacokinetics, alkynes have little such adverse effect and are common moieties in many pharmaceuticals[35]. We chose terbinafine hydrochloride (TH), a FDA approved alkyne-bearing antifungal skin drug[36], for 3D tissue imaging. Fig. 3.8b-e reveal the drug delivery pathways in mouse ear tissue by imaging the internal alkyne at 2230 cm^{-1} (Fig. 3.8a) in TH. At the stratum corneum layer (Fig. 3.8b), TH exhibits a brighter contrast at cell edges, similar to that of the lipid channel. At the viable epidermis layer (Fig. 3.8c), TH accumulates only in the oily hair coating, whereas most cell bodies and hair keratin are mainly highlighted in the protein channel. With increasing depths, TH is highly enriched in the sebaceous gland (Fig. 3.8d) and subcutaneous fat cells (Fig. 3.8e), closely resembling the lipid patterns. These observations suggest that TH penetrates into tissues

through the lipid instead of the protein phase, which is consistent with the lipophilic nature of TH. Our technique should be generally applicable to tracking many other drugs after proper alkyne derivatization.

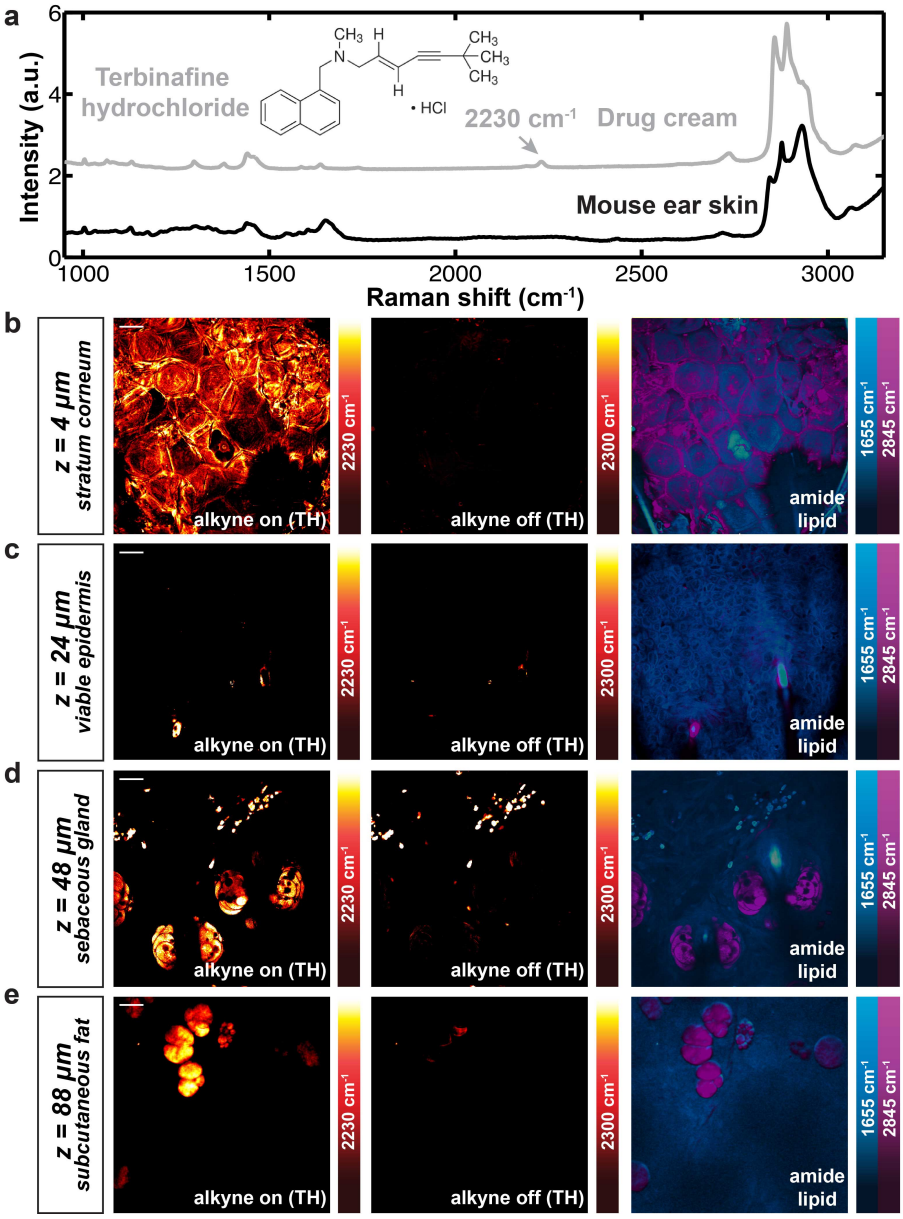

Fig. 3.8 ***In vivo*** **delivery of an alkyne-bearing drug into mouse ear. a,** Raman spectra of a drug cream containing 1% TH and mouse ear skin tissue. **b-e,** SRS imaging of tissue layers from stratum corneum (z = 4 μm) to viable epidermis (z = 24 μm), sebaceous gland (z = 48 μm) and subcutaneous fat (z = 88 μm). To facilitate tissue penetration, DMSO solution containing 1% TH was applied onto the ears of an anesthetized live mouse for 30 min and the dissected ears are

imaged afterwards. Similar results are obtained with the drug cream (Fig. 3.9). For all 4 layers: 2230 cm^{-1} (alkyne-on) images display TH penetration; 2300 cm^{-1} (alkyne-off) images show off-resonant background (The bright spots in **d** are due to two-photon absorption of red blood cells). The composite images show protein (1655 cm^{-1}) and lipid (2845 cm^{-1}) distributions. All images (512 × 512 pixels) were taken under a 100 μs pixel dwell time. Scale bars, 20 μm.

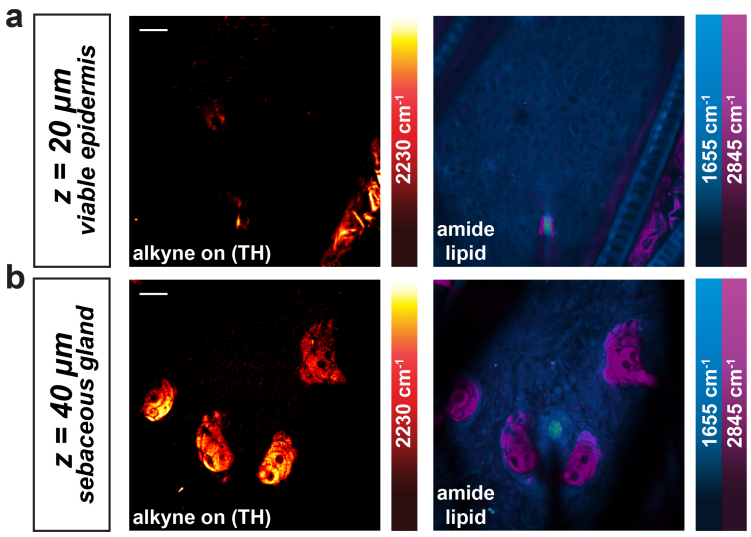

Fig. 3.9 *In vivo* delivery of an alkyne-bearing drug (TH in Lamisil cream) into mouse ear. (**a**-**b**) SRS imaging of the viable epidermis layer (z = 20 μm) and the sebaceous gland layer (z = 40 μm). For both **a** and **b**: the 2230 cm^{-1} (alkyne-on) images display the TH penetration into mouse ear tissues through lipid phase. The composite images show both protein (1655 cm^{-1}) and lipid (2845 cm^{-1}) distributions. Scale bars, 20 μm.

3.6 Conclusion and discussion.

The above applications demonstrate the general applicability of our technique in live cells and animals. Technically, our work equips a small non-fluorescent tag onto a powerful but otherwise label-free vibrational microscopy, extending the repertoire of bio-imaging modalities beyond fluorescence and label-free approaches. Application-wise, SRS imaging of alkynes may do for small biomolecules what fluorescence imaging of fluorophores has done for larger species, thus bringing these small targets under the illumination of modern live-cell microscopy.

Recently, the coupling of SRS microscopy with alkyne tags has been applied to imaging the uptake of glucose, a small molecule and a major energy source for living organisms, in live cells and tissues, thus laid foundation for studying the energy demands in living systems[37].

3.7 Materials and sample preparation.

Materials. 5-Ethynyl-2'-deoxyuridine (EdU) (T511285), 17-Octadecynoic acid (17-ODYA) (O8382), DMEM medium without L-methionine, L-cystine and L-glutamine (D0422), L-methionine (M5308), L-cystine (C7602), 2-Mercaptoethanol (M3148) and Phorbol 12-myristate 13-acetate (P1585) were purchased from Sigma-Aldrich. 5-Ethynyl Uridine (EU) (E-10345), Homopropargylglycine (Hpg) (C10186), Alexa Fluor® 488 Azide (A10266), Click-iT® Cell Reaction Buffer Kit (C10269), DMEM medium (11965), FBS (10082), penicillin/streptomycin (15140), L-glutamine (25030), Neurobasal A Medium (10888) and B27 supplement (17504) were purchased from Invitrogen. RPMI-1640 Medium (30-2001) was purchased from ATCC. BCS (hyclone SH30072) was purchased from Fisher Scientific.

DMEM culture medium was made by adding 10% (vol/vol) FBS and 1% (vol/vol) penicillin/streptomycin to the DMEM medium. Methionine-deficient culture medium was made by supplying 4 mM L-glutamine, 0.2 mM L-cystine, 10% FBS and 1% penicillin/streptomycin to the DMEM medium without L-methionine, L-cystine and L-glutamine. RPMI-1640 culture medium was made of supplying the RPMI-1640 medium with 10% FBS, 1% penicillin/streptomycin and 50 μM 2-Mercaptoethanol. Neuron

culture medium was made of Neurobasal A Medium adding with 1X B27 supplement and 0.5 mM glutamine. Culture medium for NIH3T3 cells was made by adding 10% (vol/vol) BCS and 1% (vol/vol) penicillin/streptomycin to the DMEM medium.

Propargylcholine synthesis. Propargylcholine was synthesized according to reference (10). 3 mL propargyl bromide (80 wt. % solution in toluene) were added dropwise to 3 g 2-dimethylaminoethanol in 10 mL anhydrous THF on ice under argon gas protection and stirring. The ice bath was removed and the mixture was kept stirring at room temperature overnight. The white solids were filtered the next day and washed extensively with cold anhydrous THF to obtain 5 g pure propargylcholine bromide. All chemicals here are purchased from Sigma-Aldrich. NMR spectrum was recorded on a Bruker 400 (400MHz) Fourier Transform (FT) NMR spectrometers at the Columbia University Chemistry Department. ^{1}H NMR spectra are tabulated in the following order: multiplicity (s, singlet; d, doublet; t, triplet; m, multiplet), number of protons. ^{1}H NMR (400 MHz, D_2O) δ ppm: 4.37 (d, J = 2.4 Hz, 2H); 4.10 (m, 2H); 3.66 (t, J = 4.8 Hz, 2H); 3.28 (s, 6H); MS (APCI+) m/z Calcd. for $C_7H_{14}NO$ $[M]^+$:128.19. Found: 128.26.

Sample preparation for SRS imaging of live cells and organisms. For all SRS imaging experiments of HeLa cells (Fig. 3.2), cells were first seeded on coverslips with a density of 1×10^5/mL in petri dishes with 2 mL DMEM culture medium for 20 h at 37 °C and 5% CO_2. For EdU experiment, DMEM culture medium was then changed to DMEM medium (FBS-free) for 24 h for cell cycle synchronization. After synchronization, medium was replaced back to DMEM culture medium and EdU (10 mM stock in PBS)

was simultaneously added to a concentration of 100 μM for 15 h. For EU experiment, EU (100 mM stock in PBS) was added to the DMEM culture medium directly to a concentration of 2 mM for 7 h. For Hpg experiment, DMEM culture medium was then changed to methionine-deficient culture medium for 1 h, followed by supplying 2 mM Hpg (200 mM stock in PBS) in the medium for 24 h. For propargylcholine and EdU dual-color experiment, DMEM culture medium was changed to DMEM medium (FBS-free) for synchronization. After synchronization, medium was replaced back to DMEM culture medium by simultaneously adding both propargylcholine (25 mM stock in PBS) and EdU (10 mM stock in PBS) to the culture medium to a concentration of 1 mM and 100 μM, respectively, for 24 h. For the propargylcholine experiment in neurons, hippocampal neurons were cultured on coverslips in 1 ml neuron culture medium for 14 d, and then propargylcholine (25 mM stock in PBS) is directly added into the medium to a final concentration of 1 mM for 24 h. For the 17-ODYA experiment in macrophages, THP-1 cells were first seeded on coverslips at a density of 2×10^5/mL in 2 ml RPMI-1640 culture medium for 24 h, followed by 72 h induction of differentiation to macrophages by incubating with 100 ng/ml Phorbol 12-myristate 13-acetate (PMA) in the medium. Medium was then replaced with RPMI-1640 culture medium containing 400 μM 17-ODYA (6:1 complexed to BSA) for 15 h.

For all of the above experiments, after incubation, the coverslip is taken out to make an imaging chamber filled with PBS for SRS imaging.

For the 17-ODYA experiment in *C. elegans*, OP50 bacterial culture was mixed well with 4 mM 17-ODYA (from 100 mM ethanol stock solution), and then seeded onto nematode growth media (NGM) plates. After drying the plates in hood, wild type N_2 day 1 adult *C. elegans* were placed onto the plates and fed for 40 h. *C. elegans* were then mounted on 2% agarose pads containing 0.1% NaN_3 as anesthetic on glass microscope slides for SRS imaging.

SRS imaging of *C. elegans* germline after feeding with EdU. MG1693 (thymidine defective MG1655) *E. Coli* strain was cultured in 2 ml LB medium at 37 °C overnight, and transferred to 100 ml of M9 medium containing 400 μM EdU for further growth at 37 °C for 24 h. The EdU-labeled MG1693 *E. Coli* was then seeded on M9 agar plate. Synchronized day 1 adult worms developed in 20 °C were transferred to EdU-labeled bacterial plate for 3 h, and then were dissected to take out the germline for imaging (Fig. 3.3).

Enzymatic assays confirming propargylcholine incorporation into cellular choline phospholipids. We design our control experiments according to the click chemistry based assays reported in Ref. 24 (Fig. 3.6). NIH 3T3 cells cultured with 0.5 mM propargylcholine for 48 hours were fixed with 4 % PFA for 15 minutes, rinsed with 1 mL TBS buffer twice and incubated with 1 mL 1 mg/mL BSA in TBS buffer for 1 hour at 37 °C, with or without 0.02 U/mL phospholipase C (Type XIV from *Clostridium perfringens*, Sigma), in the presence of 10 mM $CaCl_2$ (required for phospholipase C

activity) (Fig. 3.6b) or 10 mM EDTA (Fig. 3.6c). The cells were then washed with TBS buffer and ready for SRS imaging.

Cell preparation for click chemistry-based fluorescence microscopy. All experiments (Fig. 3.7) were carried out following the manufacturer's protocol from Invitrogen. HeLa cells were first incubated with 10 μM EdU in DMEM culture medium for 24 h, or 1 mM EU in DMEM culture medium for 20 h, or 1 mM Hpg in methionine-deficient culture medium for 20h, respectively. Cells were then fixed in 4% PFA for 15 min, washed twice with 3% BSA in PBS, permeabilized with 0.5% Triton PBS solution for 20 min, and performed click chemistry staining using Alexa Fluor 488 Azide in the Click-iT Cell Reaction Buffer Kit for 30 min. After washing with 3% BSA in PBS for three times, fluorescence images were obtained using an Olympus FV1200 confocal microscope with 488nm laser excitation while the cells were immersed in PBS solution.

Sample preparation for drug delivery into mouse ear tissues. Either DMSO solution or Drug cream (Lamisil, Novartis) containing 1% (w/w) active terbinafine hydrochloride (TH) was applied to the ears of an anesthetized live mouse (2-3 weeks old white mouse of either sex) for 30 min, and the dissected ears from the sacrificed mouse were then imaged by SRS (Figs. 3.8 and 3.9). The amide (1655 cm^{-1}) and lipid (2845 cm^{-1}) images have been applied with linear spectral unmixing to eliminate cross talk before composition. The experimental protocol for drug delivery on mice (AC-AAAG4703) was approved by Institutional Animal Care and Use Committee at Columbia University.

3.8 Instrumentation Summary.

Stimulated Raman scattering (SRS) microscopy. More detailed descriptions are provided in Chapter 2. An integrated laser system (picoEMERALD, Applied Physics & Electronics, Inc) was chosen as the light source for both the tunable Pump beam and the Stokes beam fixed at 1064nm (5~6 ps pulse width and 80 MHz repetition rate). The intensity of the Stokes beam is being modulated at 8 MHz by a built-in electro-optic modulator to reject the slower mechanical, electric and Pump laser noise. Collinear Pump and Stokes beams are spatially combined, temporally synchronized, and then focused by a water immersion objective (NA=1.2) onto the focal spot. The transmitted Pump beam is collected by an oil condenser (NA=1.4), de-scanned and spectrally filtered before being detected by a large-area photodiode. A RF lock-in amplifier (SR844, Stanford Research) was used to demodulate the stimulated Raman loss signal with a 10 μs time constant. All the SRS images are acquired by a laser scanning multiphoton microscope (FV1200, Olympus) with a pixel dwell time of 100 μs.

Spontaneous Raman Spectroscopy. The spontaneous Raman spectra were acquired using a laser confocal Raman microscope (Xplora, Horiba Jobin Yvon) at room temperature. A 12 mW (after the microscope objective), 532 nm diode laser was used to excite the sample through a 50X, N.A.=0.75 air objective (MPlan N, Olympus). The total data acquisition time was 300 s using the LabSpec 6 software. All the spontaneous Raman spectra have subtracted the PBS solution background.

3.9 References.

1. Zhang, J., Campbell, R. E., Ting, A.Y. & Tsien, R. Y. Creating new fluorescent probes for cell biology. *Nat. Rev. Mol. Cell Biol.* **3**, 906-918 (2002).
2. Michalet, X. et al. Quantum dots for live cells, in vivo imaging, and diagnostics. *Science* **307**, 538-544 (2005).
3. Pawley, J. B. (ed.) *Handbook of biological confocal microscopy* (Springer, 2006).
4. Yuste, R. (ed.) *Imaging: a laboratory manual* (Cold Spring Harbor Press, 2010).
5. Sasic, S. & Ozaki, Y. (eds.) *Raman, infrared, and near-infrared chemical imaging* (Wiley, 2011).
6. Cheng, J. -X. & Xie, X. S. *Coherent Raman Scattering Microscopy* (CRC Press, 2012).
7. Masters, B. R. & So, P. T. C. (eds.) *Handbook of biomedical nonlinear optical microscopy* (Oxford University Press, 2008).
8. Olivier, N. et al. Cell lineage reconstruction of early zebrafish embryos using label-free nonlinear microscopy. *Science* **329**, 967-971 (2010).
9. Huang, D. et al. Optical coherence tomography. *Science* **254**, 1178-1181 (1991).
10. Min, W., Freudiger, C. W., Lu, S. & Xie, X. S. Coherent nonlinear optical imaging: beyond fluorescence microscopy. *Annu. Rev. Phys. Chem.* **62**, 507-530 (2011).
11. Freudiger, C. W. et al. Label-free biomedical imaging with high sensitivity by stimulated Raman scattering microscopy. *Science* **322**, 1857-1861 (2008).
12. Saar, B. G. et al. Video-rate molecular imaging in vivo with stimulated Raman scattering. *Science* **330**, 1368-1370 (2010).
13. Zhang, X. et al. *ChemPhysChem* **13**, 1054-1059 (2012).
14. Freudiger, C. W. et al. Multicolored stain-free histopathology with coherent Raman imaging. *Lab. Invest.* 92, 1492-1502 (2012).
15. Ji, M. et al. Rapid, label-free detection of brain tumors with stimulated Raman scattering microscopy. *Sci. Transl. Med.* **5**, 201ra119-201ra119 (2013).
16. Wang, P., Liu, B., Zhang, D., Belew, M. Y., Tissenbaum, H. A., & Cheng, J.-X., Imaging Lipid Metabolism in Live Caenorhabditis elegans Using Fingerprint Vibrations. *Angew. Chem., Int. Ed.* **53**, 11787 –11792 (2014).

17. Wang, M. C., Min, W., Freudiger, C. W., Ruvkun, G., & Xie, X. S., RNAi screening for fat regulatory genes with SRS microscopy. *Nat. Methods* **8**, 135-138 (2011).
18. Prescher, J. A. & Bertozzi, C. R. Chemistry in living systems. *Nat. Chem. Biol.* **1**, 13-21 (2005).
19. Kolb, H. C., Finn, M. G. & Sharpless, K. B. Click chemistry: diverse chemical function from a few good reactions. *Angew. Chem. Int. Ed.* **40**, 2004-2021 (2001).
20. Lin-Vien, D., Colthup, N. B., Fateley, W. G. & Grasselli, J. G. T*he Handbook of Infrared and Raman Characteristic Frequencies of Organic Molecules* (Academic Press, 1991).
21. Salic, A. & Mitchison, T. J. A chemical method for fast and sensitive detection of DNA synthesis in vivo. *Proc. Natl. Acad. Sci. USA* **105**, 2415-2420 (2008).
22. Jao, C. Y. & Salic, A. Exploring RNA transcription and turnover in vivo by using click chemistry. *Proc. Natl. Acad. Sci. USA* **105**, 15779-15784 (2008).
23. Beatty, K. E. et al. Fluorescence visualization of newly synthesized proteins in mammalian cells. *Angew. Chem. Int. Ed.* **45**, 7364-7367 (2006).
24. Jao, C. Y., Roth, M., Welti, R. & Salic, A. Metabolic labeling and direct imaging of choline phospholipids in vivo. *Proc. Natl. Acad. Sci. USA* **106**, 15332-15337 (2009).
25. Hang, H. C., Wilson, J. P. & Charron, G. Bioorthogonal chemical reporters for analyzing protein lipidation and lipid trafficking. *Acc. Chem. Res.* **44**, 699-708 (2011).
26. Baskin, J. M. et al. Copper-free click chemistry for dynamic in vivo imaging. *Proc. Natl. Acad. Sci. USA* **104**, 16793-16797 (2007).
27. Yamakoshi, H. et al. Imaging of EdU, an alkyne-tagged cell proliferation probe, by Raman microscopy. *J. Am. Chem. Soc.* **133**, 6102-6105 (2011).
28. Yamakoshi, H. et al. Alkyne-tag Raman imaging for visualization of mobile small molecules in live cells. *J. Am. Chem. Soc.* **134**, 20681-20689 (2012).
29. Ngo, J. T. & Tirrell, D. A. Noncanonical amino acids in the interrogation of cellular protein synthesis. *Acc. Chem. Res.* **44**, 677-685 (2011).
30. Andersen, J. S. et al. Nucleolar proteome dynamics. *Nature* **433**, 77-83 (2005).
31. Liu, C. C. & Schultz, P. G. Adding new chemistries to the genetic code. *Annu. Rev. Biochem.* **79**, 413-444 (2010).

32. Moore, K. J. & Tabas, I. Macrophages in the pathogenesis of atherosclerosis. *Cell* **145**, 341-355 (2011).
33. Ashrafi, K. et al. Genome-wide RNAi analysis of Caenorhabditis elegans fat regulatory genes. *Nature* **421**, 268-272 (2003).
34. Chen, Z.; Paley, D. W.; Wei, L.; Weisman, A. L.; Friesner, R. A.; Nuckolls, C.; Min, W., Multicolor Live-Cell Chemical Imaging by Isotopically Edited Alkyne Vibrational Palette. *J. Am. Chem. Soc.* **2014,** *136* (22), 8027–8033.
35. Christiansen, E. et al. Identification of a potent and selective free fatty acid receptor 1 (FFA1/GPR40) agonist with favorable physicochemical and in vitro ADME properties. *J. Med. Chem.* **54**, 6691-6703 (2011).
36. Balfour, J. A. & Faulds, D. Terbinafine. A review of its pharmacodynamic and pharmacokinetic properties, and therapeutic potential in superficial mycoses. *Drugs* **43**, 259-284 (1992).
37. Hu, F., Chen, Z., Zhang, L., Shen, Y., Wei, L. & Min, W., Vibrational Imaging of Glucose Uptake Activity in Live Cells and Tissues by Stimulated Raman Scattering. *Angew. Chem., Int. Ed.* **54**, 9821-9825 (2015).

Chapter 4

Probing complex protein metabolism in live systems by stimulated Raman scattering microscopy with deuterium tags

The contents of this chapter has been published in:

L. Wei, Y. Yu, Y. Shen, M. Wang and W. Min, "Vibrational imaging of newly synthesized proteins in live cells by stimulated Raman scattering microscopy", *Proc. Natl. Acad. Sci. USA,* 110, 11226 (2013), *Direct Submission.*

L. Wei, Y. Shen, F. Xu, F. Hu, J. K. Harrington, K. L. Targoff and W. Min. "Imaging complex protein metabolism in live organisms by stimulated Raman scattering microscopy with isotope labeling", *ACS Chem. Bio.* 10, 901 (2015).

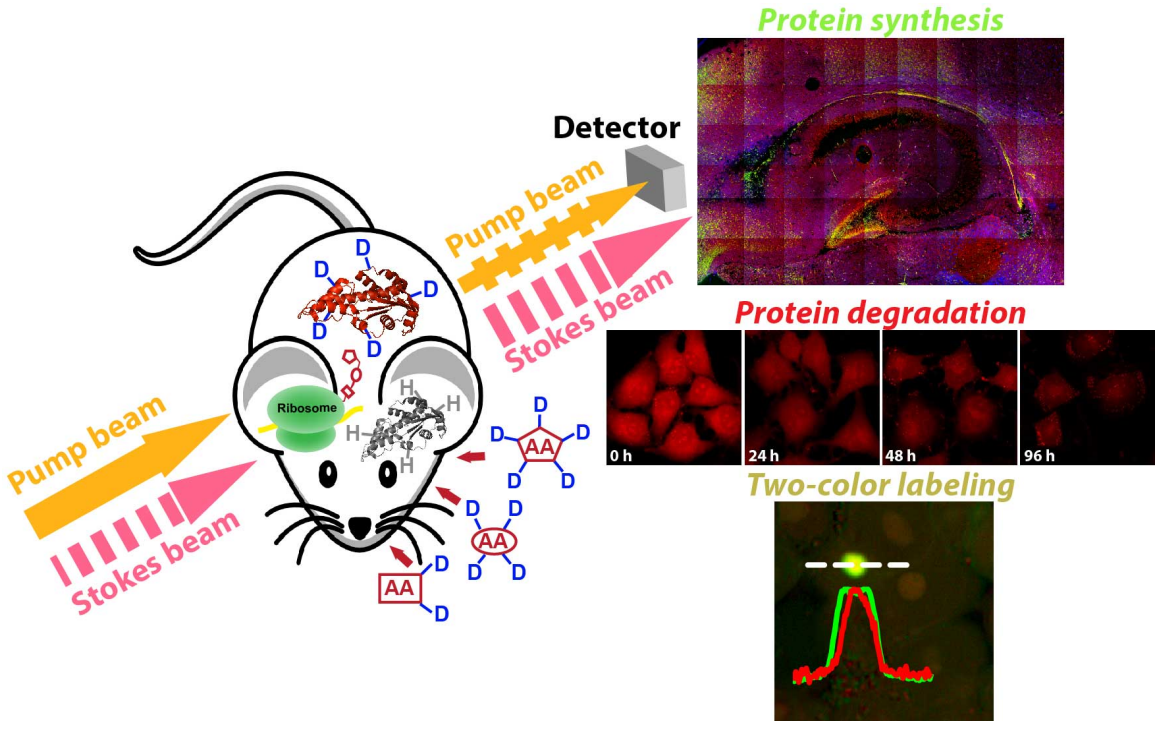

Abstract

Protein metabolism consisting of both synthesis and degradation is highly complex, playing an indispensable regulatory role throughout physiological and pathological processes. To study protein metabolism, extensive efforts, such as autoradiography, mass spectrometry and fluorescence microscopy, have been devoted over the past decades. However, noninvasive and global visualization of protein metabolism has been proven to be highly challenging especially in live systems. Herein, we present a comprehensive imaging platform by coupling stimulated Raman scattering (SRS) microscopy with metabolic labeling of deuterated amino acids (D-AAs) for the visualization of complex protein metabolism including synthesis, degradation and pulse-chase analysis of two temporally defined populations in live bio-systems. First, we pinpointed where and when the new proteins are being synthesized, the key step in the central dogma of molecular biology, in live cells, neurons, brain tissues and all the way to zebrafish and mice *in vivo*. Second, by tracking the methyl group (CH_3) distribution attributed to pre-existing proteins, this platform also enables us to map protein degradation inside live cells. Third, using two sub-sets of structurally and spectroscopically distinct D-AAs, we achieved two-color pulse-chase imaging, as demonstrated by observing aggregate formation of mutant hungtingtin proteins. Hence, the presented labeling and imaging platform would be a valuable tool to study complex protein metabolism with high sensitivity, resolution and biocompatibility for a broad spectrum of systems ranging from cells to model animals, and possibly to humans.

4.1 Introduction.

Proteins are dynamic entities in cells, acting coordinately through both synthesis and degradation to maintain cellular functions. Hence, the ability to image protein metabolism at a global level with subcellular resolution is extremely useful in revealing the metabolic status of a cell. Such a technique would enable functional identification of either sub-cellular compartments or cell locations within complex tissues during physiological and pathological processes. For example, long-term memory formation involves activity-dependent local protein synthesis in neurons[1,2], whereas Huntington's disease often disrupts protein degradation pathways of the affected cell[3,4]. To some extent, it is not the identities of the proteins that are important, but their complex spatial distribution and temporal dynamics.

Current methods including isotope based analysis and bioorthogonal chemistry based fluorescence detection have been extensively applied to visualize complex metabolic dynamics at the proteome level. Traditional autoradiography using radioactive amino acids provide vigorous analysis for either protein synthesis or degradation[5,6]. However, samples must be fixed before exposure to films. Stable Isotope Labeling by Amino Acids in Cell Culture (SILAC) combined with mass spectrometry offers a quantitative approach for proteomics[7,8]. However, it lacks spatial information. Recently developed multi-isotope imaging mass spectrometry (MIMS) provides the imaging ability but is highly invasive, thereby not compatible with live systems[9,10]. A powerful fluorescence based technique named BioOrthogonal Noncanonical Amino acid Tagging (BONCAT) was developed by metabolic incorporation of unnatural amino acids

containing reactive groups, which are subsequently conjugated to fluorescent tags via click chemistry[11-13]. A related labeling strategy was demonstrated with an alkyne analog of puromycin[14]. Unfortunately, these methods generally require non-physiological fixation of cells[15-17].

This chapter reports a comprehensive labeling and imaging platform to probe complex protein metabolic dynamics by exploiting the coupling SRS with metabolic labeling of D-AAs by cell's native translational machineries (Fig. 1). First, we image *de novo* protein synthesis at the global level through the specific detection of the vibrational signature from carbon-deuterium bonds (C-D) by SRS in the cell silent spectral region in live systems from cellular level to complex tissues and model animals *in vivo*. Second, we successfully imaged protein degradation in live HeLa cells by targeting Raman peak of methyl group (CH_3) for the pre-existing protein pools and employing a recently developed linear combination algorithm on measured SRS images at 2940 cm^{-1} and 2845 cm^{-1} channels. Third, inspired by the classic pulse-chase analysis of complex protein dynamics, two-color pulse-chase imaging was accomplished by rationally dividing D-AAs into two structurally different sub-sets that exhibit resolvable vibrational modes, as demonstrated by tracking aggregate formation of mutant huntingtin (mHtt) proteins.

The concept of such an imaging platform is particularly attractive for imaging. On the labeling side, cells and animals can tolerate a large amount of deuterium on D-AAs, which introduces minimum perturbation to protein functions. In fact, experiments using deuterated water or deuterated drugs have already been carried out on humans[18-20]. On the

imaging side, SRS microscopy is a sensitive and specific optical technique for imaging chemical bonds. When the energy difference between incident photons from two lasers (Pump beam and Stokes beam at 867.2 nm and 1064 nm, respectively) matches with the 2133 cm^{-1} mode of C-D vibrations, the joint action of Pump and Stokes photons will efficiently excite vibrational transition of C-D bonds. Whenever a molecule is transferred into the vibrational excited state, the Stokes pulse gains a photon whereas the Pump pulse loses one, dictated by energy conservation (Fig 1a). By detecting the resulting stimulated Raman loss (or gain) of the Pump beam (or the Stokes beam) in one pixel and then raster scan the laser spot across the sample, one can produce a 3D concentration map of the targeted C-D bonds in living cell and tissues (Fig. 1b). Technically, SRS microscopy provides background-free chemical contrast with linear concentration dependence, sub-cellular resolution determined by optical diffraction limit (xy resolution of ~300nm, z resolution or depth of field of ~1000 nm), intrinsic 3D sectioning that is suitable for tissue imaging, and the use of near-infrared wavelength and pico-second excitation pulses minimizes photon scattering inside turbid samples and potential photo-toxicity[21-24].

Taken together, these technical advances and biological applications demonstrate SRS microscopy coupled with metabolic labeling of D-AAs as a comprehensive and generally applicable imaging platform to evaluate complex protein metabolism with high sensitivity, resolution and biocompatibility in a broad spectrum of live cells, tissues and animals.

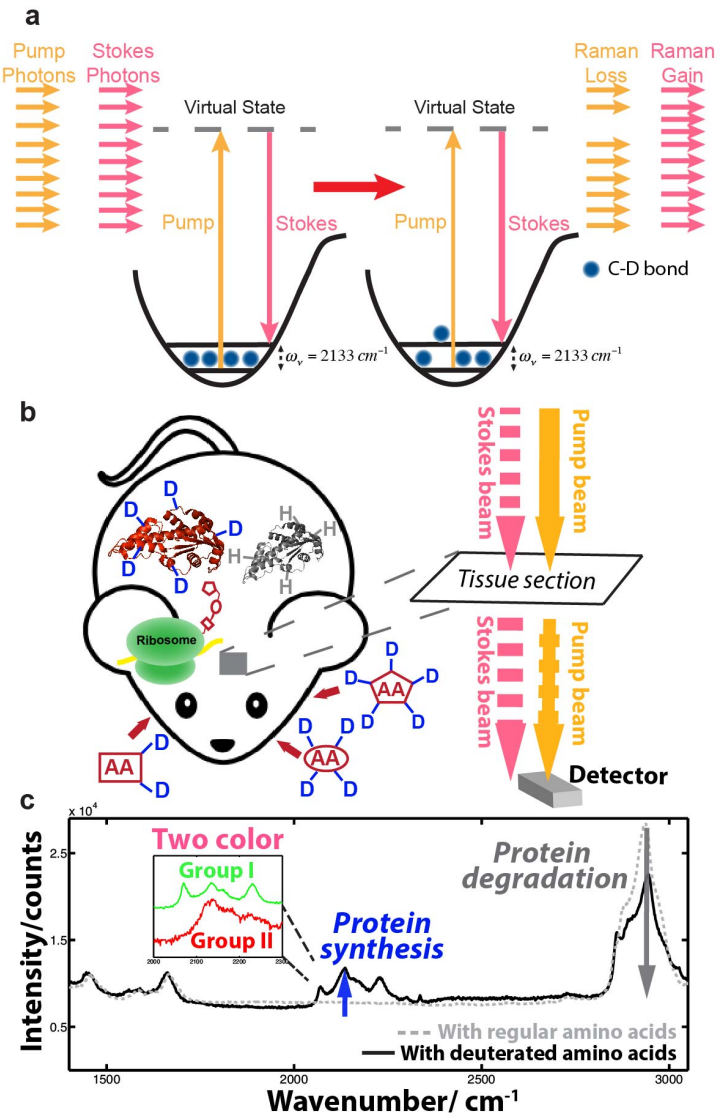

Fig. 4.1 Imaging complex protein metabolism by stimulated Raman scattering (SRS) microscopy in live cells, tissues and animals. (a) Energy diagram of the SRS process. (b) Cartoon for SRS imaging following metabolic labeling of deuterated amino acids (D-AAs) in live organisms (e.g. mice), which are first administered with D-AAs for certain period of time and then imaged by SRS to probe protein metabolism. (c) Spontaneous Raman spectra from HeLa cells incubated with medium containing either regular amino acids (gray, dashed) or D-AAs (black, solid) illustrate three distinct ways to probe complex protein metabolism: imaging newly synthesized proteins by targeting 2133 cm^{-1} from carbon-deuterium bonds (C-D), imaging degradation of pre-existing proteins by targeting the pure methyl group (CH_3) distribution, and two-color pulse-chase protein imaging by labeling with two sub-groups of D-AAs (i.e., group I and group II).

4.2 Selective visualization of newly synthesized proteins.

4.2.1 Introduction.

The proteome of a cell is highly dynamic in nature and tightly regulated by both protein synthesis and degradation processes to actively maintain homeostasis. Many intricate biological processes, such as cell growth, differentiation, diseases and response to environment stimuli, require protein synthesis and translational control[25]. In particular, long-lasting forms of synaptic plasticity, such as those underlying long-term memory, require new RNA and protein synthesis in a space- and time- dependent manner[26-28]. Therefore, direct visualization and quantification of newly synthesized proteins at a global level are indispensable to unraveling the spatial-temporal characteristics of the proteomes in live cells.

First, we demonstrated the proof-of-concept of our new technique on live HeLa cells using a single deuterium-labeled essential amino acid, leucine-d_{10}. Then we optimized the incorporation efficiency of the deuterium isotope into nascent proteins and showed broad applicability of the method on several mammalian cell lines, particularly, its unique advantage in generating spatial maps of the quantitative ratio between new and old proteomes. In addition, besides visualizing newly synthesized proteins in cell bodies, the ability to image nascent proteins in neurites of neuron-like mouse neuroblastoma Neuro-2A (N2A) cells upon differentiation was also shown. Moreover, we further optimized both the SRS instrumentation sensitivity and the labeling recipe enabling imaging with superb spatial and temporal resolution in cultured hippocampal neurons, demonstrating the prospect of studying *de novo* protein synthesis during neuronal plasticity, such as

long-term memory. Finally, going beyond cultured cells, we imaged nascent proteins in brain tissues and zebrafish and mouse *in vivo*. To our knowledge, this is the first report using nonlinear vibrational microscopy for visualizing *de novo* protein synthesis in live systems.

4.2.2 Rationale of isotope-based SRS imaging.

Here we detect the vibrational signal of C-D as an indicator for newly synthesized proteins that metabolically incorporate deuterium-labeled amino acids (Fig. 4.1b-c). When hydrogen atoms are replaced by deuterium, the chemical and biological activities of biomolecules remain largely unmodified. Intriguingly, the C-D stretching motion displays a distinct vibrational frequency from all the other vibrations of biological molecules inside live cells. It is shown in chapter 1 that the frequency of vibrational oscillation, ω_v, inversely scales with the square root of the reduced mass of the oscillator (Eq. 1.10). The reduced mass of the C-D oscillator is increased by two folds when hydrogen is replaced by deuterium. Thus the vibrational frequency ω_v would be reduced by a factor of $\sqrt{2}$. Indeed, the experimentally measured stretching frequency is shifted from ~2950 cm^{-1} of C-H to ~2100 cm^{-1} of C-D. Remarkably, the vibrational frequency of 2100 cm^{-1} is located in a cell-silent spectral window in which no other Raman peaks exist (Fig. 4.1c), thus enabling detection of exogenous C-D with both high specificity and sensitivity.

4.2.3 SRS imaging of newly synthesized proteins by metabolic incorporation of leucine-d_{10} in live HeLa cells.

Among the 20 natural amino acids, leucine is an essential one with both high abundance in protein (~ 9% in mammalian cells) and ten side-chain C-H that can be replaced by C-D[29]. Hence, we first demonstrated the feasibility of our technique by detecting the metabolic incorporation of leucine-d_{10} (L-Leucine-2,3,3,4,5,5,5,5',5',5'-d_{10} as shown in Fig. 4.2a) to nascent proteins in live HeLa cells. Figure 4.2b shows the spontaneous Raman spectrum of HeLa cells incubated in the medium containing 0.8 mM free leucine-d_{10} for 20 hours (blue) over-plotted with the spectrum of HeLa cells growing in the regular medium without leucine-d_{10} (red) as well as the spectrum from a 10 mM free leucine-d_{10} solution in phosphate buffered saline (PBS) (black). As indicated by the comparison between the blue and the red spectra, the Raman peaks of leucine-d_{10}, exhibiting multiple peaks around 2100 cm^{-1} due to symmetric and asymmetrical C-D stretching, are indeed located in the cell-silent region. The comparison of the blue and the black spectra implies that leucine-d_{10} incorporated into cellular proteome after 20 hours is enriched to about 10 mM. Thus a 10% incorporation yield of leucine-d_{10} can be estimated at this condition based on the intrinsic leucine concentration of about 100 mM in proteins (calculated from protein concentration and leucine percentage in cells).

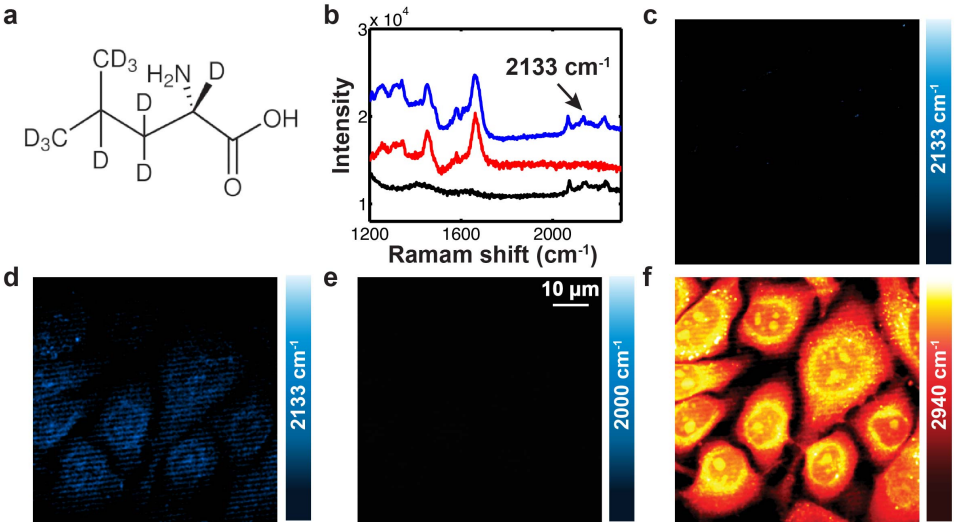

Fig. 4.2 SRS imaging of newly synthesized proteins by metabolic incorporation of leucine-d_{10} in live HeLa cells. (a) Structure of leucine-d_{10} with 10 non-exchangable side-chain deuterium. (b) Spontaneous Raman spectra of HeLa cells incubated with medium containing leucine-d_{10} (0.8 mM) for 20 hrs (blue), HeLa cells growing in regular medium (red), and 10 mM leucine-d_{10} in phosphate buffered saline (PBS) solution (black). The C-D Raman peaks lie in the cell-silent region where no Raman peaks from other biological molecules exist. (c) SRS image targeting the central 2133 cm^{-1} vibrational peak of C-D shows no signal from live HeLa cells growing in regular medium. (d) SRS image targeting the 2133 cm^{-1} vibrational peak of C-D bonds exhibits weak but detectable contrast for live HeLa cells growing in a medium containing leucine-d_{10} (0.8 mM) for 20 hrs. (e) SRS image of the same cells as in (d) is background-free when taken at an off-resonance frequency 2000 cm^{-1}. (f) SRS image of the same cells as in (d) at frequency 2940 cm^{-1} (CH_3 stretching attributed mainly to proteins) shows a much stronger signal from the total protein pool than the 2133 cm^{-1} signal in (d), but with similar protein distribution pattern.

Based on the above spectra, we choose to target the central 2133 cm^{-1} vibrational peak of C-D to acquire SRS images of nascent proteins in live HeLa cells. As expected, HeLa cells growing in regular medium show no detectable SRS contrast at 2133 cm^{-1} (Fig. 4.2c), which is consistent with the flat spectral baseline (red in Fig. 4.2b) in the cell-silent region. In contrast, SRS image of HeLa cells growing in the medium containing 0.8 mM leucine-d_{10} (Fig. 4.2d) shows a weak but clearly identifiable contrast outlining the cell

shape. As a control, the off-resonant SRS image at 2000 cm^{-1} of the same cells is background free (Fig. 4.2e). Such clean chemical contrast among Fig. 4.2 c-e would be difficult for CARS microscopy due to the presence of its non-resonant background. As a protein reference, an image taken at 2940 cm^{-1} (CH_3 stretching mainly from proteins with minor cross-talk from lipids[30]) shows both existing and newly synthesized proteins (Fig. 4.2f), the signal of which comes from the same regions but is much stronger than that in Fig. 4.2d. Thus we have demonstrated the feasibility of using SRS imaging to detect newly synthesized proteins by specifically targeting the C-D vibrational signal of metabolically incorporated leucine-d_{10} in live HeLa cells. This opens up a new imaging opportunity to capture nascent proteome dynamics in live cells under a myriad of cues.

4.2.4 Imaging optimization by metabolic incorporation of deuterium-labeled all amino acids in live HeLa cells with SRS imaging.

Although leucine is the most abundant essential amino acid, it only accounts for a small fraction of amino acids in proteins. Hence, we reasoned that, deuterium-labeling of all the amino acids would lead to a substantial signal enhancement. Indeed, the spontaneous Raman spectrum (Fig. 4.3a) of HeLa cells incubated with deuterium-labeled all 20 amino acids (prepared by supplying uniformly deuterium-labeled whole set of amino acids to leucine, lysine and arginine deficient DMEM medium, more details refer to section 4.6) exhibits an about five times higher C-D vibrational peak than that in Fig. 2b under the same condition. The corresponding SRS image at 2133 cm^{-1} (Fig. 4.3b) shows a significantly more pronounced signal than that in Fig. 4.2d under the same intensity scale. In particular, nucleoli (indicated by arrows in Fig. 4.3b and verified by

DIC visualization) exhibit the highest signal, which is in accordance with previous reports using BONCAT and our own fluorescence staining results (Fig. 4.4). Nucleoli, the active sites for ribosomal biogenesis, have been reported to involve rapid nucleolar assembly and proteomic exchange[31-33]. Such fast protein turnover is indeed reflected by the spatial enrichment of newly synthesized protein signals in those subcellular areas (Fig. 4.3b). Note that SRS imaging here is directly performed on live cells and hence free from potential complications due to fixation and dye conjugation. Again, the off-resonant image at 2000 cm^{-1} is clean and dark (Fig. 4.3c), proving the specificity of SRS imaging of C-D at 2133 cm^{-1}. In addition to image newly synthesized proteins, SRS can readily image intrinsic biomolecules in a label-free manner. By simply adjusting the energy difference between the Pump and the Stokes beams to match the vibrational frequency of amide I, lipids, and total proteins respectively, Fig. 4.3d-f shows the SRS images of amide I band at 1655 cm^{-1} primarily attributed to proteins; CH_2 stretching at 2845 cm^{-1} predominantly for lipids and CH_3 stretching at 2940 cm^{-1} mainly from proteins with minor contribution from lipids.

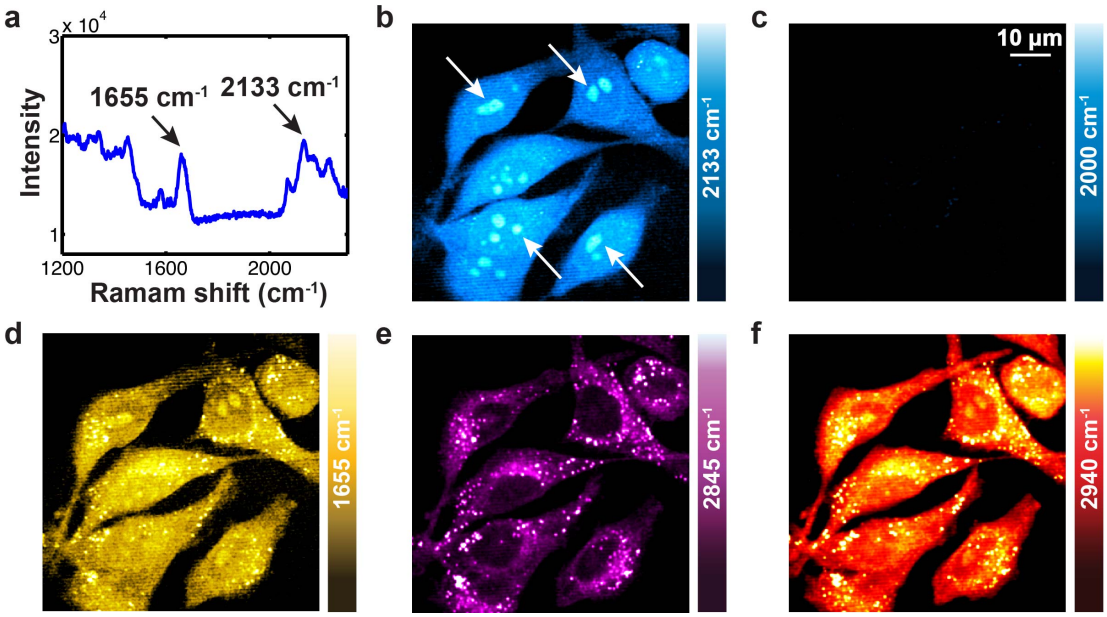

Fig. 4.3 SRS imaging of newly synthesized proteins by metabolic incorporation of deuterium-labeled all amino acids in live HeLa cells. (a) Spontaneous Raman spectrum of HeLa cells incubated with a medium containing deuterium-labeled all amino acids for 20 hrs, showing a ~5 times stronger peak at 2133 cm^{-1} than the blue spectrum in Fig. 2(b). (b) SRS image targeting the central 2133 cm^{-1} vibrational peak of C-D shows a high-contrast image representing newly synthesized proteins. The same intensity scale bar is used here as in Fig. 2(d). Consistent with previous reports, nascent proteins are distributed with a higher percentage in nucleoli (indicated by arrows) which are the active sites for ribosome biogenesis involving constant import and degradation of proteins. (c) SRS image of the same cells as in (b) at off-resonance frequency 2000 cm^{-1} is background-free. (d-f) SRS images of same cells as in (b) at frequency 1655 cm^{-1} (amide I stretching attributed primarily to proteins); 2845 cm^{-1} (CH_2 stretching attributed mainly to lipids) and 2940 cm^{-1} (CH_3 stretching attributed mainly to proteins) show the intrinsic distributions of total cellular lipids and proteins.

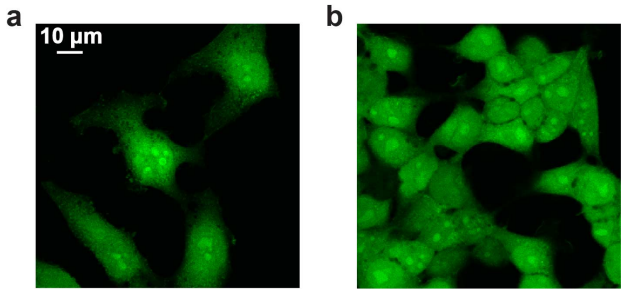

Fig. 4.4 Fluorescence image of newly synthesized proteins in HeLa and HEK 293T cells using bioorthogonal noncanonical amino acid tagging (BONCAT). By metabolic incorporation of homopropargylglycine (Hpg) followed with fluorescence staining after fixation, permeabilization, and click chemistry using Click-iT Hpg Alexa Fluor 488 Imaging Kit, the newly synthesized proteins are shown in green. The fluorescence images of HeLa cells (a) and HEK293T cells (b) show the maps of newly synthesized proteins in the whole-cell level with nucleoli being highlighted.

4.2.5 Time-dependent *de novo* protein synthesis.

Being linearly dependent on analyte concentration, SRS contrast is well-suited for quantification of *de novo* protein synthesis in live cells. Here we show time-dependent protein synthesis images under the same intensity scale (Fig. 4.5a-c). As expected, the new protein signal (2133 cm^{-1}) from 5-hour, 12-hour and 20-hour incubation increases substantially over time (Fig. 4.5a-c) while the amide I (1655 cm^{-1}) signal remains at a steady state (Fig. 4.5d-f). Since protein distribution is often heterogeneous in biological systems, we presented a more quantitative representation by acquiring ratio images between the newly synthesized proteins and the total proteome (from either amide I or CH_3). Figure 4.5g-i depicts the fraction of newly synthesized proteins (2133 cm^{-1}) among the total proteome (1655 cm^{-1}) and its spatial distribution. The fraction of newly synthesized proteins is growing with time from 5 hours to 20 hours, highlighting nucleoli as the subcellular compartments with fast protein turnover[31-33]. Such quantitative ratio

imaging of new versus old proteomes would be very difficult to obtain using BONCAT or mass spectroscopy without the destruction of cells.

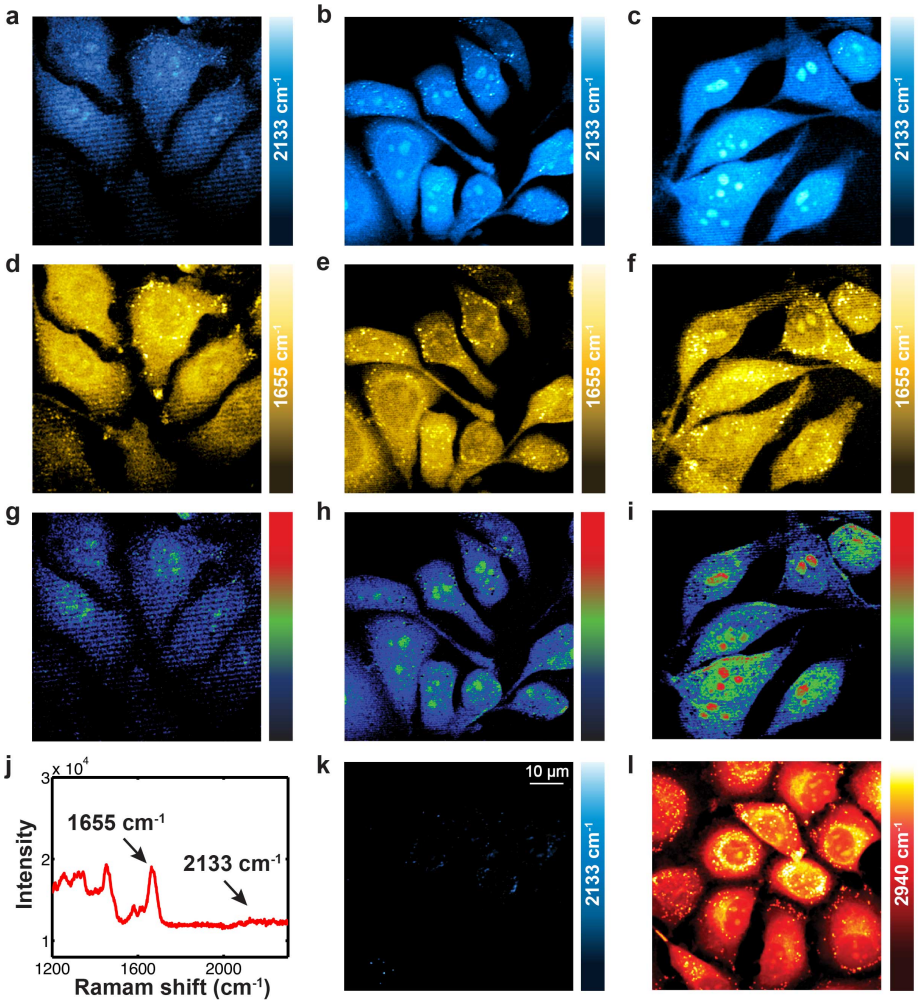

Fig. 4.5 SRS imaging of time-dependent *de novo* protein synthesis and drug-induced protein synthesis inhibition effect in live HeLa cells incubated in deuterium-labeled all amino acid medium. (a-f) SRS image targeting the central 2133 cm^{-1} vibrational peak of C-D displays a time-dependent signal increase (5 hrs (a), 12 hrs (b), 20 hrs (c)) of the newly synthesized proteins, with nucleoli being obviously gradually highlighted. As a control, the amide I (1655 cm^{-1}) signal remains at a steady state over time (5 hrs (d), 12 hrs (e), 20 hrs (f)). (g-i) Ratio images between the SRS image at 2133 cm^{-1} (newly synthesized proteins) and the SRS image at 1655 cm^{-1} (the amide I band from total proteins), representing the relative new protein fraction with subcellular resolution at each time point (5 hrs (g), 12 hrs (h), 20 hrs (i)). The color bar ranging from black to red represents the ratio ranging from low to high. (j) Spontaneous Raman spectrum of HeLa cells incubated with both deuterium-labeled all amino acids and a protein synthesis inhibitor

anisomycin (5 μM) for 12 hrs shows the absence of the C-D Raman peak at 2133 cm^{-1}. (k) SRS image of the same sample displays non-detectable signal throughout the whole field of view. (l) As a control, the image of the same cells at 2940 cm^{-1} confirms that anisomycin does not influence the total protein level.

The effect of protein synthesis inhibition by chemical drugs is further tested to validate that the detected C-D signal indeed derives from nascent proteins. HeLa cells incubated with deuterium-labeled all amino acids together with 5 μM anisomycin, which works as a protein synthesis inhibitor by inhibiting peptidyl transferase or the 80S ribosome system, for 12 hours show the complete absence of the C-D signal in the spontaneous Raman spectrum (Fig. 4.5j). Furthermore, SRS imaging of the same samples exhibits no detectable signal (Fig. 4.5k) when compared to Fig. 4.5b without the protein synthesis inhibitor. As a control, the corresponding 2940 cm^{-1} image (Fig 4.5l) of total proteome remains at a similar level as the non-drug treated counterpart in Fig. 4.3f. Thus, the detected C-D SRS signal (Fig. 4.5 a-c) unambiguously originates from deuterium-labeled nascent proteins, which vanishes upon adding the protein synthesis inhibitor.

4.2.6 Demonstration on HEK293T and neuron-like differentiable N2A cells.

To show the general applicability and potential of our method, we choose two additional mammalian cell lines for further demonstration: human embryonic kidney HEK293T cells, and neuron-like neuroblastoma mouse N2A cells which can be induced to differentiate with the growth of neurites (i.e., axons and dendrites). The spontaneous Raman spectrum (Fig. 4.6a) of HEK293T cells incubated with deuterium-labeled all amino acids for 12 hrs exhibits a 2133 cm^{-1} C-D channel signal nearly as high as the 1655 cm^{-1} amide channel signal. The resulting SRS image shows a bright signal for new

proteins with an intense pattern residing in nucleoli (Fig. 4.6b). As before, the off - resonant image (2000 cm^{-1}) displays vanishing background (Fig. 4.6c); the amide I channel (1655 cm^{-1}) image (Fig. 4.6d) exhibits consistent overall proteome distributions similar to that in HeLa cells; CH_2 channel (2845 cm^{-1}) image (Fig 4.6e) depicts a more diffusive lipid distribution in cytoplasm compared to that in HeLa cells. Consistent with the results obtained in HeLa cells above, the ratio image (Fig. 4.6f) between the newly synthesized proteins (Fig. 4.6b) and the total proteins (Fig. 4.6d) highlights nucleoli for active protein turnover in HEK293T cells as well[31-33].

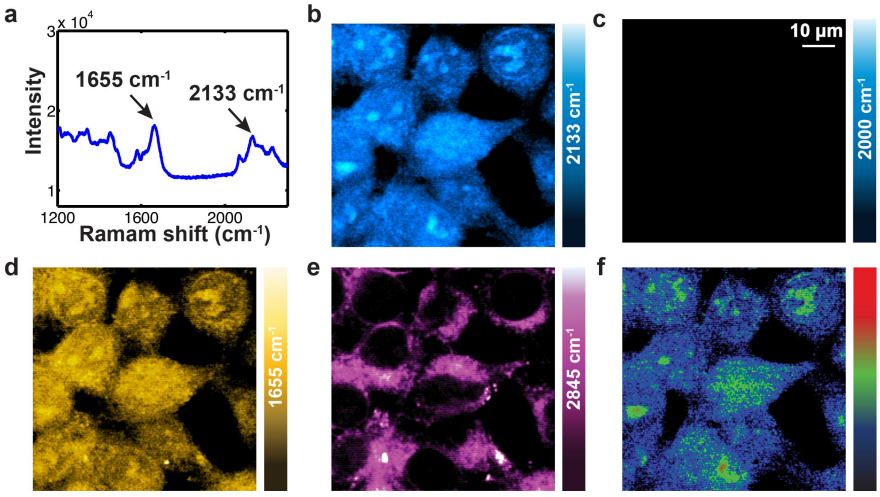

Fig. 4.6 SRS imaging of newly synthesized proteins by metabolic incorporation of deuterium-labeled all amino acids in live human embryonic kidney (HEK293T) cells. (a) The spontaneous Raman spectrum of HEK293T cells incubated with deuterium-labeled all amino acids for 12 hrs shows a 2133 cm^{-1} C-D peak nearly as high as the Amide I (1655 cm^{-1}) peak. (b) SRS image targeting the central 2133 cm^{-1} vibrational peak of C-D bond shows newly synthesized proteins in live HEK293T cells displaying a similar signal level as HeLa cells at 12 hrs (Fig. 4(b)). (c) As a comparison, the off-resonant image is still background-free. (d-e) Multicolor SRS images of intrinsic cell molecules: total proteins (1655 cm^{-1} (d)) and lipids (2845 cm^{-1} (e)). (f) The ratio image between new proteins (2133 cm^{-1}) and total proteins (1655 cm^{-1}) illustrates a spatial map for nascent protein distribution.

Besides showing the ability to image newly synthesized proteins inside cell body, our technique can also be applied to tackle more complex problems, such as *de novo* protein synthesis in neuronal systems[26-28]. As an initial demonstration, we imaged the newly synthesized proteins in neuron-like N2A cells, which have been extensively used as a model system to study neuronal differentiation, axonal growth and signaling pathways. Under differentiation condition, N2A cells massively grow new neurites from cell bodies and form connections with other cells. Fig. 4.7a shows the image of newly synthesized proteins after induction for differentiation, by simultaneously differentiating the N2A cells and supplying with the deuterium labeled all amino acids for 24 hours. Similar to HeLa and HEK293T cells, N2A cell bodies are observed to display high-level protein synthesis. More interestingly, newly synthesized proteins are also observed in a subset of, but not all neurites (Fig. 4.7a and Fig. 4.7b), which implies that the observed neurites in Fig. 4.7a are newly grown under the differentiation condition. For a detailed visualization, Fig. 4.7c, d show the zoomed-in regions in the dashed squares in Fig. 4.7a, b respectively. A more comprehensive examination is illustrated by both the ratio image (Fig. 4.7e) between Fig. 4.7c and Fig 4.7d and the merged image (Fig. 4.7f) with the red channel designating new protein signal from Fig. 4.7c and the green channel designating total protein signal from Fig. 4.7d. On one hand, both the ratio image and the merged image highlight the neurites with higher percentage of new proteins (indicated by stars), implying these neurites are newly grown. On the other hand, from the merged image, there are some neurites (indicated by arrows) showing obvious signals in the green channel (total proteins) only but with no detectable signal in the red channel (new proteins). Hence, the arrow indicated neurites are most likely older than their starred

counterparts. In addition, the transition from green to red in the merged image (Fig. 4.7f) implies the growth direction by which new neurites form and grow.

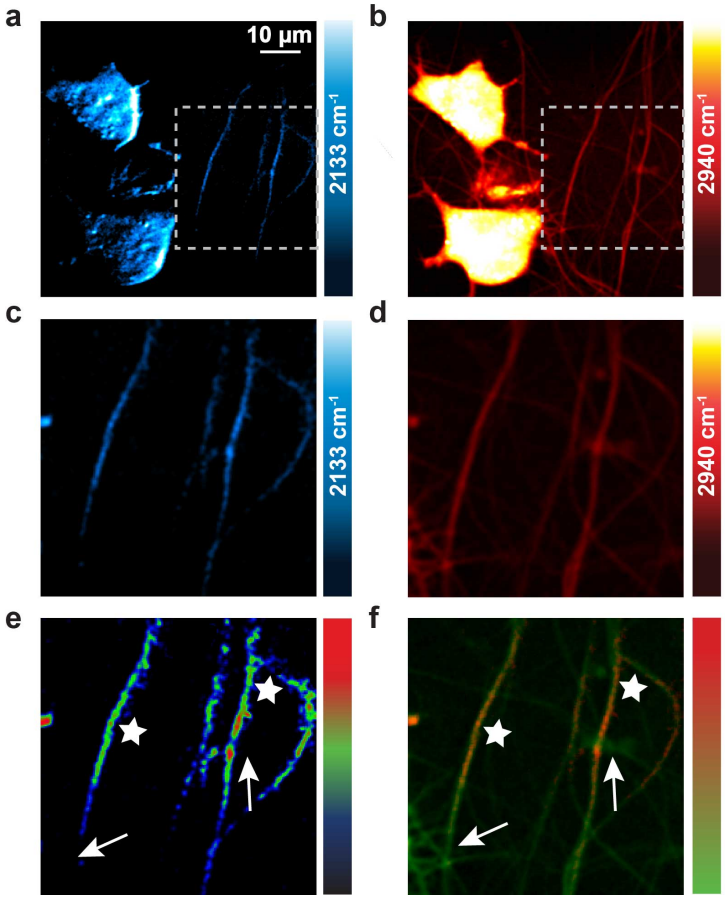

Fig. 4.7 SRS imaging of newly synthesized proteins in both cell bodies and newly grown neurites of neuron-like differentiable mouse neuroblastoma (N2A) cells. During the cell differentiation process by serum-deprivation and 1 μM retinoic acid, deuterium-labeled all amino acids medium is also supplied for 24 hrs. (a) SRS images targeting the central 2133 cm^{-1} vibrational peak of C-D show newly synthesized proteins. (b) SRS images targeting the 2940 cm^{-1} CH_3 show total proteins. (c-d) Zoomed-in images as indicated in the white dashed squares in (a) and (b). (e) Ratio image between new protein (c) and total proteins (d). While the starred neurites show high percentage of new proteins, the arrows indicate neurites displaying very low new protein percentage. (f) Merged image between new protein (c) (red channel) and total proteins (d) (green channel). Similarly, starred regions show obvious new proteins; while arrows indicate regions that have undetectable new protein signal.

4.2.7 Sensitivity optimization and time-lapse imaging of the *de novo* proteome synthesis dynamics.

The cell culture medium used in the previously sections 4.2.4 - 4.2.6 was prepared by supplying uniformly deuterium-labeled whole set of amino acids to a commercially available medium that is deficient of leucine, lysine and arginine. Due to the presence of other regular amino acids already in the commercial medium, the resulting partially deuterated medium has only about 60% deuteration efficiency. Realizing this, in this section we custom prepared new media that replace nearly all the regular amino acids by the D-AA counterparts (details in section 4.6). As shown in the spontaneous Raman spectra (Fig. 4.8a), the optimized medium (red spectrum) displays a 50% signal increase compared with the partially deuterated medium (blue spectrum). Indeed, SRS images targeting C-D vibrational peak at 2133 cm^{-1} confirms a 50% average intensity boost in live HeLa cells (Fig. 4.8b). The use of optimized D-AA medium now leads to an about 8 times higher signal than when using a single leucine-d_{10} (Fig. 4.8a, red vs black spectrum). In addition to improving labeling strategy, non-trivial instrumentation optimizations are also carried out compared to results shown in previous sections. To further improve SRS detection sensitivity and acquisition speed, laser output the and microscope system throughput for near-IR wavelengths have been increased; the acousto-optic modulator (AOM) has been replaced with an electro-optic modulator (EOM) for a 30% higher modulation depth, and a high-speed lock-in amplifier has been employed for faster image acquisition.

With much-improved sensitivity, protein synthesis can now be imaged with superb

spatial and temporal resolution. Spatially, we visualized newly synthezied proteins from fine structures (likely dendritic spines, indicated by arrow heads) of live neurons (Fig. 4.8c). Temporally, we could readily image newly synthesized proteins in live HeLa cells in less than one-hour incubation with the optimized deuteration medium (Fig. 4.8d). Control image with protein synthesis inhibitors only displays vague and homogeneous cell outlines which presumably come from the free D-AA pool (sub-mM concentration, much more dilute than the metabolically enriched pool in the protein-bound form)[34]. Moreover, using a fast lock-in amplifier, our current imaging speed can be as fast as 3 s per frame (512 × 512 pixels), nearly 10 times faster than before, which enables time-lapse imaging in live cells with minimum photo-toxicity to cell viabilities. Figure 4.8e presents time-lapse SRS imaging of a same set of live HeLa cells gradually synthesizing new proteins over time from 10 min to 5 h incubation in optimized D-AA medium. The obvious cell migration and division prove their viability, supporting high bio-compatibility of our technique. To our best knowledge, this is the first time that long-term time-lapse imaging of proteome synthesis *dynamics* has been demonstrated on single live mamamian cells.

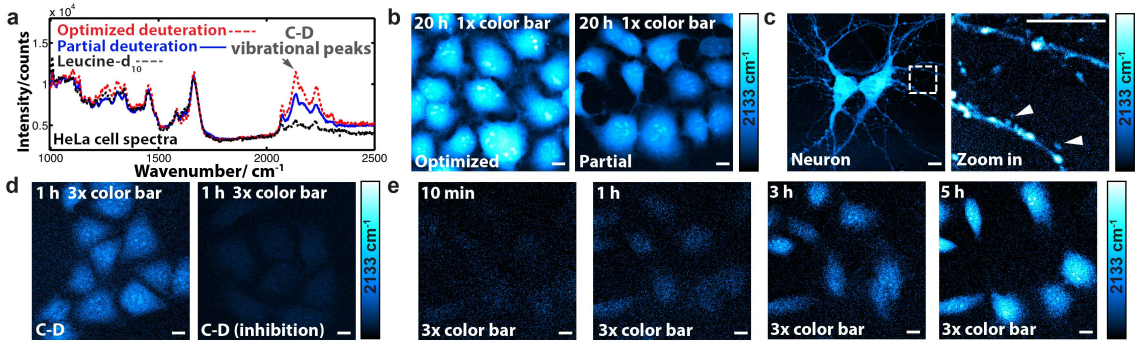

Fig. 4.8 High sensitivity SRS imaging of newly synthesized proteins in live cells after labeling and instrumentation optimization. (a) Spontaneous Raman spectrum of C-D peaks in HeLa cells incubated in optimized deuteration medium (red) displays a 50% increase when compared to the previously reported partial deuteration medium (blue), and about 8 times higher than using leucine-d_{10} (black) only. Each spectrum is averaged over 5–10 cells. (b) SRS images of newly synthesized proteins in live HeLa cells confirm a 50% average signal increase. (c) SRS images of newly synthesized proteins in live neurons in optimized deuteration medium for 20 h. The zoom-in image highlights the fine dendritic structures (likely dendritic spines, arrow-headed). (d) SRS image of newly synthesized proteins in live HeLa cells with 1 h incubation of optimized deuteration medium. Control image with protein synthesis inhibition deprives most of the signal. (e) Time-lapse SRS images of protein synthesis dynamics in a same set of live HeLa cells with continuous incubation in optimized deuteration medium. Scale bar, 10 μm.

4.2.8 SRS imaging of newly synthesized proteins in live mouse brain tissues.

Going above the cellular level, we now apply our imaging platform to a more complex level, organotypical brain tissues. In our study, we focus on the hippocampus because it is the key region in brains that involves extensive protein synthesis[5, 35]. As expected, active protein synthesis is found in the hippocampal region, particularly in the dentate gyrus, which is known for its significant role in both long-term memory formation and adult neurogenesis[35]. SRS image at 2133 cm^{-1} (Fig. 4.9a, C-D) of a live mouse organotypic brain slices cultured in D-AA medium for 30 h, reveals active protein synthesis from both the soma and the neurites of individual neurons in dentate gyrus. In

addition, the old protein (CH_3) and total lipids (CH_2) images are presented silmultaneously for multichannel analysis (Fig. 4.9a).

In order to investigate spatial pattern of protein synthesis on a larger scale, we imaged the entire brain slice by acquiring large-area image mosaics. A 4–by–3 mm image (Fig. 4.9b) of another organotypic slice displays overlayed patterns from new proteins (2133 cm^{-1}, green), old proteins (CH_3, red) and lipids (CH_2, blue). Intriguing spatial variation is observed: while the distribution of old proteins are relatively homogenous across the field of view, newly synthesized proteins are either concentrated in dentate gyrus or scattered within individual neurons throughout the cortex, suggesting high activities in these two regions. Thus, we have demonstrated the ability to directly image protein synthesis dynamics on living brain tissues with subcellular resolution and multi-channel analysis, which was difficult to achieve with other existing methods[36] The intricate relationship between protein synthesis and neuronal plasticity[37] is currently under investigation on this platform.

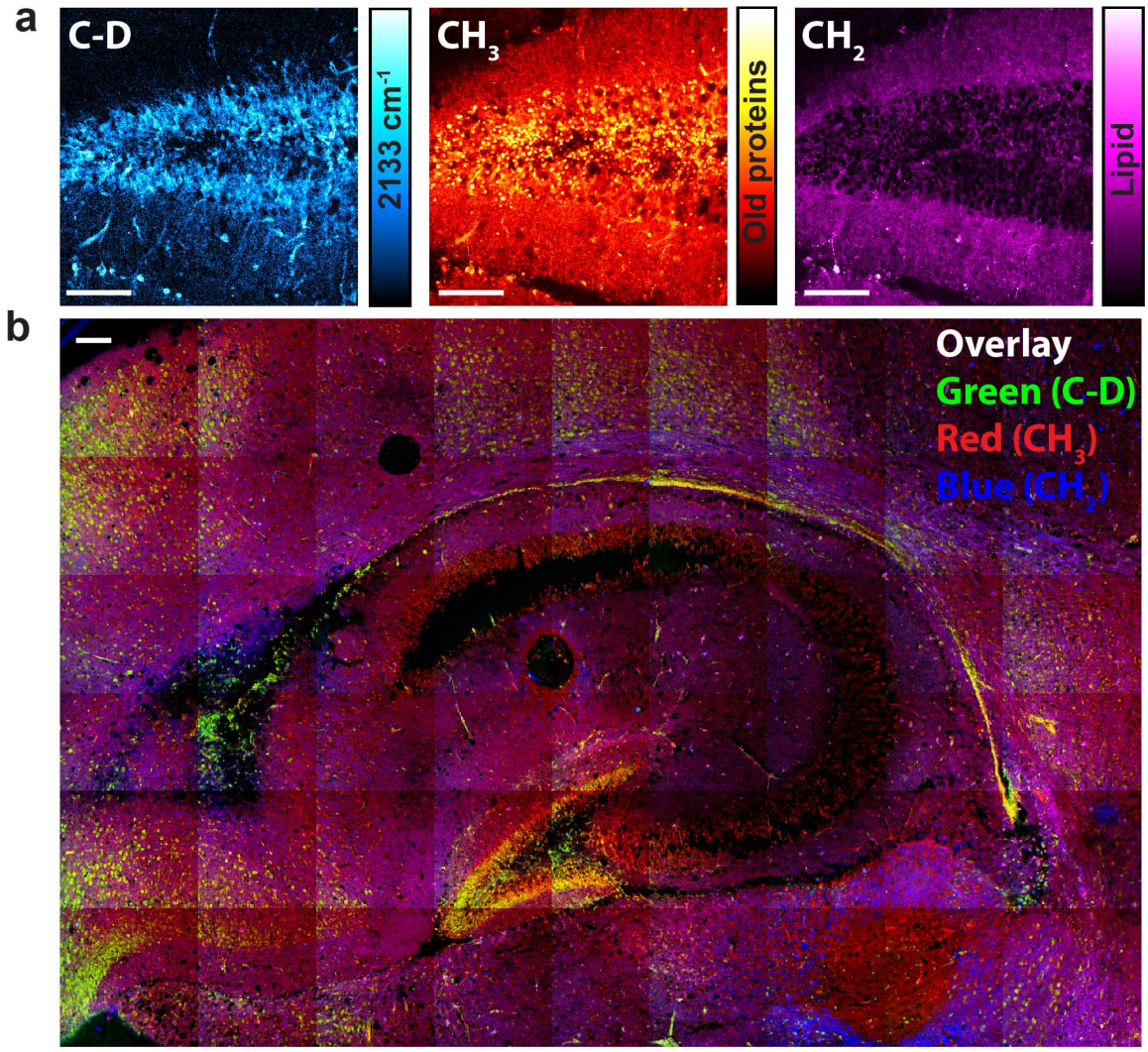

Fig. 4.9 SRS imaging of live mouse brain tissues identifying locations of active protein synthesis. (a) SRS images at dentate gyrus of a live organotypic brain slice (400 μm thick, from a P10 mouse) after culturing in D-AA medium for 30 hr. 2133 cm^{-1} (C-D) image presents the distribution of newly synthesized proteins. The CH_3 and CH_2 images show the old protein pools and total lipids, respectively. (b) A 4–by–3 mm large field view overlay image of new proteins (C-D, green), old proteins (CH_3, red) and total lipids (CH_2, blue) for a brain slice (400 μm thick, from a P12 mouse) cultured in D-AA medium for 30 h. Scale bar, 100 μm.

4.2.9 SRS imaging of newly synthesized proteins *in vivo*.

One prominent advantage of our labeling strategy is its non-toxicity and minimal invasiveness to animals. We thus move up to the physiological level to image protein

metabolism in embryonic zebrafish and mice. Zebrafish are popular model organisms due to their well-understood genetics and transparent embryos, amenable to optical imaging[38]. We injected 1 nL D-AA solution into zebrafish embryos at the 1-cell stage (150 ng D-AAs per embryo), and then allowed them to develop normally for 24 h (Fig. 6a, bright field) before imaging the whole animal. We found a high signal for newly synthesized proteins (Fig. 4.10a, 2133 cm^{-1}) in the somites at the embryonic zebrafish tail, consistent with the earlier BONCAT result[39]. The spatial pattern of this signal appears similar to that of the old protein distribution (Fig. 4.10a, CH_3), but almost complementary to the lipid distribution (Fig. 4.10a, CH_2).

Finally we demonstrate on mammals – mice. We administered the drinking water containing D-AAs to 3-week-old mice for 12 days, and then harvested liver and intestine tissues for subsequent imaging. No toxicity was observed for the fed mice. The SRS images from both live liver tissues (Fig. 4.10b) and live intestine tissues (Fig. 4.10c) illustrate the distributions of newly synthesized proteins (2133 cm^{-1}, C-D) during the feeding period, which resemble the total protein distribution (1655 cm^{-1}, Amide I). On a faster incoporation timescale, live liver and intestine tissues obtained after intraperitoneal injection of D-AAs into mice for 36 h reveal spatial patterns (Fig. 4.11) similar to the feeding results above as well as the click-chemistry based fluorescence staining[14]. All these results support our imaging platform as a highly suitable technique for *in vivo* interrogation.

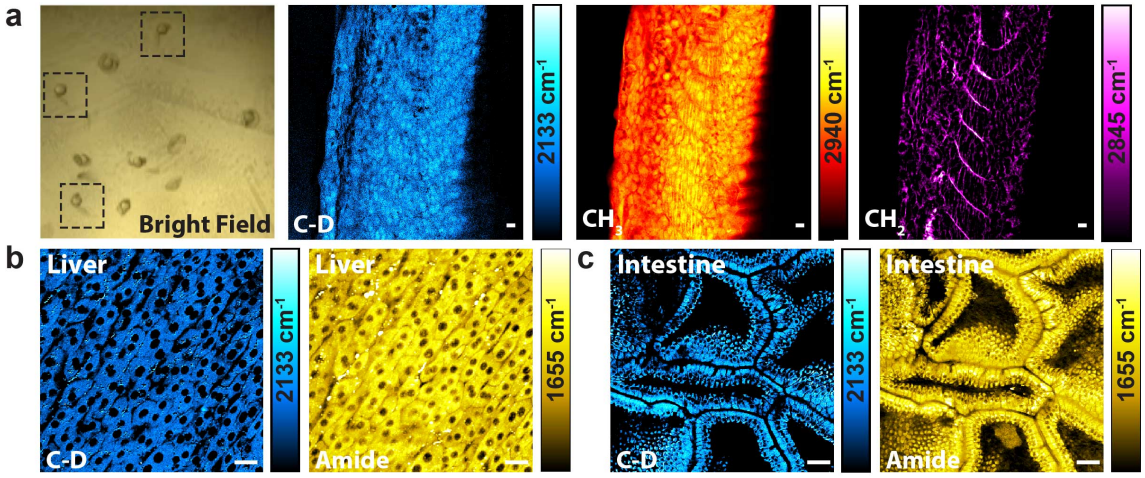

Fig. 4.10 SRS imaging for newly synthesized proteins *in vivo* of both intact zebrafish and mouse. (a) SRS images of a 24-hpf (hpf: hours post fertilization) zebrafish. Wild-type zebrafish embryos were injected at 1-cell stage with 1 nL D-AA solution and allowed to develop normally for another 24 h before imaging. Bright field image shows the gross morphology of embryonic zebrafish at 24 hpf (dashed boxes). 2133 cm^{-1} (C-D) image presents the distribution of newly synthesized proteins (Supplemental Fig. 2a) in the somites of an embryonic zebrafish tail. The CH_3 image shows the old protein pool while the CH_2 image depicts total lipid in the same fish. (b-c) SRS images of live mouse liver (b) and intestine (c) tissues harvested from mice after administered with D-AA containing drinking water for 12 days. 2133 cm^{-1} (C-D) channel shows newly synthesized proteins (Supplemental Fig.2 b-c) that resemble the distribution of total protein as shown in the 1655 cm^{-1} image (Amide I). Scale bar, 10 μm.

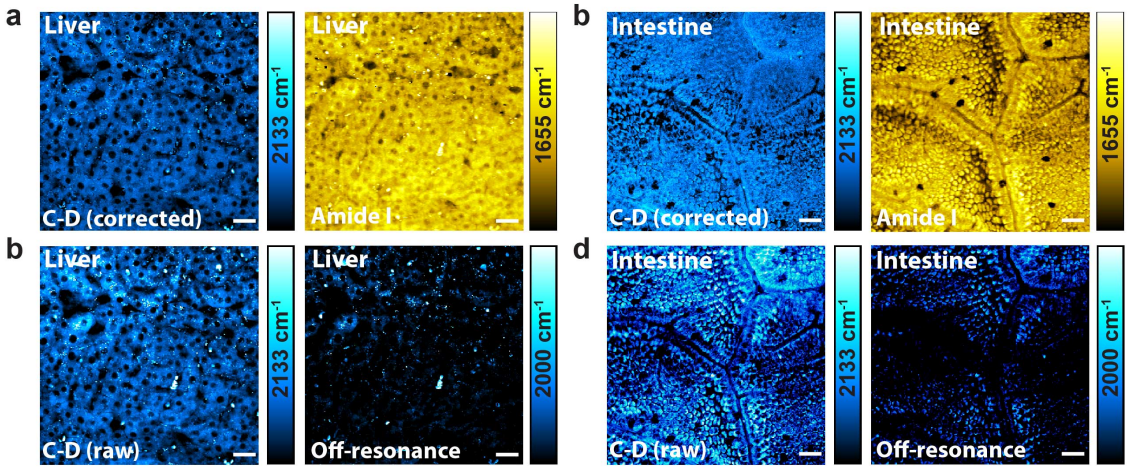

Fig. 4.11 SRS imaging for newly synthesized proteins *in vivo* of mice after intraperitoneal injection (IP injection) of D-AA solutions. (a-b) SRS images of live mouse liver (a) and intestine (b) tissues harvested from mice after intraperitoneal injection with D-AA solutions for 36 h. 2133 cm^{-1} channel shows newly synthesized proteins (off-resonance image subtracted) that resemble the distribution of total proteins as shown in the 1655 cm^{-1} image (Amide I). (c-d) Corresponding raw C-D on-resonance (2133 cm^{-1}) and off-resonance (2000 cm^{-1}) images are shown as references for liver (c) and intestine (d) tissues. Scale bar, 10 μm.

4.3 Probing protein degradation.

Besides imaging protein synthesis, our labeing and imaging platform offers the ability to probe protein degradation simultanously. Exeprimentally, we intend to probe the pre-existing protein pool by targeting the CH_3 showing a strong peak at 2940 cm^{-1}, as newly synthesized proteins will be mostly carrying C-D peaked around 2133 cm^{-1}. However, the 2940 cm^{-1} CH_3 protein channel is known to suffer from undesired crosstalk from the 2845 cm^{-1} CH_2 lipid signal[24]. To obtain a clean protein component, we adopt two-color SRS imaging at both 2940 cm^{-1} and 2845 cm^{-1} channels followed by a linear combination algorithm which has been effectively applied in cells, tissues and animals[40-42]. The subsequently obtained images show the pure distribution of old protein pools (exclusively from CH_3) and the distribution of lipids (exclusively from CH_2),

respectively. Hence protein degradation could be tracked by imaging the old protein distributions over time when cells are growing in the D-AA medium.

Figure 4.12a shows time-dependent SRS images of old protein distributions (CH_3) in live HeLa cells when incubated with D-AAs from 0 h to 96 h. Clearly, the old protein pool is degrading, as shown by the decay of its average intensity. As a contrast, the total lipid images display no obvious intensity change (Fig. 4.12b). In addition, the spatial patterns of old proteins (Fig. 4.12a) reveal a faster decay in the nucleoli than the cytoplasm. This observation is consistent with the fact that neucleoli have active protein turnover[32] and also with our report in previous sections that C-D labeled newly synthesized proteins are more prominent in nucleoli. Single exponential decay fitting of the average intensities in Fig. 3a yields a decay time constant of 45 ± 4 h (Fig. 4.12c), corresponding to a proteome half-live of 31 ± 3 h which is very close to the data reported by mass spectrometry (35 h)[43]. Therefore, our imaging platform is capable of observing both protein synthesis and degradation by imaging at C-D channel and CH_3 channel, respectively, thus capturing proteomic metabolism dynamics in full-scope.

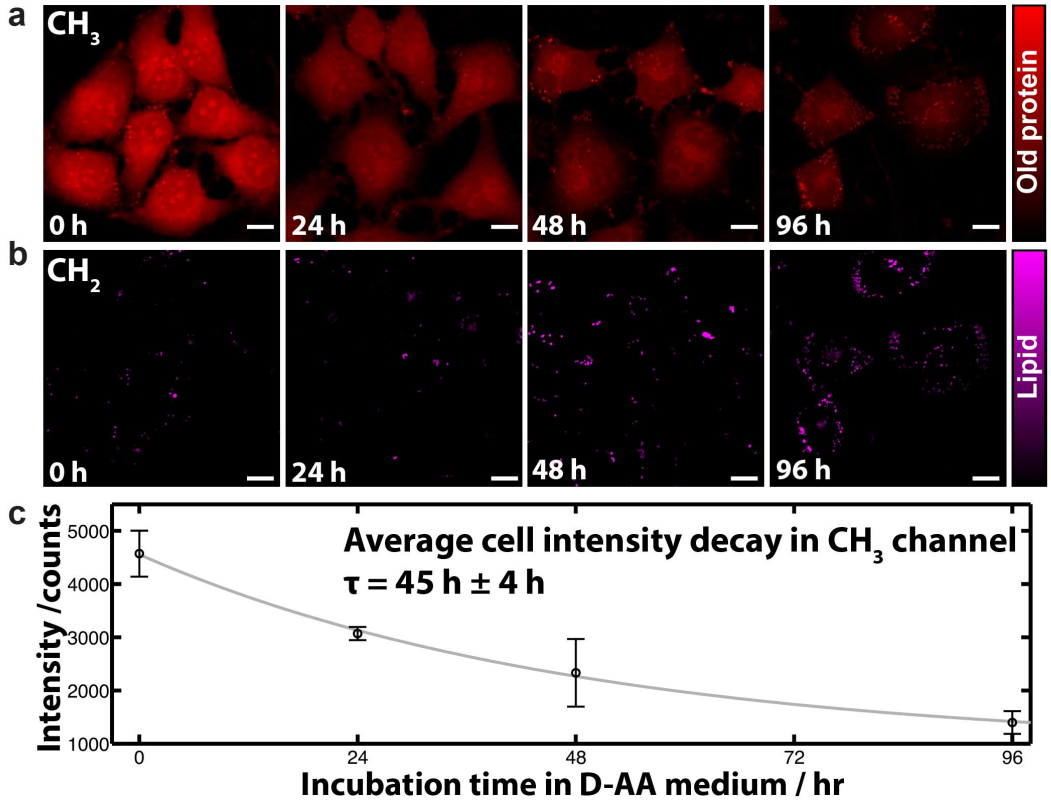

Fig. 4.12 Time-dependent SRS imaging of protein degradation in live HeLa cells. (a) Adopting a linear combination algorithm between 2940 cm^{-1} and 2845 cm^{-1} channels, the obtained SRS images exclusively from CH_3 vibration display gradual degradation of pre-existing proteins in live HeLa cells cultured in optimized deuteration medium for 0 h, 24 h, 48 h and 96 h. (b) SRS images exclusively from CH_2 vibration display the total lipid distribution at the corresponding time point. (c) Single exponential decay fitting from averaged cellular image intensities of pre-existing proteins in (a), yielding a protein degradation time constant of 45 ± 4 h. Error bars, standard deviation. Scale bar, 10 μm.

4.4 Two-color pulse-chase SRS imaging of temporally defined proteins.

Inspried by the popular pulse-chase analysis in classic autoradiography techniques and recent two-color BONCAT imaging[44], we aim to exploit another dimension of probing dynamic protein metabolism with two-color pulse-chase imaging of proteins labeled at different times. To do so, we need to rationally divide total D-AAs into two sub-sets with distinct Raman spectra. We reasoned that Raman peaks of C-D stretching

are closely related to their chemical environments, thus the structural difference between D-AAs should lead to diverse Raman peak positions and shapes. We then examined the spontanesous Raman spectra of each D-AA sequentially, and subsequently identified two subgroups. Group I contains three amino acids, leuine-d_{10}, isoleucine-d_{10} and valine-d_8, structurally known as branched-chain amino acids (Fig. 4.13a). All members of group I exhibits multiple distinct Raman peaks with the first one around 2067 cm^{-1}. The rest of D-AAs without branched chains are then categorized into group II, all of which show a prominent Raman peak around 2133 cm^{-1} (three examples shown in Fig. 4.13b). To test inside cells, Raman spectra of HeLa cells cultured in either group I D-AA medium only (green) or group II D-AA medium only (red) are shown in Fig. 4.13c. Based on the spectra, we choose to acquire two-color narrow-band SRS images at 2067 cm^{-1} and at 2133 cm^{-1}. By constructing and utilizing a linear combination algorithm (refer to section 4.6), similar to the one used for CH_3 and CH_2 above, pure signals of proteins labeled by group I D-AAs and by group II D-AAs can be succesfully separated and quantitatively visualized. Note that hyper-spectral imaging approaches using broadband femtosecond lasers might also work here[45-47].

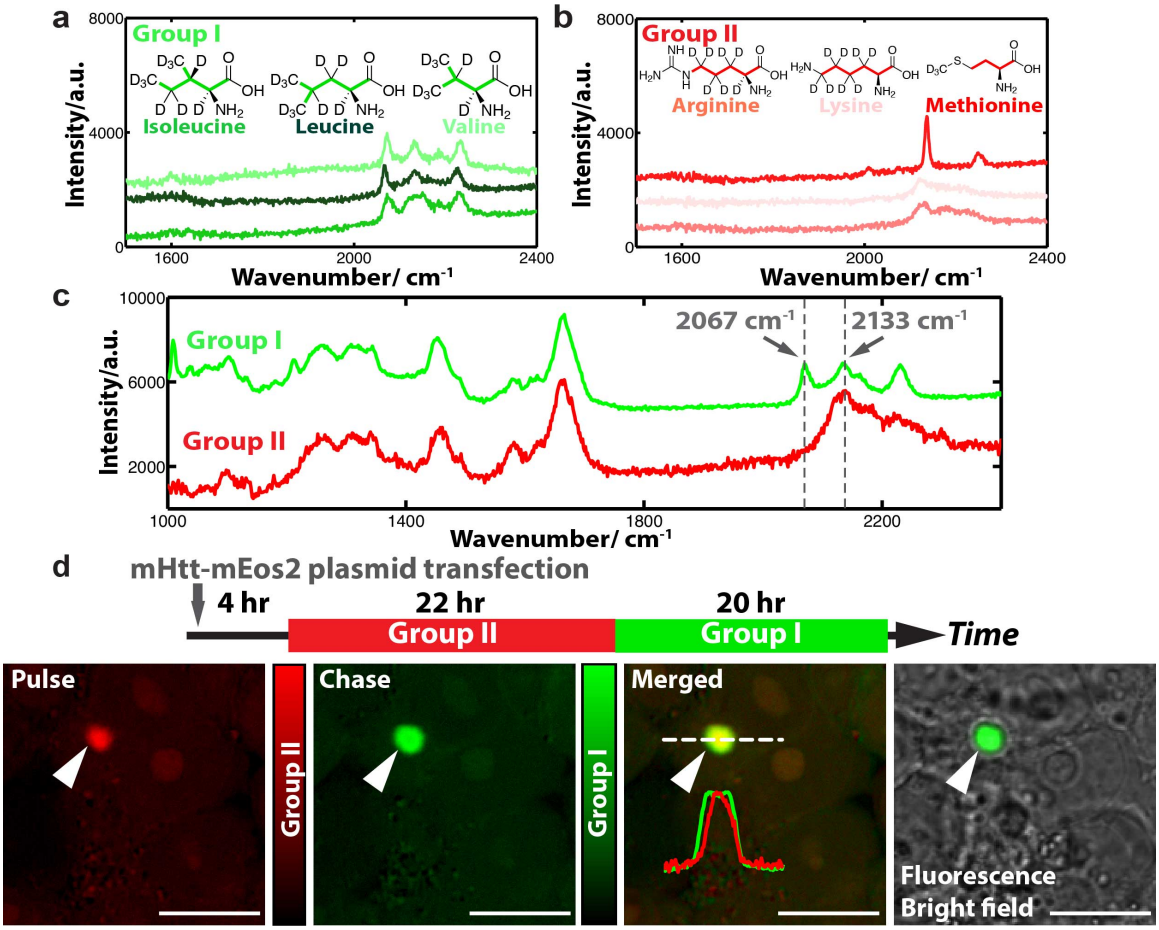

Fig. 4.13 Two-color pulse-chase SRS imaging of distinct sets of temporally defined proteins. (a) Structures and spontaneous Raman spectra of group I D-AAs (i.e. the branched chain amino acids). (b) Structures and spontaneous Raman spectra of three examples of group II non-branched D-AAs. (c) Spontaneous Raman spectra of HeLa cells cultured with group I D-AAs (green), showing multiple peaks with the first around 2067 cm^{-1}, and with group II D-AAs (red), showing a common peak around 2133 cm^{-1}. (d) Two-color pulse-chase imaging by sequential labeling of group II and group I D-AAs in time with simultaneous expression of mutant huntingtin (mHtt94Q-mEos2) proteins. Cartoon displays experimental timeline of plasmid transfection and D-AA medium exchanges. The fluorescence image (overlaied with bright field) indicates the formation of a large aggregate (arrow-headed) of mHtt94Q-mEos2. The retrieved signals from linear combination of the original images at 2067 cm^{-1} and 2133 cm^{-1} channels display a large aggregation of mHtt proteins solely labeled by group II D-AAs during the first 22 h (red, pulse) and mHtt proteins only labeled by group I D-AAs during the following 20 h (green, chase). The merged image, as well as the intensity profile, from the pulsed (red) and chased (green) images confirms with a yellow core and a green shell. Scale bar, 10 μm.

We now chose the mutant huntingtin (mHtt) protein in Huntington's disease as our model system for pulse-chase imaging demonstration. It is believed that Huntington's disease is caused by a mutation from normal huntingtin gene to mHtt gene expressing aggregation-prone mHtt proteins with poly-glutamine (polyQ) expansion[3]. For easy visualization by fluorescence, we tagged mHtt (with 94Q) with a fluorescent protein marker, mEos2. As illustrated by the cartoon in Fig. 4.13d, HeLa cells were first transfected with mHtt94Q-mEos2 plasmid in regular medium for 4 h, and then replaced with group II D-AA medium for 22 h before changing to group I D-AA medium for another 20 h. SRS images are acquired at 2067 cm^{-1} and 2133 cm^{-1} channels, respectively, and subsequently processed with linear combination.

Fluorescence overlaid with bright field image informs us the formation of a large aggregate triggered by aggregation-prone polyQ expansion in mHtt94Q-mEos2 (Fig. 4.13d, fluorescence). Interestingly, proteins labeled with group II D-AAs during the initial pulse period mainly concentrate within the core of the aggregate (Fig. 4.13d, red), whereas proteins labeled with group I D-AAs during the subsequent chase period occupy the entire volume of the aggregate (Fig. 4.13d, green). The merged image between group I and group II images, as well as the intensity profiles across the aggregate, further confirm the observation of a yellow core inside and a green shell outside (Fig. 4.13d, merged). This two-color pulse-chase result suggests that the core is aggregated earlier in time and the later produced mHtt proteins are then recruited to and percolate through the aggregate to increases its overall size, in agreement with recently reported results by fluorescence[48]. The demonstration here thus illustrates that our imaging platform using

the two subgroups of D-AAs is readily applicable for performing pulse-chase imaging to probe the complex and dynamic aspects of proteome metabolism.

4.5 Conclusion

The ability to probe complex proteome metabolism with high sensitivity, resolution and biocompatibility will help us gain deep insights into protein metabolic regulation in biological systems in healthy and diseased conditions. We have thus presented such a platform by coupling SRS imaging with metabolic labeling of D-AAs from cellular level applications to complex tissue level and all the way to *in vivo* animal visualization.

Technically, compared to the exiting methods for probing proteomes such as BONCAT, SILAC and MIMS, our technique is mostly superior in its biocompatibility, thanks to the unique coupling of stable isotope labeling with SRS imaging, which also brings significant advantages in terms of specific utilities of the platform. The "bioorthognality" of C-D together with the background-free nature of SRS microscopy render protein synthesis detection to be highly sensitive and selective; for protein degradation, the linear concentration dependence and the Raman spectral fidelity of SRS allow quantitative retrieval for the pure CH_2 and CH_3 signals; for two-color imaging, the narrow-band SRS excitation using picosecond pulses permits the rich spectral diversity of D-AAs to be exploited for coding distinct protein populations. All these technical advantages are difficult to achieve by Coherent Anti-stokes Raman scattering (CARS) which is known for its non-resonant background, nonlinear dependence on analyte concentrations and severe spectral distortion[24].

Biologically, the presented platform will pave the way for interogating a broad range of complex systems such as memory-related protein sythesis in hippocampal brain tissues, protein aggregation and degradation in neurodegenerative diseases, and protein metabolism in animal disease models. Furthermore, considering that stable isotope labeling and SRS imaging are both compatible with live humans[30], we envision a bright prospect of applying this platform to performing diagnostic and theraputic imaging in humans.

4.6 Materials and methods.

Deuterated amino acids (D-AAs) culture media. Deuterium-labeled leucine-d_{10} medium is made by adding leucine-d_{10} (0.8 mM), lysine (0.8 mM) and arginine (0.4 mM) (Sigma) into leucine, lysine and arginine deficient DMEM medium (Sigma). Deuterium-labeled all amino acids medium (used in sections 4.2.4-4.2.6) is made by adding uniformly deuterium-labeled amino acid mix (20aa) (Cambridge Isotope, MA) into leucine, lysine and arginine deficient DMEM medium (Sigma). The final concentration of leucine-d_{10} is adjusted to be 0.8 mM among the amino acid mix. HeLa, HEK293T and N2A cells from sections 4.2.4-4.2.6 are seeded on a coverslip in a Petri-dish with 2 mL of regular DMEM medium with 10% FBS and 1% penicillin/streptomycin (Invitrogen) growing at 37 °C in a 5% CO_2 atmosphere for 20 hrs. The regular medium is then replaced with medium containing either leucine-d_{10} or deuterium-labeled all amino acids. After incubation for a certain amount of time, the coverslip is then taken out to make an imaging chamber filled with PBS for SRS imaging. For N2A cells, in the process of

induced cell differentiation with serum deprivation and 1 μM retinoic acid, deuterium-labeled all amino acids are supplemented

All the custom-made optimum efficiency D-AAs media are listed from Table 1-4.

1) D-AA medium (CD-DMEM) for HeLa cells in 4.2.7: adapted from regular recipe of DMEM medium (11965, Invitrogen). The D-AA culture medium for HeLa cells was made with 90% CD-DMEM, 10% FBS (10082, invitrogen) and 1X penicillin/streptomycin (15140, invitrogen).

Table 1 CD-DMEM for HeLa cells in 4.2.7

Amino acids components	Concentration (mM)	Product company and catalog number
Glycine-d_5	0.4	DLM-280, Cambridge isotope
L-Arginine·HCl-d_7	0.398	DLM-541, Cambridge isotope
L-Cysteine·2HCl	0.2	C6727, SIGMA (regular)*
L-Glutamine-d_5	4.0	DLM-1826, Cambridge isotope
L-Histidine·HCl·H_2O	0.2	H5659, SIGMA (regular)*
L-Isoleucine-d_{10}	0.802	DLM-141, Cambridge isotope
L-Leucine-d_{10}	0.802	DLM-567, Cambridge isotope
L-Lysine·HCl-d_8	0.798	616214, ALDRICH (Isotech)
L-Methionine-d_3	0.201	DLM-431, Cambridge isotope
L-Phenylalanine-d_8	0.4	DLM-372, Cambridge isotope
L-Serine-d_3	0.4	DLM-582, Cambridge isotope
L-Threonine	0.798	T8441, SIGMA (regular)*
L-Tryptophan	0.078	T8941, SIGMA (regular)*
L-Tyrosine-d_2	0.398	DLM-2317, Cambridge isotope
L-Valine-d_8	0.803	DLM-488, Cambridge isotope
Other components (vitamins, Inorganic Salts and glucose) are exactly the same as in the regular DMEM medium (11965, invitrogen).		

*The reasons these 4 amino acids are remain in their regular forms are because: first, their deuterated forms have limited number of side chain deuterium and are also relatively expensive; second, their occurrence (percentage) in mammalian cell proteins are small[29]. Thus the lack of the deuterated version for these 4 amino acids would not influence the general deuterium labeling efficiency for CD-DMEM. Same reason applies to below media.

2) D-AA medium (CD-Neurobasal A) for hippocampal neuron culture and organotypic brain slices: adapted from regular recipe of Neurobasal A medium (10888, Invitrogen). The D-AAs culture medium for hippocampal neurons was made of CD-Neurobasal A Medium, 1x B27 serum free supplement (17504, Invitrogen) and 0.5 mM glutamine-d_5 (DLM-1826, Cambridge isotope). The CD-Neurobasal A culture medium for organotypic brain slices was made of CD-Neurobasal A Medium, 1X B27 serum free supplement (17504, Invitrogen), 0.5% glucose (15023, invitrogen), 2 mM glutamine-d_5 (DLM-1826, Cambridge isotope) and 1X penicillin/streptomycin (15140, invitrogen).

Table 2 CD-Neurobasal A for hippocampal neuron and organotypic brain slices

Amino acids components	Concentration (mM)	Product company and catalog number
Glycine-d_5	0.4	DLM-280, Cambridge isotope
L-Alanine-d_4	0.022	DLM-250, Cambridge isotope
L-Arginine·HCl-d_7	0.398	DLM-541, Cambridge isotope
L-Asparagine-d_8	0.006	672947 ALDRICH (Isotech)
L-Cysteine·2HCl	0.26	C6727, SIGMA (regular)*
L-Histidine·HCl·H_2O	0.2	H5659, SIGMA (regular)*
L-Isoleucine-d_{10}	0.802	DLM-141, Cambridge isotope
L-Leucine-d_{10}	0.802	DLM-567, Cambridge isotope
L-Lysine·HCl-d_8	0.798	616214, ALDRICH (Isotech)
L-Methionine-d_3	0.201	DLM-431, Cambridge isotope
L-Phenylalanine-d_8	0.4	DLM-372, Cambridge isotope
L-Proline-d_7	0.067	DLM-487, Cambridge isotope
L-Serine-d_3	0.4	DLM-582, Cambridge isotope
L-Threonine	0.798	T8441, SIGMA (regular)*
L-Tryptophan	0.078	T8941, SIGMA (regular)*
L-Tyrosine-d_2	0.398	DLM-2317, Cambridge isotope
L-Valine-d_8	0.803	DLM-488, Cambridge isotope
Other components (vitamins, Inorganic Salts and glucose) are exactly the same as in the regular Neurobasal A medium (10888, Invitrogen).		

3) Group I D-AA medium for HeLa cells. The group I D-AA culture medium for HeLa cells was made with 90% group I D-AA medium, 10% FBS (10082, invitrogen) and 1X penicillin/streptomycin (15140, invitrogen).

Table 3 Group I D-AA medium

Amino acids components	Concentration (mM)	Product company and catalog number
Glycine	0.4	50046, SIGMA (regular)
L-Arginine·HCl	0.398	A6969, SIGMA (regular)
L-Cysteine·2HCl	0.2	C6727, SIGMA (regular)
L-Glutamine	4.0	G8540, SIGMA (regular)
L-Histidine·HCl·H_2O	0.2	H5659, SIGMA (regular)
L-Isoleucine-d_{10}	0.802	DLM-141, Cambridge isotope
L-Leucine-d_{10}	0.802	DLM-567, Cambridge isotope
L-Lysine·HCl	0.798	L8662 SIGMA (regular)
L-Methionine	0.201	M5308 SIGMA (regular)
L-Phenylalanine	0.4	P5482 SIGMA (regular)
L-Serine	0.4	S4311 SIGMA (regular)
L-Threonine	0.798	T8441, SIGMA (regular)
L-Tryptophan	0.078	T8941, SIGMA (regular)
L-Tyrosine	0.398	T8566 SIGMA (regular)
L-Valine-d_8	0.803	DLM-488, Cambridge isotope
Other components (vitamins, Inorganic Salts and glucose) are exactly the same as in the regular DMEM medium (11965, invitrogen).		

4) Group II D-AA medium for HeLa cells. The group II D-AA culture medium for HeLa cells was made with 90% group II D-AA medium, 10% FBS (10082, invitrogen) and 1X penicillin/streptomycin (15140, invitrogen).

Table 4 Group II D-AA medium

Amino acids components	Concentration (mM)	Product company and catalog number
Glycine-d_5	0.4	DLM-280, Cambridge isotope
L-Arginine·HCl-d_7	0.398	DLM-541, Cambridge isotope

L-Cysteine·2HCl	0.2	C6727, SIGMA (regular)
L-Glutamine-d_5	4.0	DLM-1826, Cambridge isotope
L-Histidine·HCl·H_2O	0.2	H5659, SIGMA (regular)
L-Isoleucine	0.802	I7403 SIGMA (regular)
L-Leucine	0.802	L8912 SIGMA (regular)
L-Lysine·HCl-d_8	0.798	616214, ALDRICH (Isotech)
L-Methionine-d_3	0.201	DLM-431, Cambridge isotope
L-Phenylalanine-d_8	0.4	DLM-372, Cambridge isotope
L-Serine-d_3	0.4	DLM-582, Cambridge isotope
L-Threonine	0.798	T8441, SIGMA (regular)
L-Tryptophan	0.078	T8941, SIGMA (regular)
L-Tyrosine-d_2	0.398	DLM-2317, Cambridge isotope
L-Valine	0.803	V0513 SIGMA (regular)
Other components (vitamins, Inorganic Salts and glucose) are exactly the same as in the regular DMEM medium (11965, invitrogen).		

5) D-AA medium (CD-MEM) for organotypic brain slice: adapted from regular recipe of MEM medium (11095, Invitrogen). The CD-MEM culture medium for organotypic brain slice was made with 90% CD-MEM, 10% FBS (10082, invitrogen), 0.5% glucose (15023, invitrogen) and 1X penicillin/streptomycin (15140, invitrogen).

Table 5 CD-MEM for organotypic brain slices

Amino acids components	Concentration (mM)	Product company and catalog number
L-Arginine·HCl-d_7	0.597	DLM-541, Cambridge isotope
L-Cysteine·2HCl	0.1	C6727, SIGMA (regular)*
L-Glutamine-d_5	2.0	DLM-1826, Cambridge isotope
L-Histidine·HCl·H_2O	0.2	H5659, SIGMA (regular)*
L-Isoleucine-d_{10}	0.397	DLM-141, Cambridge isotope
L-Leucine-d_{10}	0.397	DLM-567, Cambridge isotope
L-Lysine·HCl-d_8	0.399	616214, ALDRICH (Isotech)
L-Methionine-d_3	0.1	DLM-431, Cambridge isotope
L-Phenylalanine-d_8	0.19	DLM-372, Cambridge isotope
L-Threonine	0.403	T8441, SIGMA (regular)*
L-Tryptophan	0.049	T8941, SIGMA (regular)*
L-Tyrosine-d_2	0.199	DLM-2317, Cambridge isotope
L-Valine-d_8	0.393	DLM-488, Cambridge isotope
Other components (vitamins, **Inorganic Salts and glucose**) are exactly the same as in the regular MEM medium (11095, invitrogen).		

Metabolic incorporation of deuterated amino acids. For HeLa cells: cells are seeded on a coverslip in a petri-dish with 2 mL of regular medium for 20 h, and then replaced with D-AA medium (or group I and group II D-AA media) for designated amount of time. The coverslip is taken out to make an imaging chamber filled with PBS for SRS imaging. For hippocampal neurons, the dissociated neurons from newborn mice are seeded for 10 days in regular Neurobasal A medium, and then replaced with the corresponding D-AA medium for designated amount of time before imaging. For organotypic brain slice, 400 μm thick, P10 mouse brain slices are cultured on Millicell-CM inserts (PICM03050, millipore) in 1 mL CD-MEM culture medium for 2 h, and then change to in 1 mL CD-neurobasal A culture medium for another 28 h before imaging. For zebrafish: Wild-type zebrafish embryos at the 1-cell stage were injected with 1 nL D-AA solution and allowed to develop normally for another 24 h. The zebrafish embryos at 24 hpf were manually dechorionated before imaging. D-AA solution was made of 150 mg uniformly deuterium-labeled amino acid mix (20 aa) (DLM-6819, Cambridge Isotope) dissolved in 1 mL PBS, with subsequent filtration using Millipore sterile syringe Filters (0.22 μm, SLGV033RS). For mice: 1. Oral administration: 3-week-old mice were fed with D-AA containing drinking water for 12 days before harvesting the liver and intestine tissues. The drinking water was made of 500 mg uniformly deuterium-labeled amino acid mix (20 aa) (DLM-6819, Cambridge Isotope) dissolved in 200 ml PBS, with subsequent filtration using Millipore sterile syringe Filters (0.22 μm, SLGV033RS). 2. Intraperitoneal injection: 3-week-old mice were injected with 500 μl D-AAs solution at the 0^{th} h, 12^{th} h and 24^{th} h. The tissues were then harvested at the 36^{th} h after the first injection. D-AA solution was made of 500 mg uniformly deuterium-labeled amino acid

mix (20 aa) (DLM-6819, Cambridge Isotope) dissolved in 2 ml PBS solutions, with subsequent filtration using Millipore sterile syringe Filters (0.22 μm, SLGV033RS). The experimental protocol for *in vivo* mice experiments (AC-AAAG2702) and zebrafish experiments (AC-AAAD6300) were approved by Institutional Animal Care and Use Committee at Columbia University.

Retrieval of pure CH_3 and CH_2 signals by linear combination between 2940 cm^{-1} and 2845 cm^{-1} channels. The employed equations follow ref. 40, 41. Pure CH_3 signal can be retrieved as $[c]_{protein} \propto 5.2*(2940\ cm^{-1}\ signal) - 4.16*(2845\ cm^{-1}\ signal)$; Pure CH_2 signal can be retrieved as $[c]_{lipid} \propto 1.2*(2845\ cm^{-1}\ signal) - 0.3*(2940\ cm^{-1}\ signal)$. This algorithm was tested with skin tissue samples, yielding similar results as reported in ref. 40, 41.

Two-color pulse-chase linear combination algorithm between 2067 cm^{-1} and 2133 cm^{-1} channels. In order to achieve SRS imaging of pure group I D-AA labeled protein distribution and pure group II D-AA labeled protein distribution simultaneously, we construct a robust linear combination algorithm to retrieve the underlying pure concentration information for two-color pulse-chasing imaging similar to the one presented above from ref. (27, 28). Since SRS signals exhibit linear concentration dependence with analyte concentrations, two chemical species with different Raman spectra can be retrieved quantitatively with two-color SRS imaging. Hence, based on the spectra shown in Fig. 4c, we choose to acquire narrow-band SRS images at 2067 cm^{-1} and

2133 cm^{-1} channels, respectively, and perform subsequent linear combination algorithm to remove the spectral cross-talk.

The proper algorithm with the corresponding cross-talk coefficients is constructed with SRS images of standard reference samples, i.e., pure group I D-AA labeled protein and pure group II D-AA labeled protein. To do so, we labeled HeLa cells with only group I D-AA medium and only group II D-AA medium, respectively, and acquired a set of image pairs at 2067 cm^{-1} and 2133 cm^{-1} channels for each cell samples (Fig. 4.14).

For any sample labeled with both groups of D-AAs, the measured SRS signals at 2067 cm^{-1} and 2133 cm^{-1} channels can be written as the following, with linear relationship to group I D-AA and group II D-AA concentrations ($[c]_{group\ I}$ and $[c]_{group\ II}$) :

$$\begin{bmatrix} 2067\,cm^{-1}\ signal \\ 2133\,cm^{-1}\ signal \end{bmatrix} = \begin{bmatrix} i_{group\,I,2067cm^{-1}} & i_{group\,II,2067cm^{-1}} \\ i_{group\,I,2133cm^{-1}} & i_{group\,II,2133cm^{-1}} \end{bmatrix} \begin{bmatrix} [c]_{group\,I} \\ [c]_{group\,II} \end{bmatrix},$$

where $i_{group\,I,2067cm^{-1}}$, $i_{group\,I,2133cm^{-1}}$, $i_{group\,II,2067cm^{-1}}$, $i_{group\,II,2133cm^{-1}}$ are the average pixel intensity recorded inside cells in (a) and (b) of Supplemental Fig. 1.

Thus group I D-AA and group II D-AA concentrations can then be easily solved as:

$$[c]_{group\,I} = \frac{i_{group\,II,2133cm^{-1}}(2067\,cm^{-1}\ signal) - i_{group\,II,2067cm^{-1}}(2133\,cm^{-1}\ signal)}{i_{group\,II,2133cm^{-1}} i_{group\,I,2067cm^{-1}} - i_{group\,II,2067cm^{-1}} i_{group\,I,2133cm^{-1}}},$$

$$[c]_{group\,II} = \frac{i_{group\,I,2067cm^{-1}}(2133\,cm^{-1}\ signal) - i_{group\,I,2133cm^{-1}}(2067\,cm^{-1}\ signal)}{i_{group\,II,2133cm^{-1}} i_{group\,I,2067cm^{-1}} - i_{group\,II,2067cm^{-1}} i_{group\,I,2133cm^{-1}}}.$$

Taking the average pixel intensity recording in (a) and (b) from Supplemental Fig. 1 into the above equations, the final linear combination algorithm reads as:

$$[c]_{\text{group I}} \propto 1.06*(2067\ \text{cm}^{-1}\ \text{signal}) - 0.0047*(2133\ \text{cm}^{-1}\ \text{signal}) \quad (4.2)$$

$$[c]_{\text{group II}} \propto (2133\ \text{cm}^{-1}\ \text{signal}) - 1.15*(2067\ \text{cm}^{-1}\ \text{signal}) \quad (4.3)$$

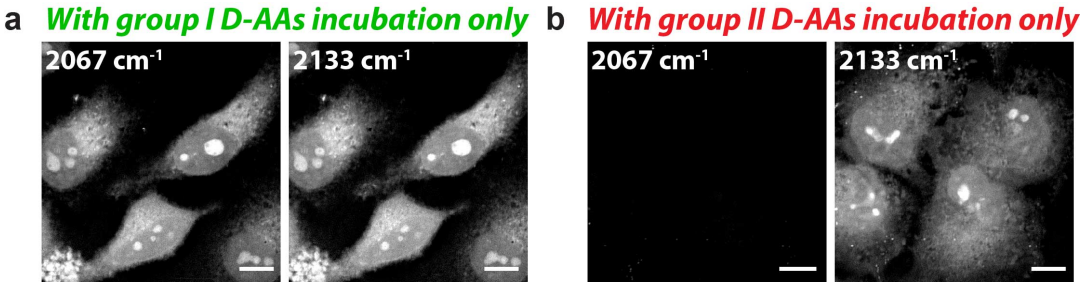

Fig. 4.14 SRS images for linear combination algorithm. SRS images at 2067 cm^{-1} and 2133 cm^{-1} channels of proteins labeled with group I D-AA only (a) and group II D-AA only (b).

4.7 Instrumentation Summary.

Stimulated Raman scattering microscopy. Refer to chapter 2 for a more detailed description. For sections 4.2.3-4.2.6 before the optimization of the instrument: A 60X water objective (UPlanAPO/IR, 1.2 N.A., Olympus) with high near IR transmission is used for all cell imaging. After passing through the sample, the forward going Pump and Stokes beams are collected in transmission by a high N.A. condenser and imaged onto a large area Si photodiode. A high O.D. bandpass filter (890/220, Chroma) is used to block the Stokes beam completely and to transmit the Pump beam only for the detection of the stimulated Raman loss signal. The output current from the photodiode is terminated with 50 Ω, pre-filtered by a bandpass filter (BBP-10.7; Mini Circuits) and demodulated by a lock-in amplifier (SR844, Stanford Research Systems) at 10 MHz to ensure shot-noise-limited detection sensitivity. For imaging, 512 by 512 pixels are acquired for one frame

with a 100 μs pixel dwell time and 20 μs time constant from the lock-in amplifier. Powers after 60X IR objective used for imaging are: 61 mW for modulated Stokes beam; 145 mW for the Pump beam of 2133 cm^{-1}, 2000 cm^{-1} and 1655 cm^{-1} channels and 64 mW for Pump beam of 2950 cm^{-1} and 2845 cm^{-1} channels.

For sections 4.2.7-4.4 with the optimization of the instrument: A 60X water objective (UPlanAPO/IR, 1.2 N.A., Olympus) with high near IR transmission is used for all cellular level imaging, and a 25X water objective (XLPlan N, 1.05 N.A., MP, Olympus) with both high near IR transmission and large field of view is used for brain tissue and *in vivo* imaging. The Pump/Stokes beam size is matched to fill the back-aperture of the objective. The forward going Pump and Stokes beams after passing through the sample are collected in transmission with a high N.A. condenser lens (oil immersion, 1.4 N.A., Olympus), which is aligned following Köhler illumination. A telescope is then used to image the scanning mirrors onto a large area (10 mm by 10 mm) Si photodiode (FDS1010, Thorlabs) to descan beam motion during laser scanning. The photodiode is reverse-biased by 64 V from a DC power supply to increase both the saturation threshold and response bandwidth. A high O.D. bandpass filter (890/220 CARS, Chroma Technology) is used to block the Stokes beam completely and transmit the Pump beam only. The output current of the photodiode is electronically pre-filtered by an 8-MHz band-pass filter (KR 2724, KR electronics) to suppress both the 80 MHz laser pulsing and the low-frequency contribution due to laser scanning across the scattering sample. It is then fed into a radio frequency lock-in amplifier (HF2LI, Zurich instrument) terminated with 50 Ω to demodulate the stimulated Raman loss signal

experienced by the Pump beam. The R-output of the lock-in amplifier is fed back into the analog interface box (FV10-ANALOG) of the microscope.

For HeLa cell imaging and brain tissue imaging, the time constant of the lock-in amplifier is set for 8 μs, and the images are acquired by a 12.5 μs pixel dwell time, corresponding to 3.3 s for a 512-by-512 pixel frame. For neurons and *in vivo* imaging of embryonic zebrafish and mice livers and intestines, the time constant is set to be 20 μs, and the images are acquired by a 40 μs of pixel dwell time, corresponding to 10.5 s for a 512-by-512 pixel frame. Laser powers after 60X IR objective used for cell imaging are: 100 mW for modulated Stokes beam and 112 mW for the Pump beam at 2133 cm^{-1}, 2000 cm^{-1} and 1655 cm^{-1} channels; 50 mW for modulated Stokes beam and 56 mW for Pump beam at 2940 cm^{-1} and 2845 cm^{-1} channels. Laser powers after 25X objective used for tissue and *in vivo* imaging are: 134 mW for modulated Stokes beam; 120 mW for the Pump beam of 2133 cm^{-1}, 2000 cm^{-1} and 1655 cm^{-1} channels; 67 mW for modulated Stokes beam and 60 mW for Pump beam at 2940 cm^{-1} and 2845 cm^{-1} channels.

Spontaneous Raman spectroscopy. The spontaneous Raman spectra were acquired using a laser Raman spectrometer (inVia Raman microscope, Ranishaw) at room temperature. A 27 mW (after objective) 532 nm diode laser was used to excite the sample through a 50X, N.A. 0.75 objective (NPLAN EPI, Leica). The total data acquisition was performed during 60 seconds using the WiRE software. All the spontaneous Raman spectra have subtracted the PBS solution as background.

4.8 References.

1. Mayford, M., Siegelbaum, S.-A. & Kandel, E.-R. Synapses and memory storage. *Cold Spring Harb. Perspect. Biol.* 4, a005751 (2012).
2. Sutton, M.-A., Schuman & E.-M. Dendritic protein synthesis, synaptic plasticity, and memory. *Cell* **127**, 49–58 (2006).
3. Walker, F.-O. Huntington's Disease. *The Lancet.* **369**, 218–228 (2007).
4. Bennett, E.-J et al. Global changes to the ubiquitin system in Huntington's disease. *Nature* **448**, 704–708 (2007).
5. Lipton, P., Raley-Susman & K.-M. Autoradiographic measurements of protein synthesis in hippocampal slices from rats and guinea pigs. *Methods* **18**, 127–143 (1999).
6. Bachmair, A., Finley, D. & Varshavsky, A. In vivo half-life of a protein is a function of its amino-terminal residue. *Science* **234**, 179–186 (1986).
7. Ong, S.-E. et al. Stable isotope labeling by amino acids in cell culture, SILAC, as a simple and accurate approach to expression proteomics. *Mol. Cell. Proteomics* **1**, 376–386 (2002).
8. Mann, M. Functional and quantitative proteomics using SILAC. *Nat. Rev. Mol. Cell Biol.* **7**, 952–958 (2006).
9. Lechene, C. et al. High-resolution quantitative imaging of mammalian and bacterial cells using stable isotope mass spectrometry. *J. Biol.* **5**, 20 (2006).
10. Zhang, D. -S. et al. Multi-isotope imaging mass spectrometry reveals slow protein turnover in hair-cell stereocilia. *Nature* **481**, 520–524 (2012).
11. Beatty, K.-E. et al. Fluorescence visualization of newly synthesized proteins in mammalian cells. *Angew. Chem. Int. Ed. Engl.* **45**, 7364–7367 (2006).
12. Ngo, J.-T. & Tirrell, D.-A. Noncanonical amino acids in the interrogation of cellular protein synthesis. *Acc. Chem. Res.* **44**, 677–685 (2011).
13. Yuet, K.-P. & Tirrell, D.-A. Chemical tools for temporally and spatially resolved mass spectrometry-based proteomics. *Ann. Biomed. Eng* (2013).
14. Liu, J., Xu, Y., Stoleru, D. & Salic, A. Imaging protein synthesis in cells and tissues with an alkyne analog of puromycin. *Proc. Natl. Acad. Sci. USA* **109**, 413–418 (2012).

15. Prescher, J.-A. & Bertozzi, C.-R. Chemistry in living systems. *Nat. Chem. Biol.* **1**, 13–21 (2005).
16. Bertozzi, C.-R. A decade of bioorthogonal chemistry. *Acc. Chem. Res.* **44**, 651–653 (2011).
17. Grammel, M. & Hang, H.-C. Chemical reporters for biological discovery. *Nat. Chem. Biol.* **9**, 475–484 (2013).
18. Moore, F.-D., Determination of total body water and solids with isotopes. *Science* **104**, 157–160 (1946).
19. Pinkus, J., Charles, D. & Chattoraj, S. Deuterium-labeled Steroids for Study in Humans: I. estrogen production rates in normal pregnancy. *J. Biol. Chem.* **245**, 633–636 (1971).
20. Tang, G., Qin, J. & Dolnikowski, G.-G. Deuterium enrichment of retinol in humans determined by gas chromatography electron capture negative chemical ionization mass spectrometry. *J. Nutr. Biochem.* **9**, 408–414 (1998).
21. Freudiger, C.-W. et al. Label-free biomedical imaging with high sensitivity by stimulated Raman scattering microscopy. *Science.* **322**, 1857–1861 (2008).
22. Min, W. Label-free optical imaging of nonfluorescent molecules by stimulated radiation. *Curr. Opin. Chem. Biol.* **15**, 831–837 (2011).
23. Min, W., Freudiger, C.-W., Lu, S. & Xie, X.-S. Coherent nonlinear optical imaging: beyond fluorescence microscopy. *Annu. Rev. Phys. Chem.* **62**, 507–530 (2011).
24. Cheng, J.-X. & Xie, X.-S. *Coherent Raman Scattering Microscopy* (CRC Press) (2012).
25. Hershey, J. W. B., Sonenberg, N. & Mathews, M. B. Eds. Protein synthesis and translational control. *Cold Spring Harbor Laboratory Press* (2012).
26. Martin, K. C., Barad, M. & Kandel, E. R. Local protein synthesis and its role in synapse-specific plasticity. *Curr. Opin. Neurobiol.* **10**, 587–592 (2000).
27. Kandel, E. R. The molecular biology of memory storage: a dialogue between genes and synapses. *Science* **294**, 1030–1038 (2001).
28. Ho, V. M., Lee, J. A. & Martin, K. C. The cell biology of synaptic plasticity. *Science* **334**, 623–628 (2011).

29. Okayasu, T., Ikeda, M., Akimoto, K. & Sorimachi, K. The amino acid composition of mammalian and bacterial cells. *Amino Acids* **13**, 379–391 (1997).
30. Saar, B. G. et al. Video-rate molecular imaging in vivo with stimulated Raman scattering. *Science* **330**, 1368–1370 (2010).
31. Phair, R. D. & Misteli, T. High mobility of proteins in the mammalian cell nucleus. *Nature* **404**, 604-609 (2000).
32. Andersen, J. S. et al. Nucleolar proteome dynamics. *Nature* **433**, 77-83 (2005).
33. Boisvert FM et al. A quantitative spatial proteomics analysis of proteome turnover in human cells. *Mol. Cell. Proteomics* **11**, M111.011429 (2012).
34. Piez, K.-A. & Eagle, H. The free amino acid pool of cultured human cells. *J. Biol. Chem.* **231**, 533–545 (1958).
35. Deng, W., Aimone, J.-B. & Gage, F.-H. New neurons and new memories: how does adult hippocampal neurogenesis affect learning and memory? *Nat. Rev. Neurosci.* **11**, 339–350 (2010).
36. Dieterich, D.-C. et al. In situ visualization and dynamics of newly synthesized proteins in rat hippocampal neurons. *Nat. Neurosci.* **13**, 897–905 (2010).
37. Hinz, F.-I., Dieterich, D.-C. & Schuman, E.-M. Teaching old NCATs new tricks: using non-canonical amino acid tagging to study neuronal plasticity. *Curr. Opin. Chem. Biol.* **17**, 738–746 (2013).
38. Kari, G., Rodeck, U. & Dicker, A.-P. Zebrafish: an emerging model system for human disease and drug discovery. *Clin. Pharmacol. Ther.* **82**, 70–80 (2007).
39. Hinz, F.-I., Dieterich, D.-C., Tirrell, D.-A. & Schuman, E.-M. Non-canonical amino acid labeling *in vivo* to visualize and affinity purify newly synthesized proteins in larval zebrafish. *ACS Chem. Neurosci.* **3**, 40–49 (2012).
40. Lu, F.-K. et al. Multicolor stimulated Raman scattering microscopy. *Mol. Phys.* **110**, 1927–1932 (2012).
41. Yu, Z. et al. Label-free chemical imaging in vivo: three-dimensional non-invasive microscopic observation of amphioxus notochord through stimulated Raman scattering (SRS). *Chem. Sci.* **3**, 2646–2654 (2012).
42. Ji, M. et al. Rapid, label-free detection of brain tumors with stimulated Raman scattering microscopy. *Sci. Transl. Med.* **5**, 201ra119 (2013).

43. Cambridge, S.-B. et al. Systems-wide proteomic analysis in mammalian cells reveals conserved, functional protein turnover. *J. Proteome Res.* **10**, 5275–5284 (2011).
44. Beatty, K.-E. & Tirrell, D.-A. Two-color labeling of temporally defined protein populations in mammalian cells. *Bioorg. Med. Chem. Lett.* **18**, 5995–5999 (2008).
45. Zhang, D. et al. Quantitative vibrational imaging by hyperspectral stimulated Raman scattering microscopy and multivariate curve resolution analysis. *Anal. Chem.* **85**, 98–106 (2013).
46. Zhang, D., Slipchenko, M.-N. & Cheng, J.-X. Highly sensitive vibrational imaging by femtosecond pulse stimulated Raman loss. *J. Phys. Chem. Lett.* **2**, 1248–1253 (2011).
47. Fu, D., Holtom, G., Freudiger, C.-W., Zhang & X., Xie, X.-S. Hyperspectral imaging with stimulated Raman scattering by chirped femtosecond lasers. *J. Phys. Chem. B* **117**, 4634–4640 (2013).
48. Schipper-Krom, S. et al. Dynamic recruitment of active proteasomes into polyglutamine initiated inclusion bodies. *FEBS Lett.* **588**, 151–159 (2014).

Chapter 5

Extending the fundamental imaging depth limit with multi-photon activation and imaging microscopy

The contents of this chapter has been published in:

Z. Chen*, **L. Wei***, X. Zhu* and W. Min. "Extending the fundamental imaging-depth limit of multi-photon microscopy by imaging with photo-activatable fluorophores", *Opt. Express* 20, 18525 (2012). *Co-first author

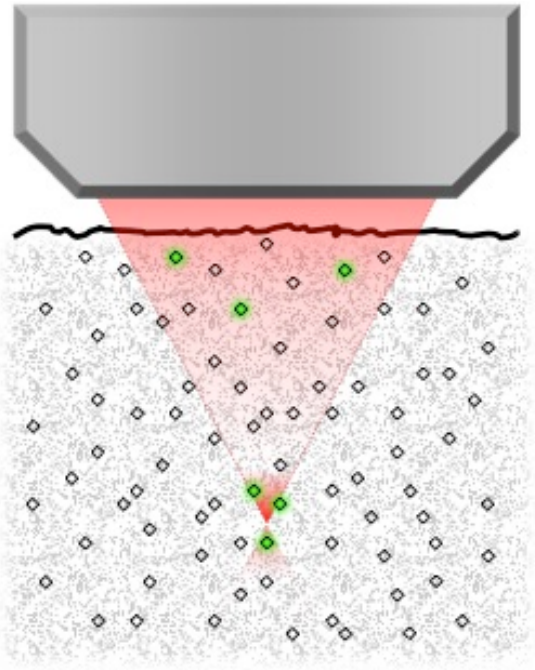

Abstract

It is highly desirable to be able to optically probe biological activities deep inside live organisms. By employing a spatially confined excitation via a nonlinear transition, multiphoton fluorescence microscopy has become indispensable for imaging scattering samples. However, as the incident laser power drops exponentially with imaging depth due to scattering loss, the out-of-focus fluorescence eventually overwhelms the in-focal signal. The resulting loss of imaging contrast defines a fundamental imaging-depth limit, which cannot be overcome by increasing excitation efficiency. Herein we propose to significantly extend this depth limit by multiphoton activation and imaging (MPAI) of photo-activatable fluorophores. The imaging contrast is drastically improved due to the created disparity of bright-dark quantum states in space. Theoretically, MPAI presents a fourth order power dependence, which is effectively four-photon process. Therefore it offers higher signal to background contrast and hence deeper imaging depth limit. Experimentally, we demonstrate this new principle on tissue phantoms labeled with synthetic caged fluorescein dye or genetically encodable photoactivatable GFP.

5.1 Introduction.

Advances in optical imaging technology have revolutionized our ability to study the microscopic world. However, compared to electron microscopy and magnetic resonance imaging, optical microscopy suffers intrinsically from relatively coarse spatial resolution and superficial penetration depth. While the diffraction-limited resolution barrier has been broken by several super-resolution fluorescence techniques[1-3], the deepest penetration into scattering samples is achieved currently by multi-photon microscopy. By employing a nonlinear optical excitation, multi-photon fluorescence is generated primarily at the laser focus where the probability of having two (or more) simultaneous photons is the highest, enabling an intrinsic optical sectioning[4, 5]. Such a spatially confined excitation permits the capture of fluorescence photons emitted from the focus by a wide-field detector without the need of a confocal pinhole, thereby dramatically increasing the detection sensitivity and hence imaging depth into scattering samples[6]. Consequently, multi-photon microscopy has become an indispensable tool for biomedicine and especially for neuroscience[7].

However, multiphoton fluorescence microscopy still exhibits a fundamental imaging-depth limit for scattering samples labeled with fluorophores[8–12]. As shown in Fig. 5.1a, the two-photon fluorescence image of fluorescent beads embedded in a turbid 3D sample quickly vanishes with the depth when using constant laser power. The corresponding cut-off depth is, however, not the true maximum. Practically, imaging can be performed much deeper when the laser power is elevated to compensate for the scattering loss (Fig. 5.1 b), but this comes at the cost of deteriorating imaging contrast.

Eventually, at a certain depth, it is no longer feasible to identify the target beads from the overwhelming background.

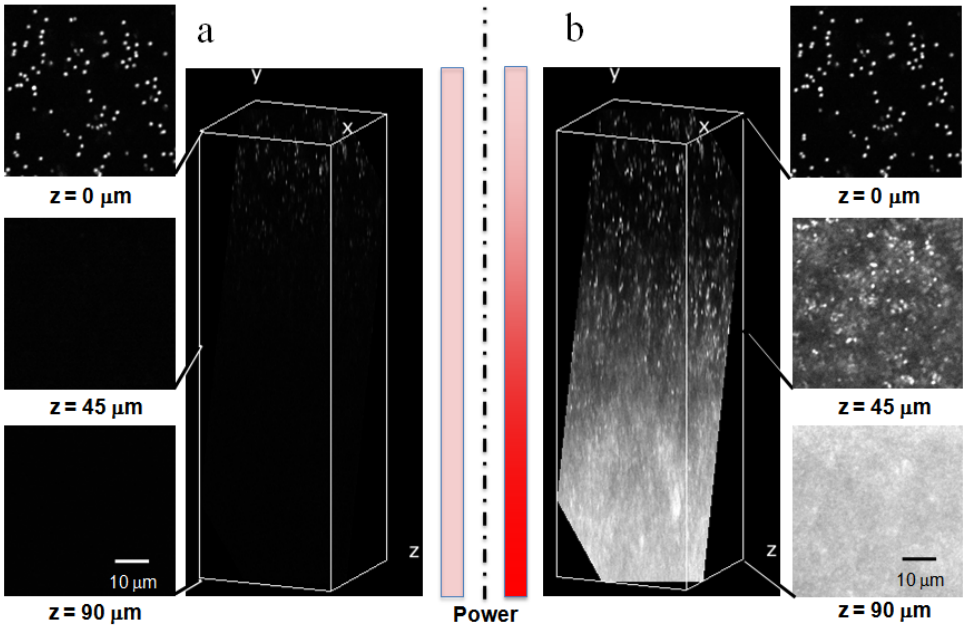

Fig. 5.1 Fundamental imaging-depth limit of multiphoton fluorescence microscopy. (a) Volume images of a tissue phantom consisting of 5% intralipid, 1 μm fluorescent beads and 1% agarose gel under a constant excitation laser power. Two-photon fluorescence signal quickly attenuates with the imaging depth. (b) Volume images of the same sample using a compensative higher laser power to maintain the signal strength at different depths. The resulting images, even though showing signals deeper into the sample, suffer from a loss of contrast as the out-of-focus background grows. The fundamental imaging-depth limit is defined when the in-focus signal and the out-of-focus background are equal to each other.

Such an imaging-depth limit arises because the approximation that multiphoton excited fluorescence is generated only within the focal volume does not always hold[9, 12]. To compensate for the scattering loss, one needs to increase the incident power exponentially with imaging depth. Eventually this exponential increase outstrips the power-law fall-off of the excitation efficiency, and the fluorescence from the out-of-focus beads begins to dominate inevitably (Fig. 5.1). Hence, the fundamental imaging-depth

limit is reached when the in-focus signal and the out-of-focus background are equal to each other[9]. Obviously, this limit cannot be overcome by further increasing incident laser power.

There have been tremendous efforts in improving the imaging depth of multiphoton microscopy, largely driven by the desire to perform *in vivo* deep tissue imaging[6]. Several strategies have been explored, such as adaptive optics designed to pre-compensate for the scattering loss[13, 14], imaging with longer excitation wavelength[15], chemical cleaning reagent[16], and differential aberration imaging[17]. Most of these methods aim to reduce the optical scattering effect of the sample on the incident laser beam. However, relatively little work has been published along the line of exploring novel imaging probes as a way of extending the imaging-depth limit.

Herein we present a new principle of multiphoton activation and imaging (MPAI) to extend the fundamental imaging-depth limit by using photo-activatable fluorophores (PAFs). PAFs are powerful imaging probes for tracking molecular and cellular dynamics with high temporal resolution, and have recently emerged as the key players in super-resolution fluorescence microscopy[1-3, 18-21]. Unlike traditional fluorophores which always remain in their bright states, PAFs permit photo-induced transitions from dark states to bright states. By preferentially inducing the bright states into the focus and dark states into the out-of-focus background, MPAI of PAFs can significantly enhance the imaging contrast and extend the depth limit of multiphoton microscopy. We demonstrate our proposal by both analytical theory and imaging experiments on tissue phantoms labeled

with synthetic caged fluorescein dye or photoactivatable Green Fluorescent Protein. Therefore, by offering the additional on-off molecular quantum states, PAFs seem to be capable of both breaking the diffraction-limited spatial resolution and extending the imaging-depth limit.

5.2 Theory and results.

5.2.1 The fundamental imaging-depth limit of two-photon microscopy.

Let us first frame the problem of deep two-photon imaging with regular fluorophores. The fundamental imaging-depth limit can be defined as the point where the in-focus signal and the out-of-focus background are equal[8-12]:

$$\left(\frac{S}{B}\right)_{regular} = \frac{\int_{V_{in}} \int_0^{\tau} C_S(r,z) I_i^2(r,z,t)\,\mathrm{d}t\,\mathrm{d}V}{\int_{V_{out}} \int_0^{\tau} C_B(r,z) I_i^2(r,z,t)\,\mathrm{d}t\,\mathrm{d}V} = 1 \qquad (5.1)$$

where V_{in}, is the focal volume at the focal plane, V_{out}, is the total sample volume along the light path but excluding the volume at the focal plane, r, is the distance from the optical axis, z, is the axial distance from the tissue surface, C, is the local fluorophore concentration, I_i, is the local imaging laser intensity, and τ, is the pixel dwell time during imaging. We assume that there is no fluorophore saturation or photobleaching and that the fluorescence collection efficiencies at the wide-field detector are identical for the signal and the background.

We can now analyze the laser intensity distribution within the scattering sample. In a typical scenario where the fluorophores are distributed throughout the sample volume, the number of out-of-focus fluorophores is almost always much larger than that of the in-

focus ones: $\int_{V_{out}} C_B(r,z)\mathrm{d}V >> \int_{V_{in}} C_S(r,z)\mathrm{d}V$. Therefore, at the fundamental imaging-depth limit as defined in Eq. (5.1), $I_i^2(r,z)\big|_{V_{in}}$ at the focus should be much larger than the out-of-focus counterpart $I_i^2(r,z)\big|_{V_{out}}$, despite of the scattering loss. Indeed, in the simple condition of homogeneous fluorophore distribution, i.e., $C_B(r,z) = C_S(r,z)$, $\int_V \int_0^\tau I_i^2(r,z,t)\mathrm{d}t\,\mathrm{d}V$ will be identical between the background and the signal, and consequently, the integral of $I_i^2(r,z)$ over a subset layers of the out-of-focus volume (e.g., $\int_{V_{out}} I_i^2(r,z)\mathrm{d}r$ for any z) will be smaller than that over the focus.

5.2.2 Reducing the background fluorophore concentration alone can improve the depth limit.

Although the sample scattering is seemingly the origin of the limited light penetration, the above theoretical framework suggests that the concentration of background fluorophores should play an important role in determining the depth limit. To separate these two effects, we constructed and imaged a set of "two-layer" samples (Fig. 5.2). 0~5 % intralipid emulsion was used as it closely mimics the response of biological tissue to near infrared light. In the absence of scattering intralipid, increasing fluorescein concentration in the background does not affect the two-photon imaging quality of the target fluorescent beads. In contrast, when the scattering effect is strong enough (e.g., 2% and 5% intralipid), the two-photon imaging contrast becomes anti-correlated with the background fluorescein concentration. Thus, both strong sample scattering and abundant background fluorophores are necessary conditions for limited imaging-depth. Sample scattering alone does not create poor imaging contrast. As an important insight, images

presented in Fig. 5.2 suggest that, simply reducing the background dye concentration while maintaining the high intralipid content still allows imaging the target beads with increased contrast and decent spatial resolution.

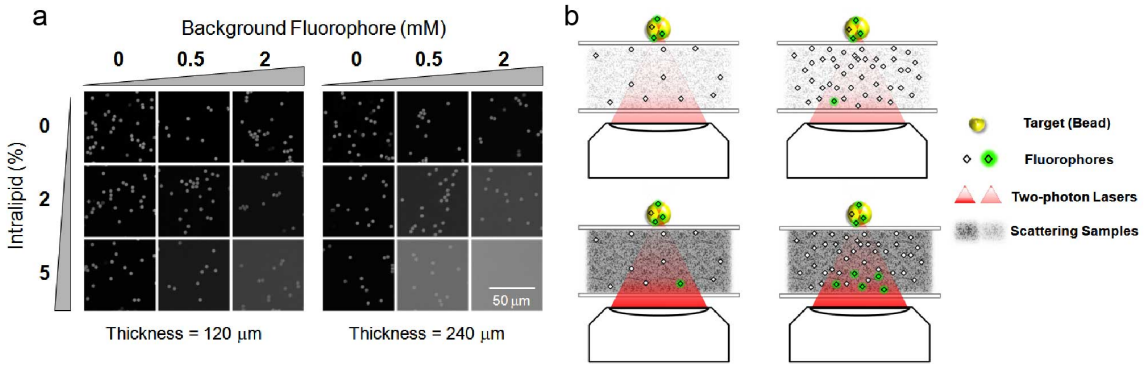

Fig. 5.2 Imaging contrast of multi-photon microscopy depends on both sample scattering and background fluorophore concentration. (a) Two-photon images of "two-layer" samples with varying intralipid contents and background dye concentrations. The laser power was set higher accordingly when a more scattering sample was imaged. At a given background layer thickness, image contrast deteriorates only when both a significant background turbidity and a dense background fluorophore staining are present. Imaging contrast further deteriorates when thicker background layers were applied. (b) Cartoon configuration for (a), in which fluorescent beads are placed on a glass coverslip as the target, while a thick layer of mixed fluorescein dye solution and scattering intralipids is inserted as the background between the target and the objective.

5.2.3 Theoretical framework of MPAI using dynamic PAFs.

Inspired by the above insight, we envisioned a way to preferentially keep the background fluorophores in the dark state by using PAFs which must first be activated by mutiphoton process to be converted to the bright state. Two different modes of experiments are possible: simultaneous or sequential activation and imaging. When PAFs are being activated and imaged by I_a and I_i (the same activation-imaging laser or two combined lasers, where I_a is the local intensity of the activation laser) simultaneously,

$C(r,z)$ in Eq. (1) should be replaced by $A(r,z,t)$, the time-dependent concentration of the PAFs in the bright state. Quantitatively, $A(r,z,t)$ will be the product of $C(r,z)$ and the time-dependent multiphoton activation yield, $\eta(t)$:

$$A(r,z,t) = C(r,z)\eta(r,z,t) \tag{5.2}$$

In the simplest condition, $\eta(t)$ follows a first-order chemical kinetics:

$$\eta(t) = 1 - \exp\left[-\sigma I_a^2(r,z,t)t\right] \qquad 0 \le t \le \tau \tag{5.3}$$

with the rate constant being proportional to $I_a^2(r,z)$ of the activation laser and the two-photon activation cross section, σ. Alternatively, we can describe the sequential mode in which activation by I_a and imaging by I_i are performed at two laser wavelengths in sequential raster scans: $A(r,z) = C(r,z)\eta(r,z,\psi)$ where ψ is the pixel dwell time of the multiphoton activation scanning process, and the resulting $A(r,z)$ becomes time independent for the subsequent imaging process. In this paper, we only present the more complex time-dependent $A(r,z,t)$ in the simultaneous mode.

When the timescale for PAFs to diffuse or transport out of the laser focal volume is shorter than the frame acquisition time, the accumulation of the activated fluorophores in the background during the scanning process could be neglected. This dynamic condition is rather common, as exemplified by *in vivo* blood vessel imaging in which fluorophores are injected into the circularoty systems of small animals[22]. Hence, the signal-to-background ratio for dynamic PAFs can be expressed as

$$\left(\frac{S}{B}\right)_{PAFs} = \frac{\int_{V_{in}} \int_0^\tau C_S(r,z)\left[1 - e^{-\sigma I_a^2(r,z,t)t}\right] I_i^2(r,z,t)\,\mathrm{d}t\,\mathrm{d}V}{\int_{V_{out}} \int_0^\tau C_B(r,z)\left[1 - e^{-\sigma I_a^2(r,z,t)t}\right] I_i^2(r,z,t)\,\mathrm{d}t\,\mathrm{d}V} \tag{5.4}$$

As was analyzed earlier, the laser intensity at the focus is much higher than its out-of-focus counterparts at the imaging-depth limit defined by Eq. (5.1). This would lead to a much higher dark-to-bright conversion yield at the focus: $\eta_S(r,z,t) > \eta_B(r,z,t)$, under a proper pixel dwell time with a non-saturating activation yield. Consequently, we expect a much improved signal-to-background ratio for PAFs than for regular fluorophores:

$$(S/B)_{PAFs} > (S/B)_{regular} \tag{5.5}$$

It is constructive to note that, after the photoactivation (with a non-saturating activation yield), the number of in-focus activated PAFs become comparable to the total number of the activated ones out-of-focus:

$$\left(\frac{N_S}{N_B}\right)_{activated} = \frac{\int_{V_{in}}\int_0^\tau C_S(r,z)\left[1-e^{-\sigma I_a^2(r,z,t)\tau}\right]\mathrm{d}t\,\mathrm{d}V}{\int_{V_{out}}\int_0^\tau C_B(r,z)\left[1-e^{-\sigma I_a^2(r,z,t)\tau}\right]\mathrm{d}t\,\mathrm{d}V} \approx \frac{\int_{V_{in}}\int_0^\tau C_S(r,z)I_a^2(r,z,t)\,\mathrm{d}t\,\mathrm{d}V}{\int_{V_{out}}\int_0^\tau C_B(r,z)I_a^2(r,z,t)\,\mathrm{d}t\,\mathrm{d}V} = 1 \tag{5.6}$$

Compared to the regular dye case in which:

$$\left(\frac{N_S}{N_B}\right)_{regular} = \frac{\int_{V_{in}} C_S(r,z)\,\mathrm{d}V}{\int_{V_{out}} C_B(r,z)\,\mathrm{d}V} \approx \frac{V_{in}}{V_{out}} << 1 \tag{5.7}$$

Eq. (5.6) clearly indicates that the bright states are preferentially induced at the focus whereas the out-of-focus PAFs mostly remain in dark states. As shown in Fig. 5.3c, such a remarkable disparity of bright-dark states in space significantly reduces the background contribution from out-of-focus fluorophores.

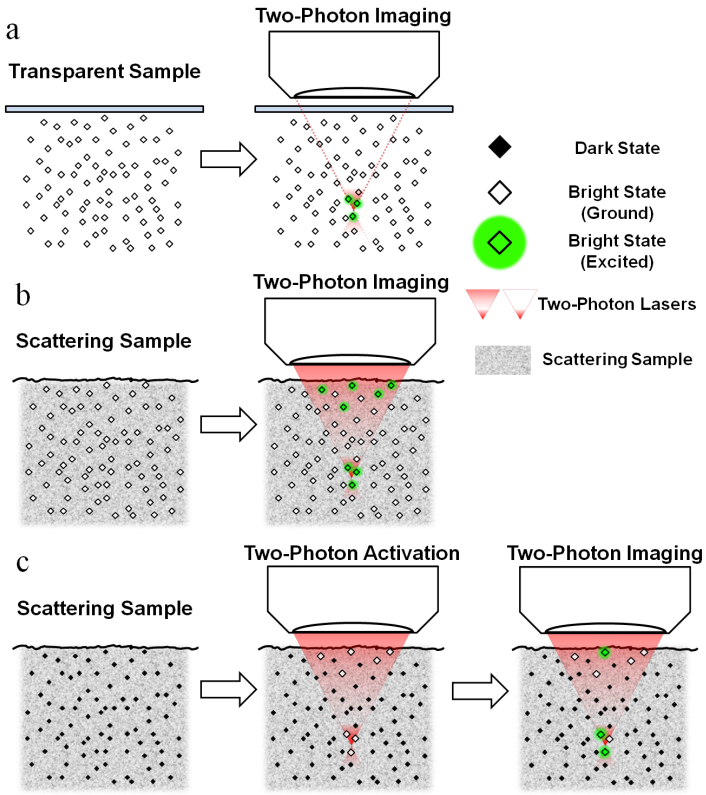

Fig. 5.3 Principle of multiphoton activation and imaging (MPAI). (a) When imaging transparent samples, fluorescence is only generated at the laser focus where the intensity is the highest. (b) When imaging deep into scattering samples, substantial laser intensities are distributed out of focus, generating background fluorescence that is comparable to or even stronger than the in-focus signal. (c) When imaging with PAFs which are originally in the dark state, the multiphoton activation will switch on a higher percentage of PAFs at focus than those out-of-focus. Such a spatial disparity of dark-bright transitions leads to a significantly decreased background fluorescence in the subsequent imaging.

5.2.4 Experimental demonstration using a caged organic dye.

Caged fluorescein, resorufin and rhodamine are the first developed small organic PAFs. They have been applied to study the assembly of tubulin, hydrodynamic flows and cell lineage during embryo development[23]. Here we use the caged fluorescein, which is commercially available, as a proof-of-principle. Fig. 5.4a shows the photo-uncaging reaction of caged fluorescein. The dark state can be activated to the bright state by

illuminating with UV light as shown by the absorption and fluorescence spectra and uncaging kinetics in Fig. 5.4b. For our two-photon application, laser pulses at 750 nm can both uncage the protective groups and image the bright state. We therefore only need one laser in this simultaneous mode, i.e., $I_a = I_i$. We again constructed "two-layer" samples (Fig. 5.5). The target object, a droplet of caged fluorescein solution, is placed on a glass coverslip, and a thick layer made of mixed scattering beads and caged fluorescein is inserted between the target and the objective. The control samples exhibit the same physical parameters except for the use of regular fluorescein in both the target droplet and the out-of-focus background layer.

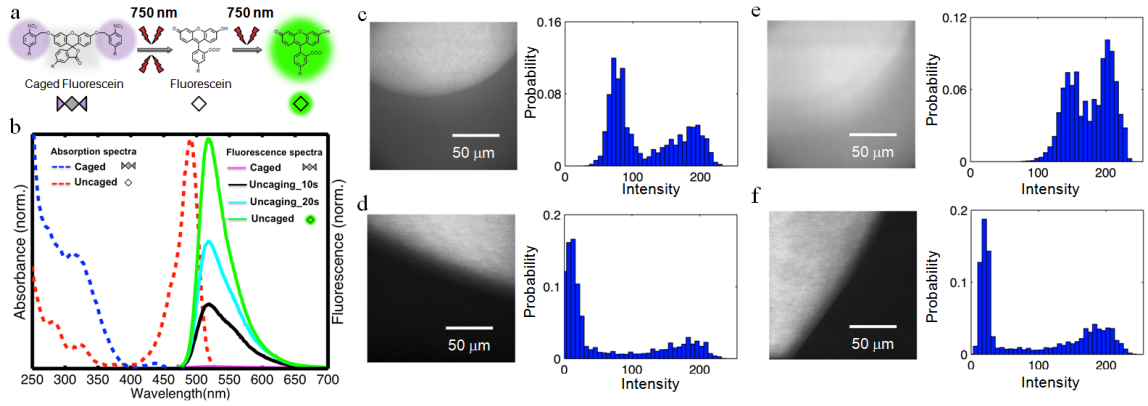

Fig. 5.4 Experimental demonstration of MPAI with caged fluorescein. (a) CMNB (5-carboxymethoxy-2-nitrobenzyl) caging groups of CMNB-caged fluorescein could be cleaved by a 750 nm pulsed laser, leading to the formation of fluorescein in the bright state, which could be excited by the same laser to emit fluorescence. (b) Absorption and fluorescence spectra of caged fluorescein and uncaged fluorescein, and the activation kinetics under UV illumination. A ~100-fold fluorescence enhancement is observed after a complete activation. (c-f) Imaging "two-layer" samples (Fig. S2) where the targets are 2 μL droplets of 1 mM dye solution and the background layers (120 μm thick) consist of scattering polystyrene beads (0.9 μm) and dye solution (1 mM for (c) and (d), 3 mM for (e) and (f)). Boundaries of liquid droplets divide the field of view so that the darker parts correspond to the background while the brighter parts represent the sum of the signal and the background. When the imaging depth-limit is reached for regular fluorescein in (c) with a *S*/*B* of about 1.2, a 20-times improvement is achieved for caged fluorescein in (d). With a

three folds more dyes in the background layer of (e) and (f), imaging contrast becomes extremely poor for regular fluorescein, while the caged fluorescein still offers a *S*/*B* of about 8.

Figure 5.4c-f show the comparison between $(S/B)_{regular}$ and $(S/B)_{PAFs}$ in our tissue phantoms labeled with dynamic fluorophores. Using the control sample, we first determined the proper concentrations of scattering and dye species in the background layer so that imaging regular fluorescein is approaching the fundamental imaging-depth limit with $(S/B)_{regular} \approx 1.2$ in Fig. 5.4c. We then measured the corresponding PAFs sample. To accommodate the relatively slow photo-activation of caged fluorescein, a long pixel dwell time of ~ 1.0 ms was used to obtain enough fluorescence signals, however this does not affect the signal-to-background ratio. The resulting $(S/B)_{PAFs}$ is found to be about 20 in Fig. 5.4d, proving a significant improvement of imaging contrast. Encouraged by this, we further elevated the background dye concentration by a factor of 3 for both control and PAFs samples in Fig. 5.4e and f. As expected, $(S/B)_{regular} \approx 1/3$ is now beyond what the depth limit permits. In contrast, the corresponding PAFs sample exhibits a remarkable $(S/B)_{PAFs} \sim 8$.

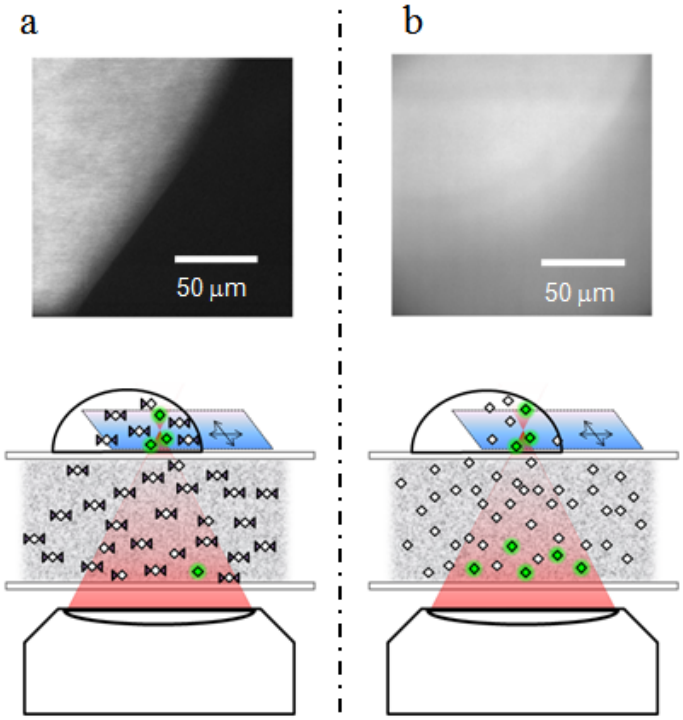

Fig. 5.5 The "two-layer" sample design in Fig. 5.4 (a): imaging with caged fluorescein (Fig. 5.4f). (b): imaging with regular fluorescein (Fig.5.4e). Images were taken across the boundaries of caged-fluorescein or regular fluorescein droplets on top of a layer of caged-fluorescein or regular fluorescein solution doped with scattering polystyrene beads.

5.2.5 Theoretical framework of MPAI using static PAFs.

If PAFs are rather static during the entire frame acquisition, we then need to consider the spatio-temporal accumulation of the activated fluorophore in out-of-focus background during the raster scanning. In this scenario, while η_S of the signal remains the same as in Eqs. (5.2)-(5.4), the effective activation time for η_B will be longer than the pixel dwell time, τ, by a factor of, $f(z)$, which scales with the z-dependent laser beam area. The result of static PAFs hence becomes

$$\left(\frac{S}{B}\right)_{PAFs} = \frac{\int_{V_{in}} \int_0^{\tau} C_S(r,z)\eta_S(r,z,t) I_i^2(r,z,t)\,\mathrm{d}t\,\mathrm{d}V}{\int_{V_{out}} \int_0^{\tau} C_B(r,z)\eta_B\left(r,z,f(z)\cdot\tau\right) I_i^2(r,z,t)\,\mathrm{d}t\,\mathrm{d}V} \tag{5.8}$$

Thus, due to the accumulation of the activated fluorophores during laser scanning, the out-of-focus background will be higher here compared to that from dynamic PAFs described in Eq. (5.4). In the condition of low photo-activation yield, we have the following approximation

$$\frac{\eta_S(r,z,\tau)}{\eta_B\left(r,z,f(z)\cdot\tau\right)} \approx \frac{I_a^2(r,z)\Big|_{V_{in}}}{f(z)\cdot I_a^2(r,z)\Big|_{V_{out}}} \approx \frac{\int_{in} I_a^2(r,z)\,\mathrm{d}r}{\int_{out} I_a^2(r,z)\,\mathrm{d}r} > 1 \tag{5.9}$$

From the earlier analysis of laser intensity distribution at the depth limit defined in Eq. (5.1), we have inferred that $\int_{in} I^2(r,z)\,\mathrm{d}r > \int_{out} I^2(r,z)\,\mathrm{d}r$ for all z layers. Consequently, the final activation yield will be higher at the focus than in the background. Therefore, the signal-to-background ratio using static PAFs is still higher in Eq. 5.8 than that with regular fluorophores in Eq. 5.1.

5.2.6 Experimental demonstration by a photo-activatable fluorescent protein.

PAFs also include several fluorescent proteins that can be genetically encoded and fused to other proteins of interest for *in vivo* imaging of cells and animals. Photoactivatable green fluorescent protein (pa-GFP) is the first member of this family of optical highlighters[24]. As shown in Fig. 5.6a, pa-GFP can be turned on from its initial dark state by two-photon activation in the 750~850 nm range, and the resulting bright state can be readily imaged in the 900~950 nm range[25].

We prepared tissue phantoms by embedding the fluorescent protein expressing *E. coli* cells in 3D agarose gel. The resulting sample is highly scattering due to the densely packed *E. coli* cells. The PAFs in this sample are considered static, as the cells are

stationary within the agarose gel. As clearly demonstrated in Fig. 5.6b-c, while the out-of-focus background is overwhelming for cells expressing regular GFP at a depth of 100 μm, MPAI of cells expressing pa-GFP at the same depth offers a satisfactory image contrast. Thus, we have experimentally demonstrated the ability of MAPI in extending the fundamental imaging-depth limit of two-photon fluorescence microscopy.

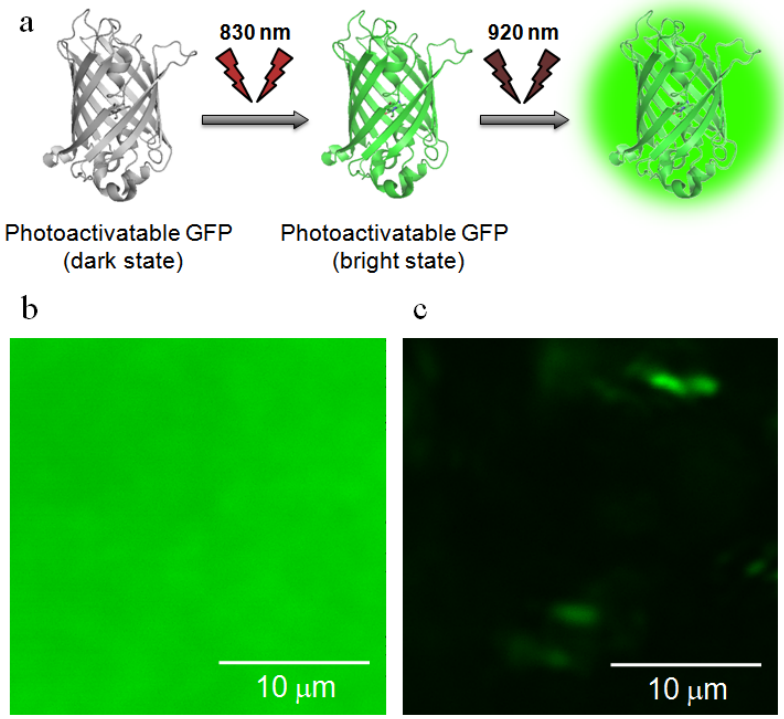

Fig. 5.6 Experimental demonstration of MPAI with pa-GFP. (a) pa-GFP could be activated by a pulsed laser at 830 nm to its bright state, which could be further excited by a 920 nm pulsed laser to emit fluorescence. Deep imaging comparison for 3D turbid samples made of *E. coli* cells expressing free regular GFP (b) or pa-GFP (c), embedded in 2% agarose gel. While the out-of-focus background is overwhelming when imaging *E. coli* expressing regular GFP at a 100 μm depth inside the gel, MPAI with pa-GFP at the same depth offers a satisfactory image contrast. *E. coli* cell densities were kept consistent between these samples.

5.3 Conclusion

To summarize, we have presented the principle of MPAI of PAFs in extending the fundamental imaging-depth limit of multiphoton fluorescence microscopy. This represents a novel strategy compared to the existing approaches that focus on reducing sample scattering. Theoretical framework has been provided to describe both the dynamic and static PAFs during image acquisition. Experimentally, we demonstrated MPAI on scattering tissue phantoms labeled with caged fluorescein (dynamic PAFs scenario) or pa-GFP (static PAFs scenario), which serves as an example of synthetic small-molecule and genetically encoded PAF, respectively.

The practical performance of MPAI can be potentially improved by using PAFs with better designed photophysical properties. First, two-photon photo-activation could be much faster for molecules with larger activation cross sections. For instance, caged coumarin has been shown to exhibit 100 times faster uncaging rate via substrate-assisted photolysis[26]. Second, after being photo-activated, many photochromic fluorophores can also be switched off either thermally or by light[27-29]. Such a switching-off property could re-set PAFs in the entire sample and hence allow repeated imaging on the same x-y plane or navigating through multiple layers.

It does not seem to be a mere coincidence that PAFs can play key roles for both breaking the diffraction-limited spatial resolution of fluorescence microscopy and extending the fundamental imaging-depth limit of multiphoton microscopy. In essence, the coarse spatial resolution and the superficial penetration depth are both rooted in the

difficulty of distinguishing identical molecules in space. By offering the additional disparity of (on-off) molecular quantum states, PAFs render the capability of circumventing both resolution and penetration limits.

5.4 Methods and materials.

Sample preparation. Fluorescent beads were purchased from Invitrogen (F8765: green/yellow 1.0 μm beads; F8859: green/yellow 4.0 μm beads). Fluorescein (Sigma 46960) and CMNB-Caged Carboxyfluorescein (Invitrogen C-20050) were prepared into 10 mM stock solution in DMSO before diluting to final concentrations. Intralipid (Sigma I141) or non-fluorescent polystyrene beads (Sigma CLB9) were used as the scattering species. "Two-layer" samples in Figs. 5.2 and 5.4 were prepared as follows: An imaging spacer with a 120 μm thickness (Sigma S7935) was pasted onto a piece of micro coverglass (VWR 48393-220). Inside the spacer, 5 μL of material serving as the scattering background was added. The background material was then sealed inside the spacer by another piece of micro coverglass on top, giving a sandwich-like background sample. Imaging targets (fluorescent beads or dye droplets) were placed on top of the glass sandwich before imaging. In bacteria imaging experiments, BL21 *E. coli* strains expressing pa-GFP (Addgene plasmid 11911) and Dronpa-3 (a regular GFP version for standard imaging, MBL International Corporation) were harvested by centrifugation, resuspended and embedded inside an imaging spacer using 2% agarose gel. *E. coli* densities of different samples were calibrated based on OD600 measurement to achieve the consistent scattering effect.

Fluorescence imaging. All the two-photon fluorescence images were taken on a Leica TCS SP5 MP inverted microscope equipped with a Mai Tai HP laser (690-1040 nm tunable emission) and a HCX PL APO CS 20X DRY microscope objective (N.A. 0.70). A non-descanned epi PMT detector placed directly behind the objective was used for fluorescence collection in combination with a 680/SP emission filter. Images were processed with LAS AF software unless otherwise stated. Images of fluorescent beads (Figs. 5.1 and 5.2) were taken under 750 nm with a pixel dwell time of ~2.4 μs. Images of caged-fluorescein-based samples (Fig. 5.4d and 5.4f) were taken under 750 nm (48mW) with a pixel dwell time of 977 μs to achieve effective uncaging. Images of *E. coli* expressing regular GFP (Fig. 5.6b) were taken under 920 nm (65mW) with a pixel dwell time of 98 μs. Images of *E. coli* expressing pa-GFP (Fig. 5.6c) were taken under 920 nm (65mW) after 3 frames of two-photon activation under 830 nm (95mW) with a pixel dwell time of 98 μs. Note that for tissue phantoms labeled with caged fluorescein or pa-GFP, due to the sample scattering, the actual laser power reached at the deep focal plane is much lower than the measured total power. All images were acquired with 512 by 512 pixels.

In the volume imaging experiments (Fig. 5.1), a final percentage of 1% agarose was mixed with the emulsion of 5% intralipid (Sigma I141) and 1.0 μm green/yellow beads (Invitrogen F8765) for fixation. The two data sets consist of 31 z- sections, respectively, taken at increments of 3 μm. Images were taken at 512 by 512 pixels with a pixel dwell time of 2.44 μs, using a 750 nm laser for excitations. Images were processed with ImageJ software (Volume Viewer plugin) to generate the volume image. In the bead imaging

experiments (Fig. 5.2), images were also taken at 512 by 512 pixels under 750 nm with a pixel dwell time of 2.44 μs.

For the spectra measurements of fluorescein and caged fluorescein (Fig. 5.4b), absorption and fluorescence spectra were taken at a concentration of 10 μM using Tecan Infinite 200 (for absorption measurements) and Fluorolog-3 spectrofluorometer (for fluorescence measurements). Fluorescence spectrum of fluorescein was measured using the excitation of 450 nm light (3 nm slit). Uncaging of caged fluorescein was carried out by the irradiation of 310 nm light (20 nm slit) using the lamp of the same spectrofluorometer.

For the activation-imaging experiments of fluorescein and caged fluorescein (Fig. 5.4c-f), suspension of non-fluorescent 0.9 μm polystyrene beads (Sigma CLB9) was sonicated and diluted (1:5) into 50% glycerol solution with fluorescein or caged fluorescein at a concentration of 1 mM or 3 mM to serve as the scattering background. Glycerol solutions were used to minimize evaporation of solvent during the imaging process. Acquired images were processed with Matlab to subtract the residual fluorescence from the sample. Intensity histograms were generated by Matlab.

5.5 References.

1. Hell, S.W. Far-field optical nanoscopy. *Science* **316**, 1153-1158 (2007).
2. Huang, B., Babcock, H. & Zhuang, X. Breaking the diffraction barrier: super-resolution imaging of cells. *Cell* **143**, 1047-1058 (2010).
3. Betzig, E. *et al.* Imaging intracellular fluorescent proteins at nanometer resolution. *Science* **313**, 1642-1645 (2006).

4. Denk, W., Strickler, J.H. & Webb, W.W. Two-photon laser scanning fluorescence microscopy. *Science* **248**, 73-76 (1990).
5. Zipfel, W.R., Williams, R.M. & Webb, W.W. Nonlinear magic: multiphoton microscopy in the biosciences. *Nat. Biotechnol.* **21**, 1369-1377 (2003).
6. Helmchen, F. & Denk, W. Deep tissue two-photon microscopy. *Nat. Methods*. **2**, 932-940 (2005).
7. Yuste, R. Ed. *Imaging: A laboratory manual.* Cold Spring Harbor Laboratory Press (2010).
8. Theer, P., Hasan, M.T. & Denk, W. Two-photon imaging to a depth of 1000 μm in living brains by use of a Ti:Al_2O_3 regenerative amplifier. *Opt. Lett.* **28**, 1022-1024 (2003).
9. Theer, P. & Denk, W. On the fundamental imaging-depth limit in two-photon microscopy. *J. Opt. Soc. Am. A-Opt. Image Sci. Vis.* **23**, 3139-3149 (2006).
10. Kobat, D., Horton, N.G. & Xu, C. In vivo two-photon microscopy to 1.6-mm depth in mouse cortex. *J. Biomed. Opt.* **16**, 106014 (2011).
11. Durr, N.J., Weisspfennig, C.T., Holfeld, B. A. & Ben-Yakar, A. Maximum imaging depth of two-photon autofluorescence microscopy in epithelial tissues. *J. Biomed. Opt.* **16**, 026008 (2011).
12. Ying, J., Liu, F. & Alfano, R.R. Spatial distribution of two-photon-excited fluorescence in scattering media. *Appl. Opt.* **38**, 224-229 (1999).
13. Ji, N., Milkie, D.E. & Betzig, E. Adaptive optics via pupil segmentation for high-resolution imaging in biological tissues. *Nat. Methods.* **7**, 141-147 (2009).
14. Rueckel, M., Mack-Bucher, J. A. & Denk, W. Adaptive wavefront correction in two-photon microscopy using coherence-gated wavefront sensing. *Proc. Natl. Acad. Sci. USA* **103**, 17137-17142 (2006).
15. Kobat, D. *et al.* Deep tissue multiphoton microscopy using longer wavelength excitation. *Opt. Express* **17**, 13354-13364 (2009).
16. Hama, H. *et al.* Scale: a chemical approach for fluorescence imaging and reconstruction of transparent mouse brain. *Nat. Neurosci.* **14**, 1481-1488 (2011).

17. Leray, A., Lillis, K. & Mertz, J. Enhanced background rejection in thick tissue with differential-aberration two-photon microscopy. *Biophys. J.* **94**, 1449-1458 (2008).
18. Fernández-Suárez, M. & Ting, A.Y. Fluorescent probes for super-resolution imaging in living cells. *Nat. Rev. Mol. Cell Biol.* **9**, 929-943 (2008).
19. Lippincott-Schwartz, J. & Patterson, G.H. Photoactivatable fluorescent proteins for diffraction-limited and super-resolution imaging. *Trends Cell Biol.* **19**, 555-565 (2009).
20. Heilemann, M., Dedecker, P., Hofkens, J. & Sauer, M. Photoswitches: Key molecules for subdiffraction-resolution fluorescence imaging and molecular quantification. *Laser & Photon. Rev.* **3**, 180-202 (2009).
21. Lee, H.-l. D. *et al.* Superresolution imaging of targeted proteins in fixed and living cells using photoactivatable organic fluorophores. *J. Am. Chem. Soc.* **132**, 15099-15101 (2010).
22. Kleinfeld, D., Mitra, P.P., Helmchen, F. & Denk, W. Fluctuations and stimulus-induced changes in blood flow observed in individual capillaries in layers 2 through 4 of rat neocortex. *Proc. Natl. Acad. Sci. USA* **95**, 15741-15746 (1998).
23. Mitchison, T.J., Sawin, K.E., Theriot, J.A., Gee, K. & Mallavarapu, A. Caged Fluorescent Probes. *Methods Enzymol.* **291**, 63-78 (1998).
24. Patterson, G.H. & Lippincott-Schwartz, J. A photoactivatable GFP for selective photolabeling of proteins and cells. *Science* **297**, 1873-1877 (2002).
25. Schneider, M., Barozzi, S., Testa, I., Faretta, M. & Diaspro, A. Two-photon activation and excitation properties of PA-GFP in the 720-920-nm region. *Biophys. J.* **89**, 1346-1352 (2005).
26. Zhao, Y. *et al.* New caged coumarin fluorophores with extraordinary uncaging cross sections suitable for biological imaging applications. *J. Am. Chem. Soc.* **126**, 4653-4663 (2004).
27. Ando, R., Mizuno, H. & Miyawaki, A. Regulated fast nucleocytoplasmic shuttling observed by reversible protein highlighting. *Science* **306**, 1370-1373 (2004).
28. Fölling, J. *et al.* Photochromic rhodamines provide nanoscopy with optical sectioning. *Angew. Chem. Int. Ed.* **46**, 6266-6270 (2007).

29. Zhu, M.-Q. *et al.* Reversible Two-Photon Photoswitching and Two-Photon Imaging of Immunofunctionalized Nanoparticles Targeted to Cancer Cells. *J. Am. Chem. Soc.* **133,** 365-372 (2011).

Chapter 6

Extending the fundamental imaging depth limit with stimulated emission reduced fluorescence microscopy and focal saturation microscopy.

Partial contents of this chapter has been published in:

L. Wei, Z. Chen and W. Min. "Stimulated emission reduced fluorescence microscopy: a concept for extending the fundamental depth limit of two-photon fluorescence imaging", *Biomed. Opt. Express* 3, 1465 (2012).

Abstract

Two-photon fluorescence microscopy has become an indispensable tool for imaging scattering biological samples by detecting scattered fluorescence photons generated from a spatially confined excitation volume. However, this optical sectioning capability breaks down eventually when imaging much deeper, as the out-of-focus fluorescence gradually overwhelms the in-focal signal in the scattering samples. The resulting loss of image contrast defines a fundamental imaging-depth limit, which cannot be overcome by increasing excitation efficiency. Herein we first propose to extend this depth limit by performing stimulated emission reduced fluorescence microscopy (SERF) in which the two-photon excited fluorescence at the focus is preferentially switched on and off by a modulated and focused laser beam that is capable of inducing stimulated emission of the fluorophores from the excited states. The resulting image, constructed from the reduced fluorescence signal, is found to exhibit a significantly improved signal-to-background contrast owing to its overall third-order nonlinear dependence on the incident laser intensity. We demonstrate this new concept by both analytical theory and numerical simulations. For brain tissues, SERF is expected to extend the imaging depth limit of two-photon fluorescence microscopy by a factor of more than 1.8. In addition, we also exploit the saturated two-photon excitation to extend this depth limit. When the excitation laser is sinusoidally modulated at a fundamental frequency, the demodulated two-photon excited fluorescence at its third harmonic frequency is found to scale with the fourth power of excitation intensity in the weak saturation region. Such an increased nonlinearity is simulated to offer a 2.3 times depth extension over the regular two-photon microscopy.

6.1 Introduction.

Compared to MPAI in Chapter 5 that utilizes a special class of fluorophores, the photoactivatable fluorophores, to extend the imaging depth in the optical microscopy, this chapter seeks to address such an imaging depth extension by the adoption of two physical principles: stimulated emission and focal saturation. Both principles are demonstrated with analytical theory and numerical simulations.

As a brief summary (details illustrated in Chapter 5), the fundamental imaging depth limit for optical microscopy is restricted by the signal-to-background ration but not the laser power, and is defined as[1-4]:

$$\left(\frac{S}{B}\right)_{2P} = \frac{\int_{V_{in}} \int_0^{\tau} C_S(r,z) I^2(r,z,t)\,\mathrm{d}t\,\mathrm{d}V}{\int_{V_{out}} \int_0^{\tau} C_B(r,z) I^2(r,z,t)\,\mathrm{d}t\,\mathrm{d}V} = 1 \tag{6.1}$$

Where V_{in} is the focal volume, V_{out} is the total sample volume along the beam path but excluding the focal volume, r is the distance from the optical axis, z is the axial distance from the tissue surface, C is the local fluorophore concentration, I is the laser intensity, and τ is the pixel dwell time during the imaging. We assume equal fluorescence collection efficiency between signal and background at the large-area detector. As an analogy, the limited imaging-depth here is reminiscent to the scenario of wide-field fluorescence microscopy, which lacks background rejection. For mouse brain tissues expressing GFP, the corresponding depth limit is about 1 mm^2. Although this depth is impressive compared with other high-resolution techniques, it still covers only a very small fraction of the mammalian brain.

6.2 The stimulated emission reduced fluorescence microscopy (SERF) for the imaging depth extension.

6.2.1 Introduction.

In this section, we propose a novel spectroscopy-based concept, Stimulated Emission Reduced Fluorescence (SERF) Microscopy, to extend the fundamental depth limit of 2P fluorescence imaging. Stimulated emission (S.E.) has been the key switching mechanism in STED microscopy for breaking the diffraction-limited spatial resolution[5], and recently was employed as a new contrast mechanism for imaging non-fluorescent chromophores with superb sensitivity[6, 7]. In SERF, we adopt a scheme that combines a continuous wave (CW) S.E. beam collinearly with 2P beam and detects the reduced fluorescence signal (Fig. 6.1a). By choosing a S.E. beam with proper wavelength and intensity to preferentially switch off the fluorescence signal from the focus while keeping most of the out-of-focus background fluorescence less affected, SERF will promote the image contrast of in-focus signal over out-of-focus background, effectively extending the fundamental imaging depth limit. Both analytical and numerical results will be presented to support our proposal.

6.2.2 Theory.

Laser intensity distribution inside scattering samples. We first analyze how the laser intensity is distributed within the scattering sample when the depth limit is reached for regular 2P imaging as in Chapter 5. Fluorophores are normally distributed throughout the 3D volume of the sample. Thus, the number of out-of-focus fluorophores is almost always orders-of-magnitude larger than that of the in-focus ones:

$$\frac{\int_{V_{in}} C_S(r,z)\mathrm{d}V}{\int_{V_{out}} C_B(r,z)\mathrm{d}V} << 1 \tag{6.2}$$

The comparison between Eq. 6.1 and Eq. 6.2 indicates that, despite of the scattering loss, $I^2(r,z)$ at the focus will be much larger than its out-of-focus counterpart when the depth limit is reached as defined in Eq. 6.1. In a simplified condition with a homogeneous fluorophore distribution, i.e., $C_B(r,z) = C_S(r,z)$, $\int_V \int_0^\tau I^2(r,z,t)\mathrm{d}t\,\mathrm{d}V$ will be equal between the background and the signal. Consequently, the integral of $I^2(r,z)$ over a subset of the out-of-focus volume will also be smaller than that over the focus.

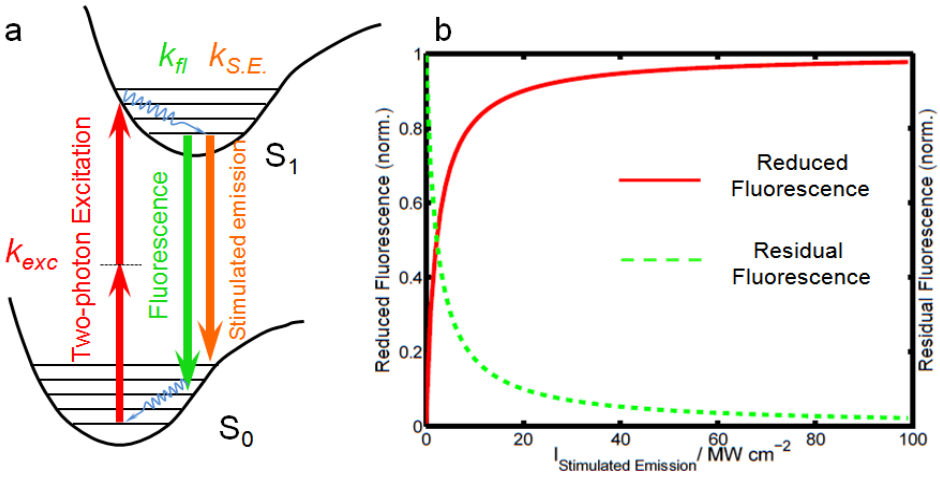

Fig. 6.1 Diagram principle for the stimulated emission reduced fluorescence (SERF) microscopy. (a) A simplified Jablonski diagram of a typical fluorophore under two-photon excitation and one-photon stimulated emission. (b) The intensity dependence of reduced fluorescence and residual fluorescence on the S.E. beam. $\tau_{fl} = 10ns$, $\lambda_{S.E.} = 750nm$, $\sigma_{S.E.} = 10^{-17} cm^2$.

Reduced fluorescence in the presence of stimulated emission. Additionally, we quantify the reduced fluorescence effect when combining a CW S.E. beam collinearly with a 2P excitation beam and focusing them into a common focal spot.

Assuming no fluorescence saturation or photobleaching, below we analyze the following two photophysical schemes of 2P fluorescence with and without the S.E. beam.

In the absence of the S.E. beam:
$$\begin{aligned} S_0 + 2h\nu_{exc} &\xrightarrow{k_{exc}} S_1 \\ S_1 &\xrightarrow{k_{fl}} S_0 + h\nu_{fl} \end{aligned}$$

In the presence of the S.E. beam:
$$\begin{aligned} & S_0 + 2h\nu_{exc} \xrightarrow{k_{exc}} S_1 \\ & \begin{cases} S_1 \xrightarrow{k_{fl}} S_{0_1} + h\nu_{fl} \\ S_1 + h\nu_{S.E.} \xrightarrow{k_{S.E.}} S_{0_2} + 2h\nu_{S.E.} \end{cases} \end{aligned}$$

where S_0 and S_1 represent the ground and the excited state, respectively, $h\nu$ is the energy of a single photon, $k_{exc} = \sigma_{exc}(I_{exc}\lambda_{exc}/hc)^2$ is the 2P excitation rate, σ_{exc} is the 2P absorption cross-section of the molecule at λ_{exc}, I_{exc} is the intensity of the 2P excitation beam (in W/cm^2). The fluorescence emission rate k_{fl} is a constant for a given fluorophore: $k_{fl} = 1/\tau_{fl}$, where τ_{fl} is the fluorescence lifetime. In the case of S.E., $k_{S.E.} = \sigma_{S.E.} I_{S.E.}\lambda_{S.E.}/hc$ is the S.E. rate where $\sigma_{S.E.}$ is the S.E. cross-section of the molecule at $\lambda_{S.E.}$. Thus we can calculate the 2P fluorescence emission rate of a single fluorescent molecule (R) and its counterpart in the presence of S.E. attenuation (R'):

$$R = f_{rep} k_{exc} \tau_{exc} \eta \tag{6.3}$$

$$R' = f_{rep} k_{exc} \tau_{exc} \eta' = f_{rep} k_{exc} \tau_{exc} \eta \frac{k_{fl}}{k_{fl} + k_{S.E.}} \tag{6.4}$$

Where f_{rep} is repetition rate of the excitation pulse train, τ_{exc} is the pulse width (~100 *fs* for a typical 2P laser), η is the fluorescence quantum yield, and η' is effective fluorescence quantum yield in the presence of the S.E. beam. Subtracting Eq. 6.4 from Eq. 6.3, we obtain the reduced fluorescence rate (defined as R_{SERF}) as:

$$R_{SERF} \equiv R - R' = f_{rep} k_{exc} \tau_{exc} \eta \frac{k_{S.E.}}{k_{fl} + k_{S.E.}} \tag{6.5}$$

Different from the commonly known STED signal, in which the residual fluorescence decreases with the increasing S.E. beam intensity, R_{SERF} increases with the intensity of S.E. beam (Fig. 6.1b) due to its differential nature.

Imaging contrast of SERF. Taking R_{SERF} in Eq. 6.5 back into Eq. 6.1, we get the image contrast $(S/B)_{SERF}$ of SERF in the differential imaging mode,

$$\left(\frac{S}{B}\right)_{SERF} = \frac{\int_{V_{in}} \int_0^\tau C_S(r,z) \dfrac{\alpha I_{S.E.}(r,z)}{1+\alpha I_{S.E.}(r,z)} I_{exc}^2(r,z,t)\,\mathrm{d}t\,\mathrm{d}V}{\int_{V_{out}} \int_0^\tau C_B(r,z) \dfrac{\alpha I_{S.E.}(r,z)}{1+\alpha I_{S.E.}(r,z)} I_{exc}^2(r,z,t)\,\mathrm{d}t\,\mathrm{d}V} \tag{6.6}$$

where $\alpha \equiv \tau_{fl} \sigma_{S.E.} \lambda_{S.E.} / hc$. For many red fluorophores, $\lambda_{S.E.}$ and λ_{exc} can be chosen to be close or even identical to each other. Consequently, 2P and S.E. beams would both lie within the tissue transparency window (650~1300 nm) and experience similar attenuation effects inside scattering samples. As analyzed earlier, $I_{exc}(r,z,t)$ at the focus is much more intense than its out-of-focus counterpart when reaching the depth limit of regular 2P imaging. Consequently, $I_{S.E.}(r,z)$ and $\alpha I_{S.E.}(r,z)/[1+\alpha I_{S.E.}(r,z)]$ at the focus should be

much higher than their out-of-focus counterparts as well. Therefore, by introducing a new factor of $\alpha I_{S.E.}(r,z)/[1+\alpha I_{S.E.}(r,z)]$, which makes the intensity ratio between the in focus and out of focus part even larger, we can preferentially switch off the molecules in the focus but not in the background, and claim an improved signal-to-background contrast at the original 2P imaging depth limit with SERF (i. e., $(S/B)_{SERF} > (S/B)_{2P} = 1$).

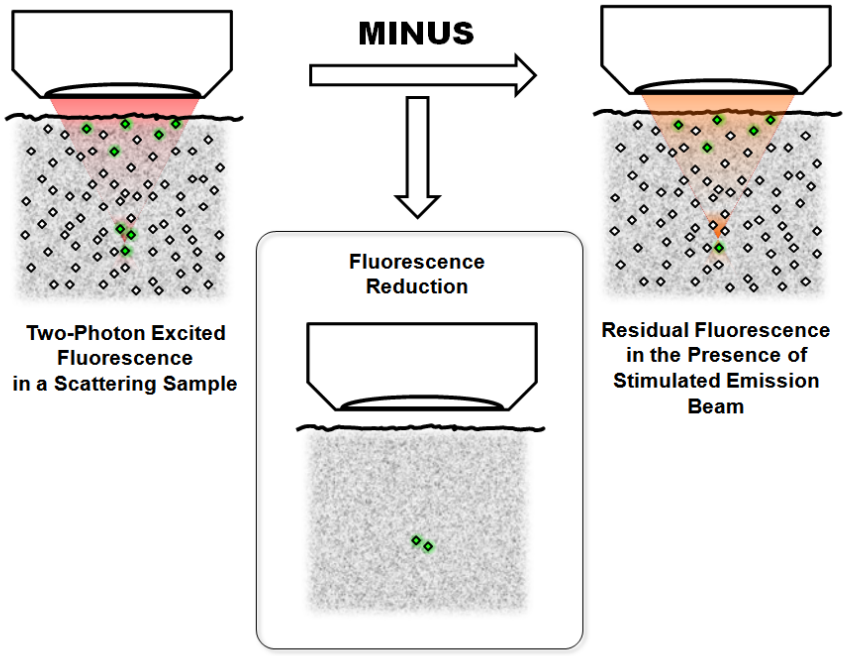

Fig. 6.2 Cartoon representation of the SERF principle. Stimulated emission beam preferentially reduces the in-focus fluorescence signal over out-of-focus background fluorescence due to its intensity distribution disparity. The resulting differential signal would be mainly generated from the laser focus. Consequently, images reconstructed with the differential signal are expected to exhibit a higher contrast when comparing with original two-photon fluorescence image.

A cartoon in Fig. 6.2 visually presents the principle of SERF. By subtracting the residual 2P fluorescence signal (in the presence of S.E. beam) from the original 2P fluorescence signal (without the S.E. beam) at each point, reduced fluorescence signal is preferentially generated at focal point, which will enhance the image contrast.

Imaging contrast dependence of S.E. intensity $I_{S.E.}$. We now address how the image contrast of SERF depends on the applied S.E. beam intensity $I_{S.E.}$. When $I_{S.E.}$ is very large, it will lead to $\alpha I_{S.E.}(r,z)/[1+\alpha I_{S.E.}(r,z)] \sim 1$ in Eq. (6.6), which results in $(S/B)_{SEFR} \sim (S/B)_{2P} = 1$. This is so because the switching-off effect becomes unbiased for fluorophores in the focus and at background with no further contrast improvement being achieved. On the other hand, when the reduced fluorescence is in the linear (non-saturating) condition, more specifically, when $\alpha I_{S.E.}(r,z) < 1$ and the reduced fluorescence is beyond the shot noise, $(S/B)_{SERF}$ becomes

$$\left(\frac{S}{B}\right)_{SERF} \approx \frac{\int_{V_{in}} \int_0^\tau C_S(r,z) I_{S.E.}(r,z) I_{exc}^2(r,z,t)\,\mathrm{d}t\,\mathrm{d}V}{\int_{V_{out}} \int_0^\tau C_B(r,z) I_{S.E.}(r,z) I_{exc}^2(r,z,t)\,\mathrm{d}t\,\mathrm{d}V} > 1 \tag{6.7}$$

Eq. (6.7) directly reveals the physical picture underlying the SERF method: when operating above the shot noise of both the signal and the background with long enough signal acquisition time, SERF transforms the originally 2P non-linear process into an overall three-photon process by adding a S.E. laser beam instead of another virtual state. The ascending of this high-order nonlinearity improves the S/B ratio thereby improving the contrast and extending the imaging depth into scattering samples.

6.2.3 Experimental designs.

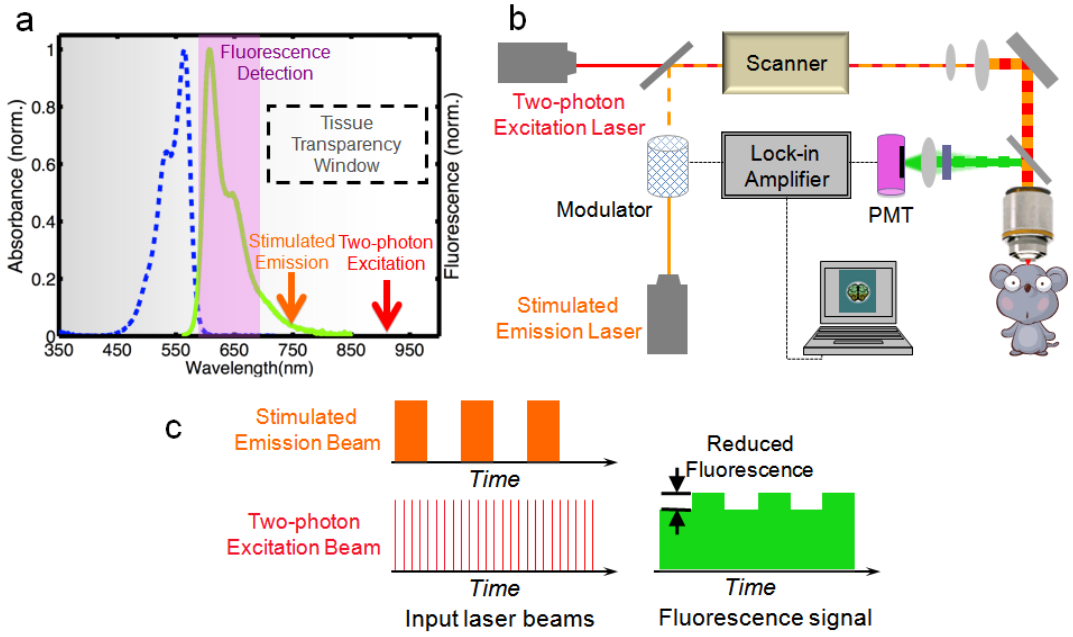

Fig. 6.3 Proposed experimental design of SERF. (a) Absorption and fluorescence spectrum of a red emission dye candidate for SERF. Both the stimulated emission and the 2-photon excitation wavelength are in the tissue transparency window for *in vivo* imaging. (b) SERF setup. In addition to a standard two-photon fluorescence microscope, a modulated stimulated emission beam is combined collinearly with the two-photon excitation beam. Reduced fluorescence at each pixel is measured by a lock-in amplifier. (c) Modulation transfer scheme of SERF. The stimulated emission beam is modulated at a high frequency (>MHz), which accounts for the reduced fluorescence modulated at the same frequency after interacting with fluorophores.

SERF fluorophores. Generally speaking, all fluorophores studied with STED microscopy can be used in SERF. Fluorophores having high 2P absorption cross-section, high brightness, broad and red-shifted emission spectra with a reasonably large Stokes shift are particularly suitable. Fig. 6.3a shows the absorption and emission spectra for an applicable red-emitting fluorophore, overlaid with the 2P excitation wavelength, S.E. wavelength and the spectral window for fluorescence collection. It has been already shown[8] that fluorophores excited via 2P processes can be forced back to the ground state

via one-photon STED in the near IR region, which supports our SERF design. It is worth stressing that the chosen wavelengths of S.E. beam and 2P excitation beam would be close to each other and both within tissue transparency window, making them behave similarly in terms of the scattering effect.

SERF microscope setup. Figure 6.3b shows the proposed SERF experiment setup. A 2P fluorescence microscope is equipped with a widely tunable pulsed laser and a non-descanned photomultiplier tube (PMT) detector closely attached to the objective to maximize the collection efficiency. Collinearly combined with the 2P laser beam, a CW S.E. laser beam is intensity modulated by a modulator at a high frequency (~5 MHz). The reduced fluorescence signal induced at the modulation frequency will be picked out by a lock-in amplifier connected after the PMT. The implementation of high frequency modulation and demodulation technique will be helpful for removing slow laser intensity noise as in other modulation transfer techniques[7]. Hence, we only need to consider the shot noise for SERF. The designed pulse train of 2P beam, CW S.E. beam and the resulting reduced fluorescence signal are illustrated in Fig. 6.3c. According to Fig. 6.1b, we design that the S.E. beam intensity is about 5~10 MW/cm^2 at focus to reduce the in-focus fluorescence by ~50% (which is just across the linear range), so that the reduced fluorescence signal won't be saturated through the sample volume to sacrifice the S/B.

6.2.4 Numerical simulation.

Equation (6.7) has proven that, in a non-saturating condition of S.E., SERF can attain $(S/B)_{SERF} > (S/B)_{2P} = 1$ by imaging the reduced fluorescence at the imaging-depth

limit of the regular 2P microscopy defined in Eq. (6.1). Here we evaluate the advantage of SERF in deep tissue imaging by numerical simulation using Matlab.

Available laser power inside scattering sample. For a propagating Gaussian beam, the z-dependent beam area, $A(z)$ follows:

$$A(z) \propto 1 + \left[\left(z - z_{focal} \right) / z_R \right]^2 \tag{6.8}$$

where $z_R = \pi \omega_0^2 / \lambda$ is the Rayleigh range, ω_0 is the beam waist, and z_{focal} denotes the focal depth below the sample surface ($z = 0$). We adopt $z_R = 0.5$ μm for a typical microscope objective. When focusing the 2P beam and S.E. beam deep into the scattering sample, the ballistic part of the Gaussian beam follows a Lambert-Beer-like exponential decline with imaging depth[9]. For the sake of performing analytical treatment, only the ballistic light is considered for samples whose anisotropy factors are low or moderate[1]. The area-integrated light power at certain z depth below surface thus can be described as

$$P_{ballistic}(z) = P_0 e^{-z/L_s} \tag{6.9}$$

where P_0 is the light power at sample surface, and L_s is the mean free path length describing the scattering strength. For example, $L_s \approx 200$ μm for brain tissues in the near IR region[9].

The imaging depth limit of regular two-photon microscopy. Assuming uniformly fluorophore-stained sample and uniformly distributed laser intensity for each z layer, we can integrate $\mathrm{d}t$, $\mathrm{d}r$ first in Eq. 6.1 for regular 2P imaging case:

$$\left(\frac{S}{B}\right)_{2P} \approx \frac{\int_{z_{in}}^{} \int_{0}^{r(z)} I_{ballistic}^2(r,z)\,dr\,dz}{\int_{z_{out}}^{} \int_{0}^{r(z)} I_{ballistic}^2(r,z)\,dr\,dz} \approx \frac{\int_{z_{in}}^{} [(\frac{P_{ballistic}(z)}{A(z)})^2 A(z)]dz}{\int_{z_{out}}^{} [(\frac{P_{ballistic}(z)}{A(z)})^2 A(z)]dz} \tag{6.10}$$

By defining $Q(z)_{2P} \equiv [P_{ballistic}(z)/A(z)]^2 A(z)$ and plugging in $A(z)$ and $P_{ballistic}(z)$ in Eqs. 6.8 and 6.9, we have

$$Q(z)_{2P} \propto \frac{\exp(-2z/L_s)}{1+\left[\left(z-z_{focal}\right)/z_R\right]^2} \tag{6.11}$$

To find out the corresponding z_{focal} limit that achieves $S/B=1$, we use the function "quadgk" in Matlab adopting Gauss–Kronrod quadrature formula, which has a relative error tolerance as 1.0e-6, to numerically integrate both the fluorescence signal around focus and out of the focus as follows:

$$\left(\frac{S}{B}\right)_{2P} \approx \frac{\int_{z_{focal}-\varepsilon}^{z_{focal}+\varepsilon} Q(z)_{2P}\,dz}{\int_{0}^{z_{focal}-\varepsilon} Q(z)_{2P}\,dz} = 1 \tag{6.12}$$

As shown in Fig. 6.4a, by reasonably assigning ε=1 μm, which is about two times of full width half maximum (FWHM) of the signal peak and whose actual value is not very sensitive, the numerical integration shows that the imaging-depth limit for regular 2P imaging is reached when $z_{focal}=1023\,\mu m$. This result is in fact very close to the experimentally measured value of 1 mm for brain tissues[2].

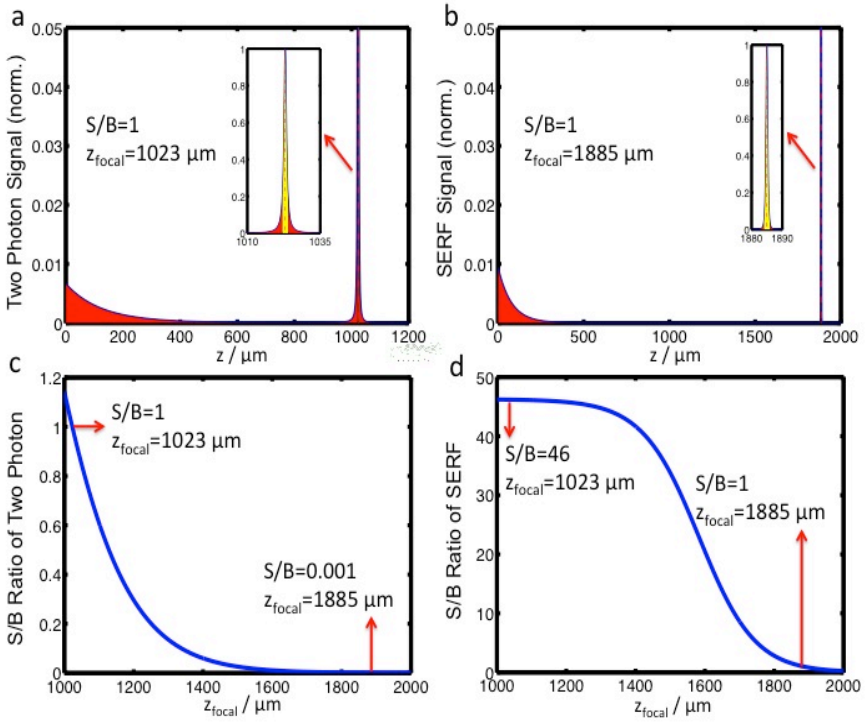

Fig. 6.4 Comparison of the fundamental imaging-depth limit between the regular two-photon imaging and SERF. (a) Using the typical parameters described in the text, the fundamental depth limit for two-photon imaging is 1023 μm at which $(S/B)_{2P}=1$ The yellow part beneath the curve is the integrated in-focus signal with a width of 2 μm, the red part with the z less than focus is the integrated out-of-focus background. Signal curve shown here has been normalized to the peak value of the signal. (b) The new depth limit for SERF is determined in a similar way, and is found to be 1885 μm when $(S/B)_{SERF}=1$, extending the depth by more than 1.8 times. (c) The dependence of $(S/B)_{2P}$ as a function of the focal depth z_{focal} between 1000 μm-2000 μm. At the SERF extended depth limit of 1885 μm, $(S/B)_{2P}$ is only 0.001. (d) On the contrary, when at the regular 2P depth limit of 1023 μm, $(S/B)_{SERF}$ is 46, which is much higher than the corresponding $(S/B)_{2P}=1$ at this focal depth.

S/B improvement and depth extension of SERF. It has been shown in Eq. 6.7 that SERF method is an overall three-photon non-linear process. Again, by assuming uniformly stained sample and uniformly distributed laser intensity in each z layer, we can modify Eq. 6.7 into:

$$\left(\frac{S}{B}\right)_{SERF} \approx \frac{\int_{z_{in}}\int_{0}^{r(z)} I_{ballistic}^{3}(r,z)\,dr\,dz}{\int_{z_{out}}\int_{0}^{r(z)} I_{ballistic}^{3}(r,z)\,dr\,dz} \approx \frac{\int_{z_{in}}[(\frac{P_{ballistic}(z)}{A(z)})^{3}A(z)]dz}{\int_{z_{out}}[(\frac{P_{ballistic}(z)}{A(z)})^{3}A(z)]dz} \tag{6.13}$$

By defining $Q(z)_{SERF} \equiv \left[P_{ballistic}(z)/A(z)\right]^{3} A(z)$, we have

$$Q(z)_{SERF} \propto \frac{\exp(-3z/L_s)}{\left(1+\left[(z-z_{focal})/z_R\right]^2\right)^2} \tag{6.14}$$

Similar numerical integration can be done for SERF as in the 2P imaging described in Eq. 6.12. Figure 6.4b shows that, by using SERF, $(S/B)_{SERF}=1$ is reached at a new depth limit of $z_{focal}=1885\,\mu m$. This effectively extends the original depth limit of $z_{focal}=1023\,\mu m$ of regular 2P imaging by more than 1.8 times. A more systematical study in Fig. 6.4c-d shows how the image contrast diminishes with the increasing imaging depth for both regular 2P imaging and SERF. SERF can achieve a 46 times of S/B contrast improvement when imaging at regular 2P depth limit of $z_{focal}=1023\,\mu m$. Note that we assume a long enough integration time here so that the shot noise can be neglected. As a reference, regular 2P imaging can only exhibit $S/B=0.001$ at the corresponding SERF depth limit of $z_{focal}=1885\,\mu m$. Even though here we only analyze

samples with low or moderate anisotropy factors, similar qualitative conclusion is expected for samples with near-unity anisotropy factor.

6.2.5 Discussion

It is imaginable to extend the depth limit of 2P microscopy by detecting three-photon (or four-photon) excited fluorescence signal. However, this seemingly viable approach is not practically attractive for bio-imaging, because (1) the simultaneous three-photon (or four-photon) absorption via more virtual states is an extremely improbable event: the transition amplitude is determined by the fifth (or seventh) order nonlinear molecular polarizability, and (2) the laser excitation wavelength for the classic GFP, YFP and RFP needs to be longer than 1400 nm, which lies outside the tissue transparency window (650~1300 nm) of most biological tissues. In contrast, SERF works through the real excited state of the fluorophore and all the involved wavelengths are within the tissue transparency window.

Although the current SERF setup employs a separate CW laser beam for S.E., one might be able to perform single wavelength experiment with the proper fluorophores (single-wavelength STED has been recently demonstrated on ATTO647N[10]). In this case, the 2P excitation wavelength lies within the fluorescence emission spectrum of the fluorophores. Experimentally, the output of a femtosecond pulsed laser is spitted into two arms, and one of the pulse trains is stretched into long pulses to act as the CW beam for S.E..

Finally, it is highly constructive to compare the technical aspects of SERF with STED microscopy[11], as both techniques are harnessing the fluorescence quenching process under S.E.. First, STED aims to break the spatial resolution limit while SERF is designed to extend the penetration depth. Second, the S.E. beam in STED is spatially shaped while the S.E. beam in SERF is being temporally modulated. Third, STED measures the residual fluorescence signal in the focus while SERF measures the difference between the original and residual fluorescence signals. Finally, STED works best in the fluorescence depletion region while SERF has to work in the non-saturating region in order to perform deep imaging. It is worth pointing out that, while SERF can improve the imaging depth, it should also be able to enhance the spatial resolution as implied in a recent report using high-order nonlinearity[12].

6.2.6 Conclusion.

In summary, a new fluorescence microscopy, SERF, is proposed to extend the fundamental depth limit of 2P imaging. This concept is radically different from the existing strategies that focus on ways to reduce scattering loss of the incident light. Technically, SERF is rather straightforward, as only a near IR CW laser beam (and the associated modulation electronics) is needed to be incorporated onto a standard 2P fluorescence microscope. We demonstrated, both analytically and numerically, the advantage of SERF method in terms of acquiring high-contrast images deep inside scattering samples. In particular, a 1.8-times deeper imaging depth is expected for scattering samples such as brain tissues.

6.3 Focal saturation and harmonic demodulation microscopy for the imaging depth extension.

6.3.1 Theoretical analysis and analytical simulation.

In this section, we seek for a new source of higher-order nonlinearity. Saturated excitation has been widely adopted to improve the spatial resolution due to the associated nonlinearity[13-18], for example, in saturated excitation microscopy (SAX)[13, 14] . Here we harness its role in depth extension. By modulating the 2P excitation laser intensity at a fundamental frequency ω and extracting the third harmonic demodulated fluorescence at 3ω, a more localized contrast that scales with the fourth power of the excitation intensity is created. Such extra nonlinearity is found to extend the fundamental depth limit of 2P microscopy by a factor of 2.3.

We now discuss the proposed method of detecting harmonic demodulated 2P fluorescence under weak excitation saturation. As shown in Fig. 6.5a, only a laser intensity modulator and a lock-in amplifier are required to add onto a standard 2P microscope. Upon intensity modulation at a fundamental frequency ω (~MHz which is fast enough for point scanning but still slower than the pulse repetition), the average 2P laser intensity could be expressed as

$$I_{2P,ave}(t) = \langle I_{2P,ave} \rangle (1 + \alpha \cos(\omega t)) \tag{6.15}$$

where $< I_{2P,ave} >$ is its time-averaged value, and α is the modulation depth (we assume α=1). With illumination by a train of 2P laser pulses, the excitation rate constant within the short laser pulses is related to $I_{2P,ave}(t)$ through

$$k_{exc,2P}(t) = \sigma_{2P}\left(\frac{I_{2P,avg}(t)\lambda_{2P}}{f_{rep}\delta_{pulse}hc}\right)^2 \tag{6.16}$$

where σ_{2P} is the two-photon absorption cross section (GM) of the fuorophore at wavelength λ_{2P}, f_{rep} is the repetition rate (~80 MHz), and δ_{pulse} is the pulse width (~100 *fs*).

Under repetitive pulsed excitation whose pulse spacing (~13ns) is relatively long compared to the fluorescence lifetime (~ns), which is then much longer than the pulse width, the fluorescence saturation is mainly due to the ground state depletion during the course of each pulse. Quantitatively, the probability of the fluorophore being excited to the excited state after each laser pulse is determined by the following first-order kinetics

$$P(t) = 1 - \exp\left(-k_{exc,2P}(t)\delta_{pulse}\right) \tag{6.17}$$

Note that there will be no excited-state molecules decaying back to the ground state within the short duration of excitation pulses.

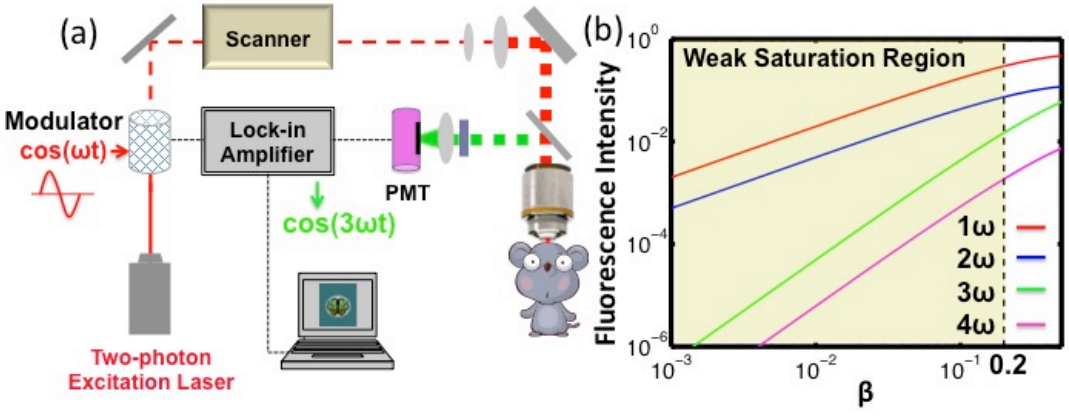

Fig. 6.5 Setup scheme and principle of focal saturation microscopy. (a) Proposed experimental setup in which the 2P pulsed excitation laser is sinusoidally modulated at ω (~MHz), and the fluorescence demodulated at 3ω is used as the new signal contrast. (b) The dependence of the demodulated harmonic

fluorescence signals at ω, 2ω, 3ω and 4ω on β which itself scales with $< I_{2P,ave} >^2$. In the weak saturation region ($\beta \leq 0.2$), both 3ω and 4ω harmonic signals scale with $< I_{2P,ave} >^4$.

The detected fluorescence emission rate $S_{fl}(t)$ then becomes:

$$S_{fl}(t) = N\eta\varepsilon f_{rep} P(t) \tag{6.18}$$

where N is the number of fluorophores, η is the fluorescence quantum yield, ε is the collection efficiency. $S_{fl}(t) \approx N\eta\varepsilon f_{rep}\delta_{pulse} K_{exc.2P(t)}$ in the absence of saturation. In contrast, in the strong-saturation condition, $S_{fl}(t) \approx N\eta\varepsilon f_{rep}$, meaning that each molecule can be excited at most once per pulse. Incorporating Eqs. 6.15-17 into $S_{fl}(t)$, we arrive at

$$S_{fl}(t) = N\eta\varepsilon f_{rep}\left[1 - \exp\left(-\beta\left[1+\cos(\omega t)\right]^2\right)\right] \tag{6.19}$$

where $\beta \equiv \delta_{pulse}\sigma_{2P}[< I_{2P,ave} > \lambda_{2P} / (f_{rep}\delta_{pulse} hc)]^2$, characterizing the extend of saturation (or ground state depletion).

We can further expand Eq. 6.19 into Fourier series:

$$\begin{aligned} S_{fl}(t) = (N\eta\varepsilon f_{rep})[S_0 + S_\omega \cos(\omega t) + \\ S_{2\omega}\cos(2\omega t) + S_{3\omega}\cos(3\omega t) + S_{4\omega}\cos(4\omega t)...] \end{aligned} \tag{6.20}$$

In the weak saturation condition where $\beta < 1$ (e.g., 0.2), the Fourier coefficient $S_{n\omega}$ representing the amplitude of the *n*th harmonic frequency have closed forms as

$$S_0 = 1 - e^{-\frac{3}{2}\beta};\ S_{1\omega} = 2\beta e^{-\frac{3}{2}\beta};\ S_{2\omega} = \frac{1}{2}\beta e^{-\frac{3}{2}\beta};\ S_{3\omega} = -\frac{1}{2}\beta^2 e^{-\frac{3}{2}\beta};\ S_{4\omega} = -\frac{1}{16}\beta^2 e^{-\frac{3}{2}\beta} \tag{6.21}$$

Fourier coefficients $S_{n\omega}$, as plotted in Fig. 6.5b, designate that, while the fundamental and the 2ω harmonic signals are proportional to $< I_{2P,ave} >^2$, the 3ω and 4ω signals scale

with $< I_{2P,ave} >^4$. Moreover, $S_{3\omega} / S_0 \approx \beta / 3$ based on Eq. 6.21. Hence, by adjusting the laser intensity that corresponds to $\beta \sim 0.2$ at the focus (about 5 mW of average power for Rhodamine B[19]), the detected focal signal at 3ω would be ~1/15 of the regular 2P signal without modulation.

Since $S_{3\omega}$ scales as $< I_{2P,ave} >^4$ in the weak saturation condition, we expect a spatially more localized contrast by detecting the demodulated fluorescence signal at 3ω :

$$\left(\frac{S}{B}\right)_{3\omega} \approx \frac{\int_{z_{in}}^{} \int_{0}^{r(z)} \left\langle I_{2P,ave}(r,z) \right\rangle^4 dr\, dz}{\int_{z_{out}}^{} \int_{0}^{r(z)} \left\langle I_{2P,ave}(r,z) \right\rangle^4 dr\, dz} \tag{6.22}$$

which represents an overall four-photon process rather than the original two-photon process. Performing the similar integration as in Eq. 6.10, Fig. 6.6a shows that, the decay of $(S/B)_{3\omega}$ as a function of z_{focal} is much slower than that of $(S/B)_{2P}$. At the original depth limit (z_{focal}=1023 μm), $(S/B)_{3\omega}$ is essentially background free, suggesting that the new method could significantly improve the image contrast of regular 2P imaging in scattering samples.

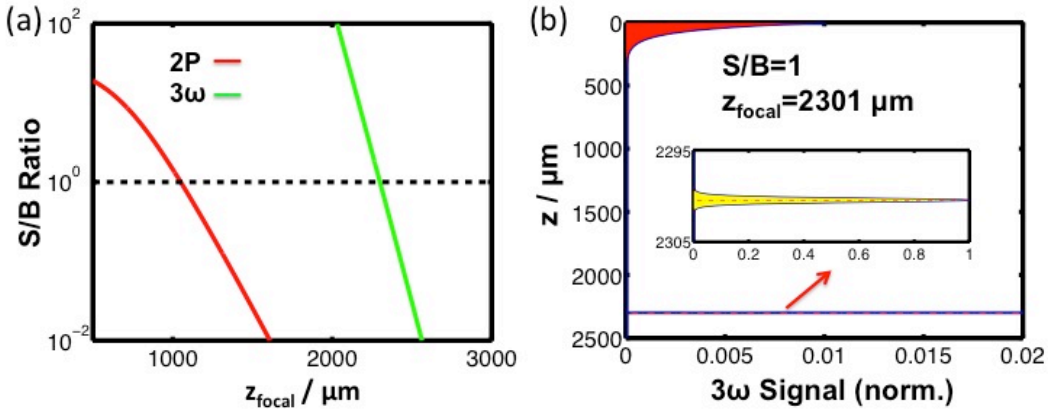

Fig. 6.6 Improved *S/B* contrast and the extended fundamental imaging-depth limit by detecting demodulated 2P fluorescence signal at 3ω. (a) $(S/B)_{3\omega}$ decays to unity much later

than what $(S/B)_{2P}$ does as a function of z_{focal}. (b) The demodulated 3ω signal distributes along the z - layers at the new extended imaging depth of 2301 μm for uniformly stained brain tissue.

6.3.2. Conclusion.

The new extended depth limit is found to be 2301 μm, which corresponds to a unity of $(S/B)_{3\omega}$ (as shown in Fig. 6.6a). This result extends the original depth limit by about 2.3 times. Fig. 6.6b depicts how the demodulated 3ω signal distributes along the z - layers when focusing at this new depth. Furthermore, we also examined the effect of different scattering strengths. For epithelial tissue ($L_s \approx 70$ μm)[3], the depth can be extended from 308 μm (using regular 2P) to 698 μm (by the new approach), which again extends the depth by about 2.3 times.

Theoretically, one could have a depth-unlimited image contrast by driving the excitation over saturation (β>>1) and then detecting even higher-order harmonics (e.g., 5ω, 7ω…). Here we chose only to detect the 8ω signal (the lowest order above the regular quadratic intensity dependence) to more than double the depth limit. In this way, the demodulated signal can be reasonably strong ($S_{3\omega}/S_0 \approx \beta/3$) so that the excitation intensity would only need to approach saturation weakly at focus (achieving 20% saturation of Rhodamine B by ~5 mW average laser power) without causing severe photobleaching. This feature is distinct from SAX microscopy[13, 14], which has to employ sufficiently high-order harmonics (e.g., 8ω) to obtain moderate resolution enhancement.

6.3.3. Discussion.

Insights can be gained by comparing the current technique with stimulated emission reduced fluorescence (SERF) microscopy proposed in section 6.2. First, both techniques explore the spectroscopic transitions of fluorophores for extra nonlinearity. Second, SERF increases the nonlinearity to the third-order, while the current technique to the fourth-order, which consequently offers a more pronounced depth extension (2.3 vs. 1.8 times). Third, the origins of extra nonlinearity are different: SERF comes from the joint action of two laser beams mediated via the fluorescent excited state, while the current technique comes from two-photon fluorescence probed ground state depletion which itself is induced by two-photon absorption. It is worth stressing that the prominent advantage of the current technique lies in its simple apparatus: only an intensity modulator and a lock-in amplifier are needed to add onto a typical laser scanning 2P microscope.

Finally, it is theoretically clearer to generalize the three super-nonlinear fluorescence microscopy techniques including MPAI, SERF and focal saturation. Our techniques exhibit higher-order nonlinearity than the standard two-photon microscopy (e.g. Two-photon fluorescence microscopy (TPFM), SHG, CARS, SRS) (Fig. 6.7a)[20]. Conceptually different from conventional direct multiphoton processes mediated by virtual states, our strategy constitutes a fundamentally new class of fluorescence microscopy where high-order nonlinearity is mediated by real population transfer (Fig. 6.7b), where MPAI and focal saturation exhibit fourth-order nonlinearity, and SERF presents a third-order nonlinearity.

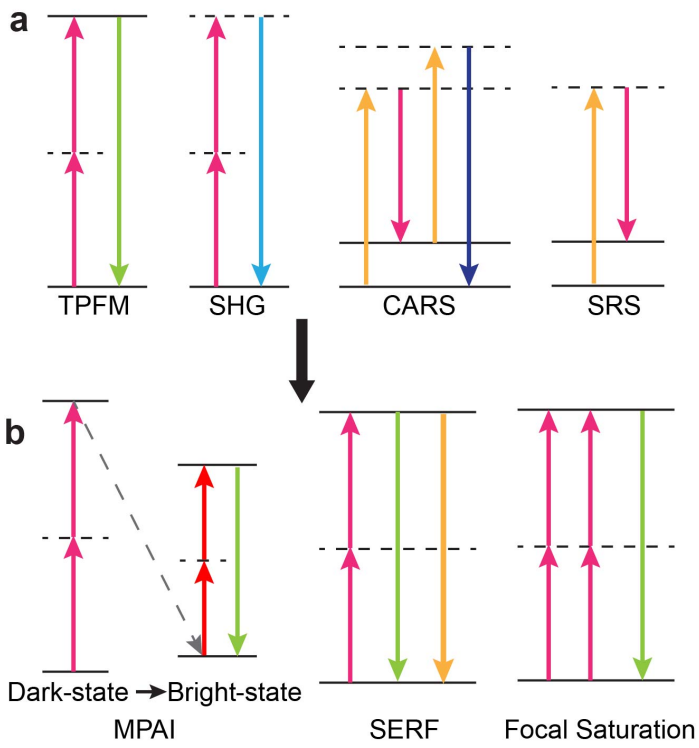

Fig. 6.7 Energy diagrams for nonlinear optical processes. (a) Current short-lived virtual states mediated nonlinear optical processes, including TPFM (two-photon fluorescence microscopy), SHG (second-harmonic generation), CARS (coherent anti-Stokes Raman scattering), and SRS (stimulated Raman scattering). (B) Three proposed (Chapters 5-6) real molecular states mediated high-order nonlinear fluorescence processes. Two-photon activation of photoactivatable fluorophores from dark to bright state, followed by two-photon excitation yield a fourth order fluorescence-to-laser intensity dependence in MPAI. In addition, fluorescence intensity change between two-photon excitation without and with one-photon stimulated emission leads to a third order power dependence in SERF. Finally, two-photon modulated saturated excitation with higher-order harmonic detection results in a fourth order power dependence in focal saturation.

6.4 References.

1. Theer, P. & Denk, W. On the fundamental imaging-depth limit in two-photon microscopy, *J. Opt.Soc. Am. A-Opt. Image Sci. Vis.* **23**, 3139-3149 (2006).
2. Theer, P., Hasan, M. T. & Denk, W. Two-photon imaging to a depth of 1000 μm in living brains by use of a Ti:Al_2O_3 regenerative amplifier, *Opt. Lett.* **28**, 1022-1024 (2003).

3. Kobat, D., Horton, N. G. & Xu, C. In vivo two-photon microscopy to 1.6-mm depth in mouse cortex, *J. Biomed. Opt.* **16**, 106014 (2011).
4. Durr, N. J., Weisspfennig, C. T., A.Holfeld, B. & Ben-Yakar, A. Maximum imaging depth of two-photon autofluorescence microscopy in epithelial tissues, *J. Biomed. Opt.* **16**, 026008 (2011).
5. Hell, S. W. Far-field optical nanoscopy, *Science* **316**, 1153-1158 (2007).
6. Min, W., Lu, S., Chong, S., Roy, R., Holtom, G. R., & Xie, X. S. Imaging chromophores with undetectable fluorescence by stimulated emission microscopy, *Nature* **461**, 1105-1109 (2009).
7. Min, W. Label-free optical imaging of nonfluorescent molecules by stimulated radiation, *Curr. Opin. Chem. Biol.* **15**, 831-837 (2011).
8. Ding, J. B., Takasaki, K. T., & Sabatini, B. L. Supraresolution imaging in brain slices using stimulated-emission depletion two-photon laser scanning microscopy, *Neuron* **63**, 429-437 (2009).
9. Helmchen, F. & Denk, W. Deep tissue two-photon microscopy, *Nat. Methods* **2**, 932-940 (2005).
10. Bianchini, P., Harke, B., Galiani, S. Vicidomini, G. & Diaspro, A. Single-wavelength two-photon excitation-stimulated emission depletion (SW2PE-STED) superresolution imaging, *Proc. Natl. Acad. Sci. USA* **109**, 6390–6393 (2012).
11. Hell, S. Microscopy and its focal switch, *Nat. Methods* **6**, 24-32 (2009).
12. Isobe, K. et al. High-resolution fluorescence microscopy based on a cyclic sequential multiphoton process, *Biomed. Opt. Express* **1**, 791-797 (2010).
13. Fujita, K., Kobayashi, M., Kawano, S., Yamanaka, M., & Kawata, S. High-resolution confocal microscopy by saturated excitation of fluorescence, *Phys. Rev. Lett.* **99**, 228105 (2007).
14. Yamanaka, M., Kawano, S. Fujita, K. Smith, N. I. & Kawata, S. Beyond the diffraction-limit biological imaging by saturated excitation microscopy, *J. Biomed. Opt.* **13**, 050507 (2008).
15. Hell, S. W. & Kroug, M. Ground-state-depletion fluorscence microscopy: a concept for breaking the diffraction resolution limit, *Appl. Phys. B* **60**, 495-497 (1995).

16. Heintzmann, R., Jovin, T. M. & Cremer, C. Saturated patterned excitation microscopy-a concept for optical resolution improvement, *J. Opt. Soc. Am. A* **19**, 1599-1609 (2002).
17. Gustafsson, M. G. L. Nonlinear structured-illumination microscopy: wide-field fluorescence imaging with theoretically unlimited resolution, *Proc. Natl. Acad. Sci. U.S.A.* **102**, 13081-13086 (2005).
18. Humpolícková, J., Benda, A. & Enderlein, J. Optical saturation as a versatile tool to enhance resolution in confocal microscopy, *Biophys. J.* **97**, 2623-2629 (2009).
19. Xu, C. & Webb, W. W. Measurement of two-photon excitation cross sections of molecular fluorophores with data from 690 to 1050 nm, *J. Opt. Soc. Am. B* **13**, 481-491 (1996).
20. Zhu, X., Kao, Y. -T., & Min, W. Molecular-Switch-Mediated Multiphoton Fluorescence Microscopy with High-Order Nonlinearity, *J. Phys. Chem. Lett.* **3**, 2082 (2012).

APPENDIX

Publications from stimulated Raman scattering microscopy:

1. **Wei, L.**, Yu, Y., Shen, Y., Wang, M. & Min, W. Vibrational imaging of newly synthesized proteins in live cells by stimulated Raman scattering microscopy, *Proc. Natl. Acad. Sci. USA,* 110, 11226-11231 (2013), *Direct Submission.*

2. **Wei**, **L.**, Hu, F., Shen, Y., Chen, Z., Yu, Y., Lin, C. -C., Wang, M. C. & Min., W. Live-cell imaging of alkyne-tagged small biomolecules by stimulated Raman Scattering, *Nat. Methods*, 11, 410-412 (2014).

3. **Wei**, **L.**, Shen, Y., Xu, F., Hu, F., Harrington, J. K., Targoff, K. L. & Min., W. Imaging complex protein metabolism in live organisms by stimulated Raman scattering microscopy with isotope labeling, *ACS Chem. Bio.* 10, 901-908 (2015).

4. Hu, F., **Wei**, **L.**, Zheng, C., Shen, Y. & Min, W. Vibrational imaging of choline metabolites in live cells by stimulated Raman scattering coupled with isotope-based metabolic labeling, *Analyst*, 139, 2312-2317 (2014).

5. Chen, Z., Paley, D., **Wei**, **L.**, Weisman, A., Friesner, R., Nuckolls, C. & Min., W. Multicolor live-cell chemical imaging by isotopically edited alkyne vibrational palette, *J. Am. Chem. Soc.* 136, 8027-8033 (2014).

6. Shen, Y., Xu, F., **Wei**, **L.**, Hu, F. & Min, W. Live-cell quantitative imaging of proteome degradation by stimulated Raman scattering, *Angew. Chem. Int. Ed.* 53, 5596-5599 (2014).

7. Hu, F., Chen, Z., Zhang, L., Shen, Y., **Wei, L.**, & Min, W. Vibrational Imaging of Glucose Uptake Activity in Live Cells and Tissues by Stimulated Raman Scattering, *Angew. Chem. Int. Ed.* 54, 9821-9825 (2015).

Publications from super-nonlinear fluorescence microscopy:

8. **Wei**, **L.**, Chen, Z. & Min, W. Stimulated emission reduced fluorescence microscopy: a concept for extending the fundamental depth limit of two-photon fluorescence imaging, *Biomed. Opt. Express* 3, 1465-1475 (2012).

9. Chen, Z.*, **Wei, L.***, Zhu, X.* & Min, W. Extending the fundamental imaging-depth limit of multi-photon microscopy by imaging with photo-activatable fluorophores, *Opt. Express* 20, 18525-18536 (2012). *Co-first author

10. **Wei, L.** & Min, W. What can stimulated emission do for bio-imaging? *Ann. N. Y. Acad. Sci.,* 1293,1-7 (2013).

11. Xu, F., **Wei**, **L.**, Chen, Z. & Min, W. Frustrated FRET for high-contrast high-resolution two-photon imaging, *Opt. Express*, 12, 14097-14108 (2013).